Materials Advances

REVIEW

View Article Online
View Journal | View Issue

Cite this: *Mater. Adv.*, 2026, 7, 3993

Composite polymer electrolytes for sodium-ion batteries: from material design to interfacial engineering and future perspectives

Muhammad Irfan, Khizar Hayat Khan, * Afzal Shah and Hazrat Hussain *

The escalating need for sustainable and safe energy storage systems has positioned sodium-ion batteries (SIBs) as a viable substitute for lithium-ion batteries, considering the lower expense and natural abundance of sodium. However, the flammability and dendrite-related safety concerns of traditional liquid electrolytes necessitate the advancement of durable solid-state electrolytes. Among these, composite polymer electrolytes (CPEs), which integrate inorganic fillers within a polymer matrix, have arisen as a leading alternative to tackle the drawbacks of individual solid polymer and inorganic ceramic electrolytes. This review provides a comprehensive and up-to-date insight into the design, preparation, and performance of CPEs for SIBs. We systematically discuss the fundamental ion migration mechanisms, the critical role of active (Na-ion conductive) and passive (inert) fillers in enhancing ionic conductivity, electrochemical stability, and mechanical strength, and the various fabrication techniques employed. A significant focus is placed on interfacial engineering strategies to mitigate the substantial interface resistance between solid electrolytes and electrodes. Finally, we address the prevailing challenges and offer future perspectives, highlighting the need for integrated design from mechanics to materials science to accelerate the practical application of high-performance, safe, and durable CPEs in next-generation SIBs.

Received 7th November 2025,
Accepted 23rd March 2026

DOI: 10.1039/d5ma01290b

rsc.li/materials-advances

1. Introduction

Fossil fuels presently serve as the major global energy source, yet their limited availability underscores the urgent need to explore sustainable alternatives. In addition to being non-renewable, fossil fuels significantly contribute to

Department of Chemistry, Quaid-i-Azam University, Islamabad, 45320, Pakistan. E-mail: khayat@chem.qau.edu.pk, hazrat.hussain@qau.edu.pk

Muhammad Irfan

Muhammad Irfan has been honored with a Master of Philosophy degree in Physical Chemistry from Quaid-i-Azam University, Islamabad, Pakistan (2023–2025). His research focuses on the synthesis of nano-materials, including 3D metal–organic frameworks and composite biopolymer-based solid-state electrolytes for lithium- and sodium-ion batteries. He has also worked as a Research Assistant in the Department of Chemistry at Quaid-i-Azam University from 2024 to 2025, contributing to laboratory experiments with MSc students.

Khizar Hayat Khan

Khizar Hayat Khan received his PhD in Physical Chemistry (2019–2024) from Quaid-i-Azam University, Islamabad, Pakistan, with collaborative research at Martin Luther University Halle-Wittenberg, Germany, supported by a DFG-funded project. His research focuses on polymer synthesis, mechanically robust self-healable polymers, 2D nanofiller functionalization, and the development of solid composite polymer electrolytes for lithium-ion batteries. He is currently a postdoctoral researcher at Shanghai Jiao Tong University, Shanghai, China.

environmental degradation, including climate change and air pollution, driving the global transition toward cleaner energy solutions.[1–3] For instance, fossil fuels account for over 80% of global energy consumption[4] and are responsible for approximately 75% of greenhouse gas emissions.[5] One way to reduce our reliance on fossil fuels is to search for renewable alternatives and develop robust energy storage devices.[6,7]

The demand for energy storage with better efficiency has reached unprecedented levels, propelled by the fast growth of portable gadgets, grid-level energy storage, and EVs.[8,9] Among the available options, lithium-ion batteries (LIBs), having rechargeable characteristics, have surfaced as the top preference for portable energy storage because of their exceptional performance, including long-term stability, low self-discharge rates, high energy density, extended lifespan, and overall reliability.[10–13] For example, LIBs power over 90% of portable electronics and are the backbone of the rapidly growing electric vehicle market, which is projected to reach 145 million units globally by 2030.[14,15] Comprehensive studies have been carried out over the years to optimize the efficiency of LIBs, confronting critical factors such as safety, cycle life, and energy density.[16,17] While LIBs are central to the energy storage revolution, their scalability is challenged by the fundamentals of lithium supply. Geographically concentrated deposits lead to fragile supply chains and cost inflation, posing a systemic risk to the industry as global demand accelerates. This creates a pressing need for complementary technologies with more resilient material bases.[18,19]

A promising alternative is to replace lithium with a suitable metal that offers comparable performance and is cost-effective and abundantly available. Sodium-ion batteries (SIBs) have acquired substantial momentum in recent years owing to their great capability to match the performance of LIBs while benefiting from the lower cost and abundance of sodium.[20] Both sodium and lithium are present in the same group of the periodic table with comparable chemical properties, with each having one loosely bound electron in its outermost shell, allowing them to form Na^+ and Li^+ ions.[21–23] Both ions are quite comparable as charge carriers, with sodium exhibiting a standard electrode potential of −2.71 V against the standard hydrogen electrode (SHE), merely 300 mV beyond lithium's electrode potential of −3.04 V against the SHE.[24,25] Whereas LIBs benefit from the lightweight nature and small ionic radius of Li^+, enabling them to achieve a higher energy density of 150–250 Wh kg^{-1} in comparison to 90–150 Wh kg^{-1} for SIBs, SIBs hold significant promise in the long run.[26] The abundant availability and lower cost of sodium can make SIBs a more renewable and cost-effective alternative for vast energy storage systems.[27]

Traditional SIBs, like LIBs, typically utilize combustible organic liquid electrolytes.[28,29] The combination of sodium metal anodes and liquid electrolytes in SIBs raises the possibility of leakage and fire in electric vehicles, especially during overcharging or misuse operations. Moreover, like LIBs, SIBs must contend with the inevitable development of dendrites because of the harmful reactions between the reactive liquid electrolytes and the sodium anode.[30,31] In addition, repeated charging and discharging can worsen the problem by allowing dendrites to pierce the separator and come into contact with the cathode, which leads to internal short circuits.[31,32] This reduces the battery lifespan and overall efficiency by causing poor cycling stability and capacity decline.

The risks associated with flammable liquid electrolytes can potentially be addressed by transitioning to semisolid gel-like electrolytes[33] and fully solid-state electrolytes (SSEs).[34,35] Quasi-solid gel electrolytes (QSGEs) sit between liquids and solids, combining the best of both worlds.[36] They maintain the high ion conductivity of liquid electrolytes while providing the mechanical stability of solid electrolytes.[37] As a result, QSGEs greatly reduce leakage risks without sacrificing electrochemical performance. So how do they work? Inside a QSGE, a three-dimensional network is created either by polymer chains or small molecule gelators that trap the organic solvent and hold the electrolyte salts in place.[38] But importantly, it still allows ions to move. The network actually helps in salt dissociation, increasing the free charge carrier concentration, and unlike in liquid electrolytes, this gel structure creates more uniform pathways for ion movement, reducing clumping and boosting conductivity. The network also slows down anions, which helps cations move more efficiently toward the electrodes, improving the transference number.[39]

One effective way to build these QSGE networks is to use low-molecular-weight gelators (LMWGs). These are small molecules that self-assemble through weak non-covalent interactions to form 'solid-like' nanoscale networks. These networks then immobilize the liquid electrolyte, turning it into a stable gel.[40] This unique structure captures the high ionic conductivity of liquid electrolytes while eliminating leakage risks, a critical safety and performance hurdle in batteries.[41,42] For battery applications, LMWGs offer a key advantage: the self-assembled network traps the solvent but leaves plenty of open space for ions to move freely. Early work conducted by

Hazrat Hussain

Hazrat Hussain is a Professor of Physical Chemistry at Quaid-i-Azam University, Islamabad. He earned his MSc and MPhil from QAU and completed his Dr-Ing in 2004 at Martin Luther University Halle, Germany. He held post-doctoral and research positions in the UK and Singapore. He is a Fellow of the Chemical Society of Pakistan. He received the Georg Förster Research Fellowship (2014) from the Alexander von Humboldt Foundation, Germany. His research focuses on polymer synthesis via reversible-deactivation radical polymerization (RDRP) and polymer electrolytes for lithium-ion batteries (LIBs).

Table 1 Comparison of electrolyte classes: ionic conductivity, advantages, limitations, and environmental aspects

Electrolyte class	Ionic conductivity (S cm^{-1})	Key advantages	Limitations and environmental aspects
Liquid electrolytes (LEs)	10^{-3}–10^{-2}	High ionic conductivity; good/stable contact with electrodes	High risk of leakage and combustion (safety issues); lithium dendrite growth during repeated deposition, destroying interface stability and potentially causing short circuit; thermal runaway can cause fire or explosion
Solid electrolytes (SEs)	10^{-8}–10^{-4}	Address leakage problems and dendrite growth problems	Low ionic conductivity (however, for inorganic solid electrolytes the conductivity could be as high as 10^{-3} S cm^{-1}); high interfacial resistance; volume change during charging/discharging causes separation of the interface
Polymer gel electrolytes (PGEs)	10^{-4}–10^{-3}	Solid state; high mechanical stability; high thermal stability; high mechanical durability; wide electrochemical window (when using ionic liquids); non-leakage; good interfacial properties; suppress dendrite growth	Low conductivity (much lower than liquid electrolytes); irreversible and continuous degradation of internal structure (limits device lifetime); a rather complicated manufacturing process; very long time of decomposition; disposal and recycling problems
Supramolecular gels based on low molecular weight gelators (LMWGs)	10^{-4}–10^{-3}	Thermally reversible gels; neutral to the environment; good biodegradability (natural origin derivatives like monosaccharides, cholesterol, and hydrazides); self-assembly *via* non-covalent interactions; enhanced conductivity effect observed in some cases; disposal and recycling advantages as thermally reversible systems	Lower mechanical strength; a smaller temperature range of the gel phase; less known and understood; need more studies and development before substituting PGEs

Hanabusa and co-workers in 1999 showed that ionic mobility in these gels remained nearly as high as that in the pure liquid electrolyte.[43] This means LMWG-based gels can achieve liquid-like conductivity while providing mechanical stability and leak resistance of a solid. Researchers have since demonstrated LMWG-based gel electrolytes in lithium-ion batteries, using gelators like DBS (1,3:2,4-dibenzylidenesorbitol) in common electrolyte solvents.[44] More recent work has extended this approach to emerging battery chemistries, including zinc-ion batteries, where LMWG-based ionogels have shown excellent performance even at extremely low temperatures while suppressing dendrite formation.[45,46] For a better understanding of the role of LMWG-based quasi-solid gel electrolytes in the broader landscape of electrolyte systems, a comparison of important electrolyte classes, including conventional liquid electrolytes, ionic liquid electrolytes, gel polymer electrolytes (GPEs), and supramolecular gel electrolytes, is summarized in Table 1. This comparison sheds light on their fundamental differences in terms of ionic conductivity, safety, mechanical properties, and practical limitations.

SSEs can be classified into three primary classes: inorganic ceramic electrolytes (ICEs), solid polymer electrolytes (SPEs), and composite polymer electrolytes (CPEs). Fig. 1 shows the schematic of sodium metal electrodes with various electrolyte material classes. These electrolytes offer benefits over standard liquid electrolytes and are the focus of extensive research aimed at advancing the practical implementation of solid-state SIBs.

Fig. 2 shows the characteristics, performance, and efficiency of ICEs, SPEs, and CPEs. ICEs [for example, sodium β″-alumina (BASE), NASICON-structured $Na_3Zr_2Si_2PO_{12}$ (NZPS) and its doped derivatives, and $Na_5GdSi_4O_{12}$ (NGS)],[47,48] due to their exceptional qualities like superior thermal stability, greater ionic conductivity, mechanical integrity, and excellent electrochemical stability, have shown great potential for use in SIBs.[49,50] However, the widespread use of ICEs is hampered in SIBs due to the intrinsic stiffness and low interfacial compatibility with electrodes. Lee *et al.*[51] have recently presented a comprehensive review of ICEs for sodium-ion batteries.

SPEs, featuring a polymer matrix with a sodium salt dispersed within it, are desirable owing to their design flexibility, good thermal and mechanical stability, and electrochemical performance.[52,53] Despite their improved safety and greater flexibility in comparison to liquid electrolytes, the ionic conductivity at room temperature for SPEs stays significantly below the desired value of $\sim 10^{-3}$ S cm^{-1}, restricting their broader adoption.[54,55]

In the past ten years or so, numerous promising strategies and innovative ideas have been put forward and investigated to attain the desired battery performance of SSEs for SIBs.[56] A particularly excellent approach is the development of CPEs that involve the distribution of inorganic fillers within a polymer matrix, creating SSEs with robust thermal, mechanical, electrochemical, and battery performance (Fig. 2).[57,58] While CPEs for LIBs are thoroughly reviewed, the same cannot be said for SIBs, where only a handful of reviews exist, leaving a substantial gap in the literature.[59] This gap persists even as SIB technology gains prominence as a complementary energy storage solution. Reviews of SIB-based CPEs that are currently available tend to focus on either filler chemistry or polymer host materials, frequently discussing ion-transport behavior, interfacial stability, and processing considerations separately. For instance, the review article written by Kumar *et al.*[59] on sodium ion polymer electrolytes focuses on synthetic strategies and their influence on ion-conduction parameters across solid, gel, and composite polymer electrolytes, with particular emphasis on conductivity mechanisms and fundamental materials chemistry. More

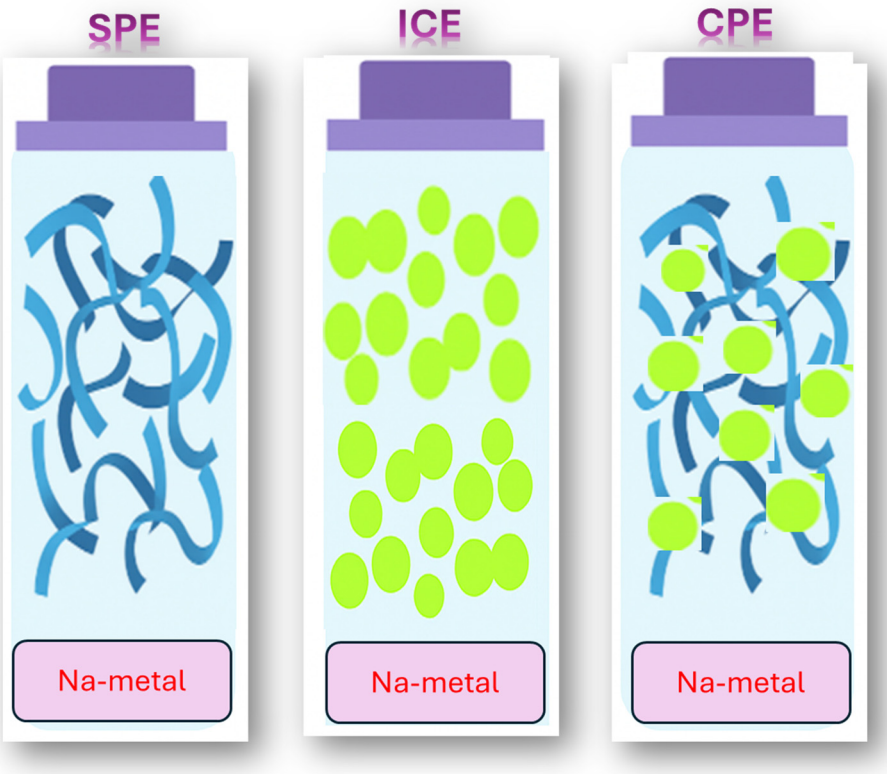

Fig. 1 Schematic representation of sodium metal electrodes with different electrolyte materials.

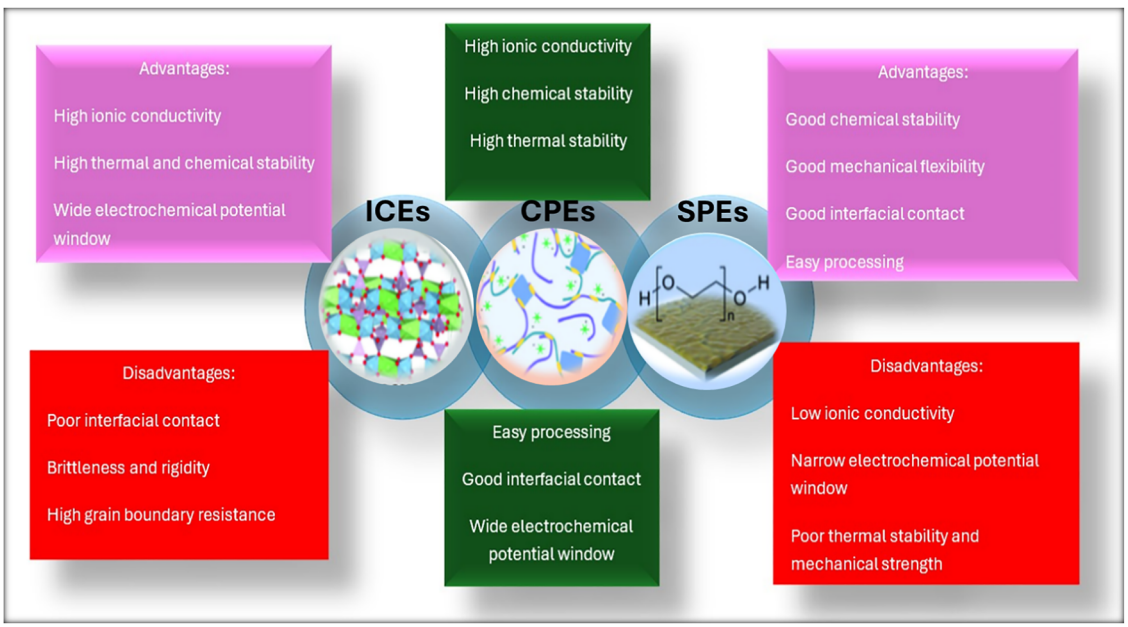

Fig. 2 Characteristic properties of ICEs, SPEs, and CPEs based on their performance and efficiency.

recently, He *et al.*[60] reviewed composite polymer solid electrolytes for all-solid-state sodium batteries, concentrating on the role of inorganic fillers dispersed within polymer matrices and discussing how filler type, particle size, content, and preparation methods affect ionic conductivity and interfacial compatibility. Senthilkumar *et al.*[61] recently published a comprehensive review examining how NASICON fillers optimize the performance of composite polymer electrolytes, with particular

emphasis on improvements in ionic conductivity, structural robustness, and electrochemical stability. The work of Gabryelczyk *et al.*[62] focused on the application of ionic liquids in tailoring the properties of gel polymer electrolytes for SIBs.

The current review highlights recent advances in the structural design of composite polymer electrolytes for sodium-ion batteries, focusing on material strategies, fabrication methods, ion transport mechanisms, and interfacial engineering approaches that boost both electrochemical and mechanical performances. Unlike earlier reviews, we integrate these elements into a cohesive framework, drawing on recent literature to connect structure–property–performance relationships with processing and interface considerations. We also present a unified perspective by categorizing nanofillers based on their primary function and linking their intrinsic properties to battery performance. In addition, we include a comparative analysis of interfacial strategies for sodium metal anodes, emphasizing the distinct mechanisms and the critical role of microstructure in achieving long-term stability. Finally, we outline current challenges and propose directions for future research.

2. Desirable characteristics of composite polymer electrolytes

Fig. 3 depicts the desirable general characteristics of CPEs. For CPEs to be suitable for widespread adoption, the following characteristics are highly desirable:

1. High ionic conductivity: at room temperature or under operational conditions, the ionic conductivity should be $\geq 10^{-3}$ S cm^{-1}. However, most sodium-based SPEs typically achieve room temperature ionic conductivities in the range of 10^{-5}–10^{-4} S cm^{-1}, with values approaching 10^{-3} S cm^{-1} only in systems with plasticizers or ionic liquids.[63]

2. Wide ESW: a wide ESW (0–5 V) ensures minimal electrolyte degradation at high voltages.[64] Furthermore, it ensures efficient and reversible Na^+ ion insertion and deinsertion, which is critical for maintaining stable performance over multiple cycles. However, sodium-based polymer electrolytes have a theoretical upper limit of approximately 5 V. In practice, most SPEs and CPEs undergo oxidative breakdown at 4.0–4.3 V, depending on polymer chemistry and the salt coordination environment.[65] Thus, the "0–5 V" window should be viewed as an ideal design target rather than a common working range.

3. Mechanical stability: a better mechanical strength maintains the structural integrity of the solid electrolyte during charge–discharge, which is necessary to prevent dendrite formation and address safety concerns.[66]

4. Thermal stability: thermal stability is required for smooth battery operation at elevated temperatures. A thermally unstable electrolyte could lead to electrolyte deformation and structural failures and could cause short-circuiting and thermal runaway at elevated temperatures.[67]

5. Compatibility with sodium metal: the electrolyte must be chemically inert and compatible with sodium metal to avoid or

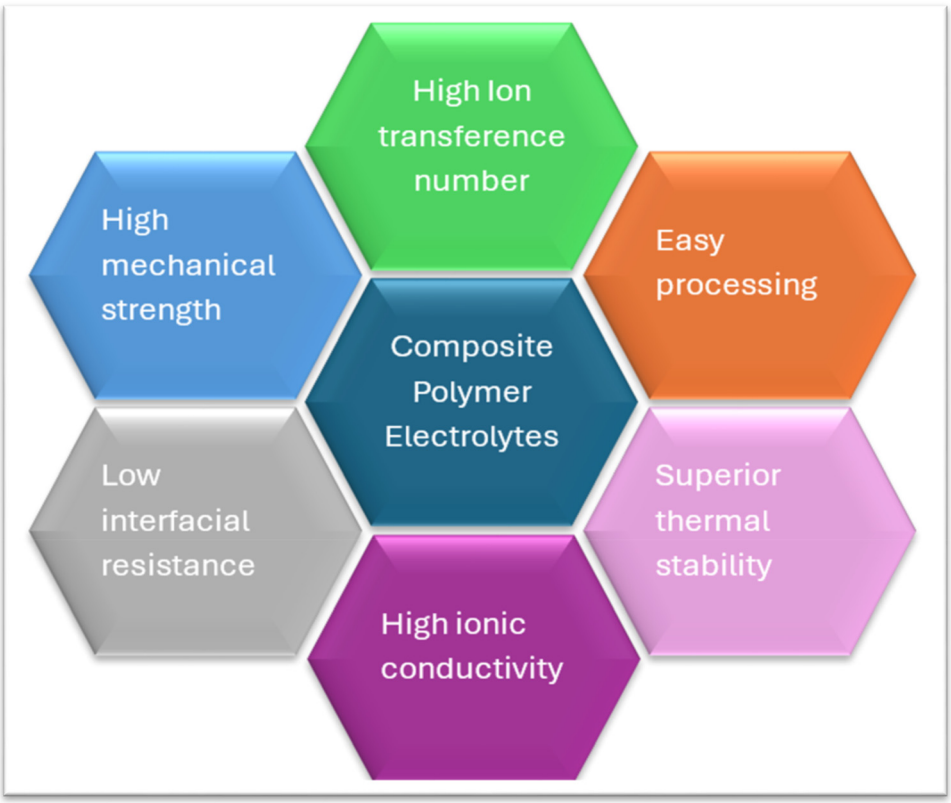

Fig. 3 Characteristics of composite polymer electrolytes.

minimize the unnecessary side reactions that degrade the battery performance.[68]

6. High Na^+ transference number: a high Na^+ transference number is a critical design parameter for solid electrolytes, as it minimizes concentration polarization and enhances power density.[69] The ideal scenario: a transference number of unity, where current is carried exclusively by Na^+ ions, represents a theoretical upper limit for single-ion conductors. In practice, this ideal is rarely achieved; most high-performing SPEs report values between 0.7 and 0.9 at operating temperatures. Nevertheless, this ideal serves as a vital benchmark for evaluating and comparing the cationic selectivity of emerging electrolyte materials. A Na^+ transference number of $\sim$1 is desirable as it ensures that the current is predominantly conducted by the sodium ions with negligible contribution from the anions. This minimizes ion concentration polarization effects and results in enhanced battery performance.

7. Low interfacial resistance: the electrolyte should create a stable and low-resistance electrode/electrolyte interface to provide a fast charge/discharge mechanism and reduce energy losses.[70]

8. Easy processability and economically viable: the fabrication process should be simple, scalable, and economically viable.[71]

3. Techniques for the fabrication of composite polymer electrolytes for sodium-ion batteries

3.1. Solution-casting technique

The solution-casting technique is a straightforward, low-cost, and widely used method for fabricating polymer-containing solid electrolytes with thicknesses typically ranging from 50 to 300 μm.[72] This approach enables the facile incorporation of varying contents of fillers, sodium salts, and plasticizers, allowing convenient optimization of CPE properties.[73] The process typically involves the following steps as depicted in Fig. 4: first, a homogeneous polymer solution is prepared by dissolving the polymer in an appropriate solvent. Next, a precise amount of sodium salt is added and dispersed through agitation. Fillers (*e.g.*, nanoparticles) are then incorporated and uniformly distributed by stirring. Finally, the solution is cast onto a Teflon Petri dish or flat glass, and a controlled solvent evaporation process ensures uniform film formation while minimizing defects.

3.2. Hot pressing/thermal pressing method

Being solvent-free, dry, faster, and cost-effective, the hot-press method provides several advantages over the ordinary and traditional solution-cast approach.[74] The fabrication process as schematically shown in Fig. 5 begins by thoroughly mixing the precursor constituents: polymer, plasticizer, salt, and fillers. When the blend achieves a temperature close to the melting point of the cast polymer upon heating, it results in a uniform and thick slurry. The heated slurry is placed inside metal sheets and put under elevated pressure for fabricating CPE films. This controlled application of heat and pressure leads to the preparation of a uniform, high-quality film with excellent structural integrity.[75,76]

3.3. *In situ* polymerization technique

This method involves dispersing nanofillers into a precursor monomer solution, followed by *in situ* polymerization using conventional techniques. A key aspect of this process is the grafting technique, where polymer chains are grown onto the particle surface through the 'grafting from' approach.[78] This ensures a stable and uniform distribution of the fillers, preventing nanofiller agglomeration within the matrix and enhancing the structural integrity and performance of the resulting nanocomposite. Several CPEs for SIBs have been successfully fabricated using the *in situ* polymerization technique.[79]

3.4. Electrospinning technique

In this procedure, a polymer solution is subjected to an elevated-voltage electric field, generating a thin jet that solidifies into nanofibers upon solvent evaporation.[80,81] Key parameters, such as solution concentration and electric field strength, are optimized to control fiber diameter and surface morphology.[82] The resulting nanofiber mats possess a high surface area and interconnected pores, which facilitate enhanced ion transport and improved ionic conductivity. The large surface area, high porosity, tunable morphologies, and high density of active sites make them particularly advantageous for power storage devices, particularly as electrolyte and electrode materials in supercapacitors, where their unique characteristics significantly enhance performance.[83]

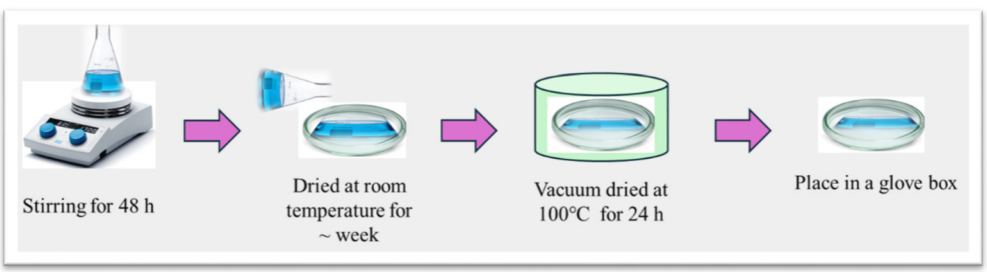

Fig. 4 Schematic depiction of a solution-casting method for fabricating polymer–based solid electrolyte films.

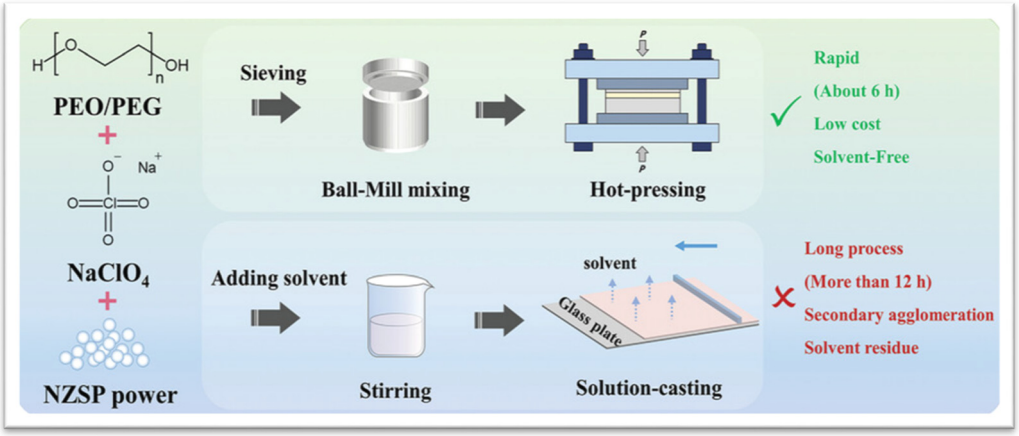

Fig. 5 PEO/PEG-based CPE produced by a hot-press technique (reprinted with permission from ref. 77. Copyright © 2024 Wiley-VCH GmbH).

3.5. Phase inversion method

A widely employed method known as the phase inversion is utilized for fabricating polymer electrolyte films with precise control over the properties and structure of membranes.[84,85]

The typical steps involved as depicted schematically in Fig. 6 are as follows: a polymer viscous solution is first formed using an appropriate solvent and cast onto a Teflon Petri dish or glass plate. The cast film is then plunged into a precipitation tank, typically water, inducing the formation of an asymmetric surface morphology. Rapid precipitation occurs due to solvent and nonsolvent exchange at the interface, leading to distinct membrane structures. Throughout this process, multiple phase transitions take place, influenced by the composition of the casting solution and additives used, ultimately defining the final membrane properties.

4. Performance evaluation

4.1. Ionic conductivity

The ionic conductivity of a solid electrolyte is generally determined by employing electrochemical impedance spectroscopy (EIS), where an AC potential is applied across a frequency domain (1 MHz to 10 mHz), and the impedance response is recorded.

For these measurements, a symmetric cell configuration is employed with the electrolyte placed between two blocking electrodes (*e.g.*, stainless steel or platinum) as schematically depicted in Fig. 7a. Unlike reactive electrodes such as lithium metal, perfectly blocking electrodes do not participate in redox reactions or charge transfer processes. When an electric field is applied, ions transfer toward the electrodes and accumulate at the electrode–electrolyte interface, creating an electric double layer as illustrated in Fig. 7a. This interfacial charge storage behaves as an idealized capacitor characterized by a double-layer capacitance (C_D). This electrolyte/blocking electrode system can be depicted by an equivalent circuit (Fig. 7b) where R_b is in parallel with the geometric capacitance (C_b) of the electrolyte, and this parallel combination is in series with C_D. The impedance data are generally presented as a Nyquist plot; plotting the real (v) *versus* imaginary (Z'') impedance. In an ideal system, the plot consists of a semicircle with its center on the horizontal Z'-axis and a vertical spike at low frequencies (Fig. 7c). The semicircle represents the bulk electrolyte

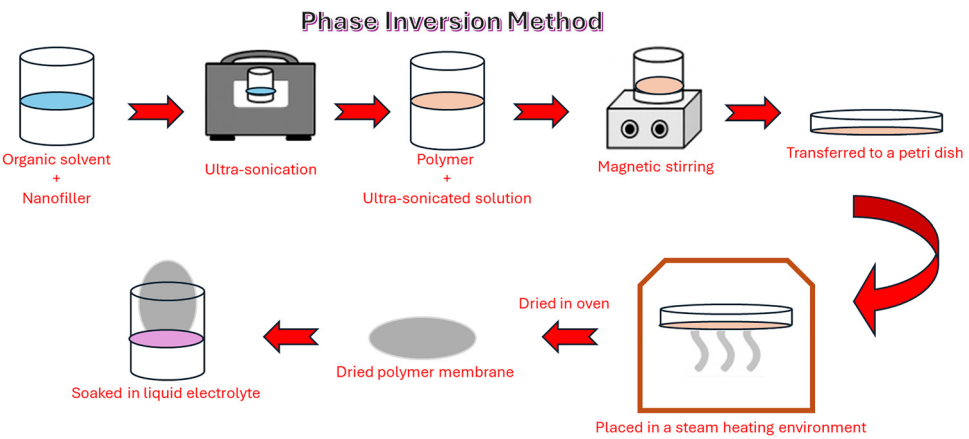

Fig. 6 Diagram showing schematically the stages involved in creating a porous polymer electrolyte membrane by a phase inversion method.

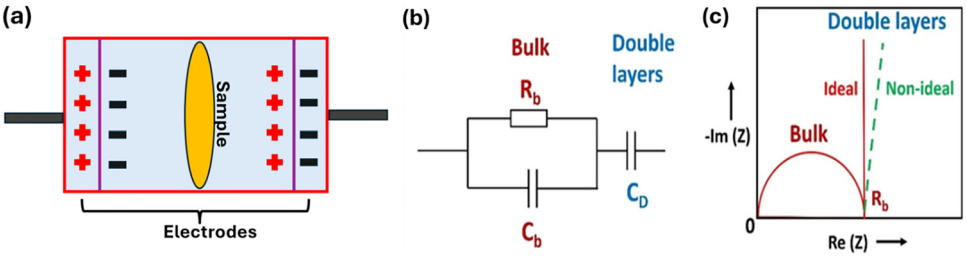

Fig. 7 Ionic conductivity measurement using blocking electrodes. (a) Schematic of the symmetric cell configuration with a solid electrolyte (SE) sandwiched between blocking electrodes. (b) Equivalent circuit representing the blocking electrode setup. (c) Characteristic Nyquist plot showing contributions from bulk electrolyte (high-frequency semicircle) and double-layer capacitance (low-frequency spike) (reprinted with permission from ref. 86. Copyright © 2021 Wiley).

behavior, while the vertical spike corresponds to double-layer formation at the electrolyte–electrode interface. Nevertheless, practical systems often display divergence from this ideal performance, with the impedance plot showing a reduced semicircle (where the center lies below the Z'-axis) and a slanted spike. In many cases, only portions of these features may be visible. The observed deviations from ideal behavior in real systems can be attributed to factors such as surface roughness, inhomogeneities in the electrolyte, or partial electrode reactions, as discussed by Careem *et al.*[87] in their analysis of impedance spectroscopy for polymer electrolyte analysis.

For calculating the electrolyte ion conductivity, R_b is obtained from the intersection of the spike and the semicircular part. The ionic conductivity (σ) is then derived from R_b using eqn (1):

$$\sigma = \frac{l}{R_b A} \quad (1)$$

where A and l denote the thickness and contact surface area of the electrolyte layer/electrode, respectively.

4.2. Sodium-ion transference number

The sodium-ion transference number (t_{Na^+}) is a crucial criterion in evaluating the performance of SPEs used in SIBs. The t_{Na^+} indicates the fraction of the total ionic current transported by sodium ions in the cell.[88] A higher t_{Na^+} approaching unity indicates dominant sodium-ion conduction, which minimizes concentration polarization and enhances ion transport efficiency. This leads to faster charging rates and more stable electrochemical performance, underscoring the importance of achieving a high t_{Na^+} in the advancement of high-performance SPEs.[83,89]

The method introduced by Bruce and Vincent[90] is widely employed to estimate t_{Na^+} by applying a small voltage bias (typically less than 10 mV) across a symmetric metal|SPE|metal cell, using sodium metal electrodes in the case of SIBs, and monitoring the first and steady-state current responses as represented by eqn (2);

$$t_{Na^+} = \frac{I_s(\Delta V - I_0 R_0)}{I_0(\Delta V - I_s R_s)} \quad (2)$$

In this context, ΔV denotes the voltage applied through the cell, typically maintained below 10 mV. I_0 and I_s represent the initial current and steady-state current, respectively, while R_0 and R_s correspond to the initial interfacial resistance/impedance and steady-state interfacial resistance/impedance of the cell. However, it is important to recognize that this technique assumes ideal, infinitely diluted electrolyte conditions, which are rarely met in practical battery systems. As such, the transference numbers derived from this approach, often referred to as the "limiting current fraction", do not precisely signify the actual fraction of current transported by Na^+ ions. Rather, they encompass a range of transport-related factors, including ionic conductivity and diffusion coefficients, and should be interpreted with caution in the context of real battery environments.[91] Nevertheless, several studies[91,92] suggest that this value can still provide meaningful insights, provided it is interpreted with caution and an understanding of the various transport phenomena it encompasses.

In typical SIB electrolytes employing commercial polyolefin separators, the sodium-ion transference number is approximately 0.17,[93] a value comparable to that observed in LIB electrolytes.[94] One effective strategy to increase this parameter involves the use of polymers containing immobilized anionic groups, commonly referred to as "single-ion conductors." For example, Youcef *et al.*[95] created a singular ion-conductive SPE by covalently immobilizing the counterion (fluorosulfonylimide, FSI) onto an ethylcellulose backbone. Such single-ion conducting systems have demonstrated consistently high transference numbers, often exceeding 0.8; however, this enhancement is sometimes accompanied by a reduction in overall ionic conductivity. Representative examples of single-ion conducting polymers include polymerized sodium tartaric acid borate,[96] organic sulfonyl-based derivatives,[97] and modified Nafion materials.[98] To enhance mechanical and electrochemical stability, these polymers are often blended with traditional polymer matrices. Some theoretical studies suggest that the exceedingly electronegative fluorine atoms in PVDF–HFP can hinder the mobility of anions, potentially leading to an inherently higher sodium-ion transference number.[99,100] However, there is currently no definitive experimental evidence that PVDF–HFP alone inherently provides a high transference number. Reported t_{Na^+} values for PVDF–HFP-based electrolytes vary widely, from ~0.2–0.3 to 0.5–0.6,[101,102] suggesting unresolved

discrepancies that warrant further mechanistic studies. Therefore, claims of naturally high t_{Na^+} in PVDF–HFP should be read cautiously and experimentally validated before being generalized.

4.3. Electrochemical stability window

Despite significant progress in performance enhancement of SPEs and their integration into commercial electric vehicles,[103] several critical challenges remain before SPE-based batteries can achieve widespread application. One of the primary limitations is related to electrochemical stability.[104] The electrochemical stability window (ESW) is the voltage range over which a SSE remains stable and therefore determines electrode compatibility and the allowable operating voltage of the battery.[51] A broader ESW facilitates the use of high-voltage cathode materials, thereby increasing the achievable energy density. Cyclic voltammetry (CV) and linear sweep voltammetry (LSV) are widely employed to quantify the ESW of SSEs using cells consisting of SE, sandwiched between a sodium metal counter electrode and a blocking working electrode.[105,106] The objective of these measurements is to identify the potential limits at which electrolyte decomposition occurs. However, the resulting decomposition currents are often weak and difficult to resolve, particularly when overshadowed by the substantially larger currents associated with sodium.[107,108] More reliable ESW determination can be achieved by separating the electrolyte decomposition process from sodium metal redox reactions. Furthermore, to ensure that ESW measurements accurately reflect practical battery operation, the test configuration should closely resemble the actual cell architecture.[108] This approach enables a more realistic assessment of the electrochemical stability of SEs under operationally relevant conditions.

As schematically represented in Fig. 8, the intrinsic electronic stability of a polymer electrolyte can be conceptually understood using a band-edge model, where the oxidation and reduction limits are approximated by the valence band maximum (VBM) and conduction band maximum (CBM), respectively.[109,110] This theoretical framework, often derived from first-principles calculations on the pure polymer matrix, serves as a computational baseline.[111] For a SIB, the electrolyte ESW must span the electrochemical potentials of both electrodes. This requires the energy difference between VBM and CBM to exceed the potential gap between the cathode (μC) and anode (μA, *e.g.*, Na/Na^+). Critically, the VBM must lie below μC and the CBM above μA to ensure both electrode potentials fall within the electrolyte stability range. Failure to meet these criteria can lead to oxidative or reductive decomposition at the interfaces. While resulting solid–electrolyte interphase (SEI) or cathode–electrolyte interphase (CEI) layers can be protective, they may also hinder Na^+ transport, ultimately compromising the cell cycling stability and lifespan. In practice, the true electrochemical stability window of a CPE is further governed by the salt anion, filler properties, and dynamic interfacial interactions. Consequently, the operational ESW must be validated experimentally using techniques such as LSV or cyclic voltammetry.

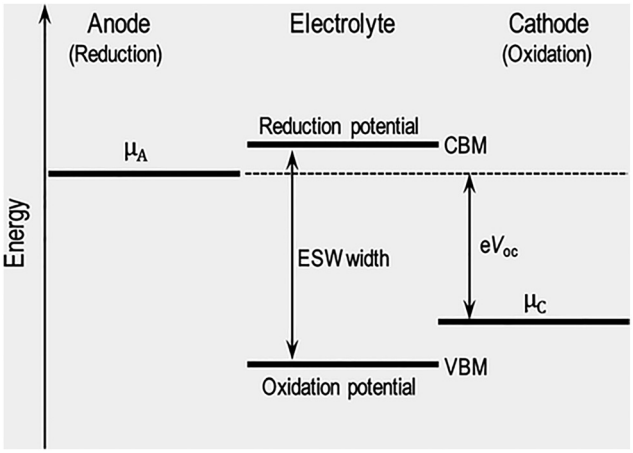

Fig. 8 Schematic representation of the electrolyte ESW as an energy profile at the electrolyte–anode/cathode interface, with the oxidation and reduction limits (VBM/CBM) serving as a computational baseline for the polymer matrix (reprinted with permission from ref. 111. Copyright © 2019 American Chemical Society).

5. Pathways of Na^+ ion transport in CPEs

In a solid polymer electrolyte containing a dispersed sodium salt, the transport mechanism of Na^+ ions closely resembles that of Li^+ ions in an SPE with a dispersed lithium salt. Specifically, Na^+ ions transfer through the polymer matrix by hopping between coordination sites, where they interact with polymer polar segments by Lewis acid–base interactions. This motion is driven by an applied electric field and facilitated by the segmental motion of the polymer chains as depicted in Fig. 9a.[112,113] Since segmental motion is limited to the amorphous state over the glass transition temperature (T_g), the SPEs' ionic conductivity is significantly affected by the T_g of the host polymer.[114] Most SPE host polymers are semicrystalline, so a common strategy to enhance ionic conductivity is to reduce crystallinity and increase the amorphous fraction through various approaches.[115] However, studies have also confirmed that ion migration can occur through crystalline domains of the polymer. This tendency has been established for specific polymer–salt crystalline complexes (especially PEO_6:Li_x-type phases) and is thus a viable, but special-case mechanism rather than a general rule for all SPEs/CPEs.[116,117] In these regions, ions move inside the tunnels formed by the helical conformations of polymer chains within the crystalline structure, as depicted schematically in Fig. 9b. Although the conductivities exhibited are too low for immediate technological application, their importance lies in demonstrating that ionic transport can occur in crystalline polymer matrices, independent of polymer segmental motion. These findings introduce an alternative paradigm for investigating ion transport in polymers and define a distinct class of solid electrolytes. Unlike conventional amorphous polymer electrolytes, ion conduction in these materials occurs within a rigid, structurally ordered environment, while

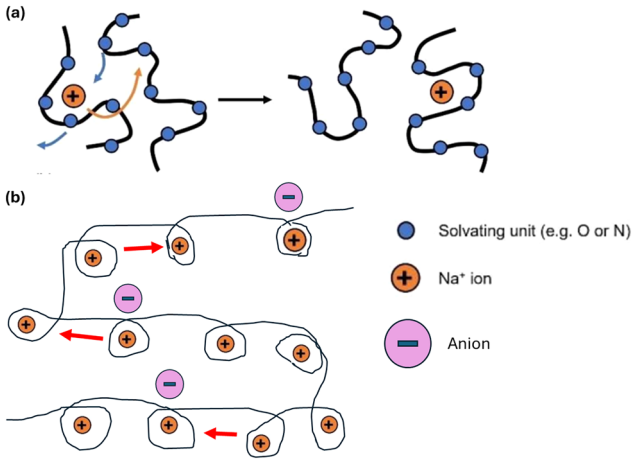

Fig. 9 Schematic representation of the ion transfer mechanism in (a) amorphous areas of the polymer (reprinted with permission from ref. 121 Copyright © 2021, Elsevier) and (b) in crystalline domains of the polymer.

remaining fundamentally different from crystalline ceramic electrolytes due to their soft polymeric nature.

Substituting lithium salts with sodium salts in SPEs leads to pronounced changes in electrochemical performance, arising from fundamental differences in ionic size, coordination chemistry, and ion–polymer interactions. Owing to its larger ionic radius, Na^+ exhibits weaker coordination with Lewis bases, such as ether oxygens in PEO, compared to Li^+, which, from a purely energetic standpoint, would be expected to facilitate faster ion transport and higher ionic conductivity. Contrary to this expectation, extensive experimental evidence demonstrates that PEO–Na^+ electrolytes consistently display lower ionic conductivities than their Li^+-based analogues, underscoring the complex and nontrivial nature of ion transport in polymer electrolytes.[118,119] Some reported investigations also reveal a complex interplay between polymer molecular weight, cation size, and coordination strength that critically governs ionic conductivity at room temperature. For example, high molecular weight (entangled) PEO systems, such as PEO:NaTFSI electrolytes, display lower conductivity than analogous Li-based SPEs.[120] This is because in high molecular-weight (entangled) PEO, the larger size of Na^+ leads to multiple Na^+–EO coordination contacts, which outweigh their weaker monomer-level interactions and ultimately slow ion-hopping dynamics. In contrast, in lower molecular weight (unentangled) PEO-based SPEs, where ion transport is primarily diffusion-controlled rather than segmentally assisted, the conductivity trend reverses ($\sigma_{NaTFSI} > \sigma_{LiTFSI}$). Here, the stronger EO–Li^+ coordination increases the effective hydrodynamic radius of Li^+, thereby reducing its mobility relative to Na^+.[120] Moreover, the relative transport behavior of Li^+ and Na^+ is highly sensitive to the chemical nature of the polymer host, while Li^+ exhibits stronger coordination in ether-based polymers such as PEO, Na^+ interacts more favorably with carbonyl-containing polymers, including PCL and PTMC. These findings underscore that ionic conductivity in polymer electrolytes is dictated not solely by the cation size but by a subtle balance among the cation charge-to-radius ratio, coordination chemistry, polymer architecture, and steric constraints imposed by the polymer matrix.

Fillers in CPEs, whether passive or active, influence the ionic conductivity pathways and mechanisms.[31] Passive fillers, such as metal oxide NPs, are not actively involved in ion transport but assist in modifying the polymer's structural properties at the particle/polymer interface that contributes to enhanced ion conductivity and electrochemical performance. The interaction between the polar segments in polymer chains and polar groups on the ceramic NP surface results in lowering the crystallinity, creating more disordered amorphous domains that favor ion mobility.[122,123] Also, the Lewis acid–base interactions between the filler and polymer at the interfacial area contribute to enhanced salt dissociation that increases free charge carrier concentration and improves ionic conductivity.[124,125] Thus, the particle/matrix interfacial region in CPEs with passive fillers is more conductive as compared with the matrix.

When designing composite polymer electrolytes with passive ceramic fillers, the resulting ionic conductivity is determined by a balance of three microstructural parameters: the thickness of the conductive polymer layer that forms at the ceramic/matrix interface, the size of the ceramic particles, and their volume fraction (Fig. 10). If the interfacial conductive layer is thin or the ceramic loading is low, the regions of enhanced conductivity surrounding each particle remain isolated, offering limited benefit to the overall ion transport, irrespective of particle size (Fig. 10a and b). A significant improvement occurs only when these regions percolate, forming continuous pathways for ion conduction. This percolation can be achieved by either increasing the thickness of the conductive polymer shell (Fig. 10c) or by raising the ceramic volume fraction to bring particles closer together (Fig. 10d). However, this second strategy has a drawback, as increasing the filler content introduces more non-conductive material that occupies volume without contributing to ion transport. Consequently, the optimal configuration emerges not from high filler loading, but from a synergistic balance: a low volume fraction of small ceramic particles that promote the formation of an extensive, interconnected network of a highly conductive polymer (Fig. 10e). This architecture maximizes continuous conduction pathways while minimizing obstructive dead volume.[126]

When designing CPEs with active (conductive) fillers, the system complexity increases significantly.[61,127] Beyond factors like ceramic volume fraction, particle size, and the extent of polymer affected by the filler, two additional parameters become critical: the intrinsic ionic conductivity of the filler itself and the resistance at the polymer/filler interface (Fig. 11a–c).[126] Overall ionic conductivity is governed by the combined contributions of the polymer and ceramic phases, the enhanced local conductivity of the polymer near the interface, and the resistances at both the polymer/filler and filler/filler contacts. For CPEs where the active fillers do not form a continuous network, the polymer/filler interface resistance is the dominant factor. A low interface resistance allows Na^+ ions to move readily between phases; even at low ceramic loadings, a

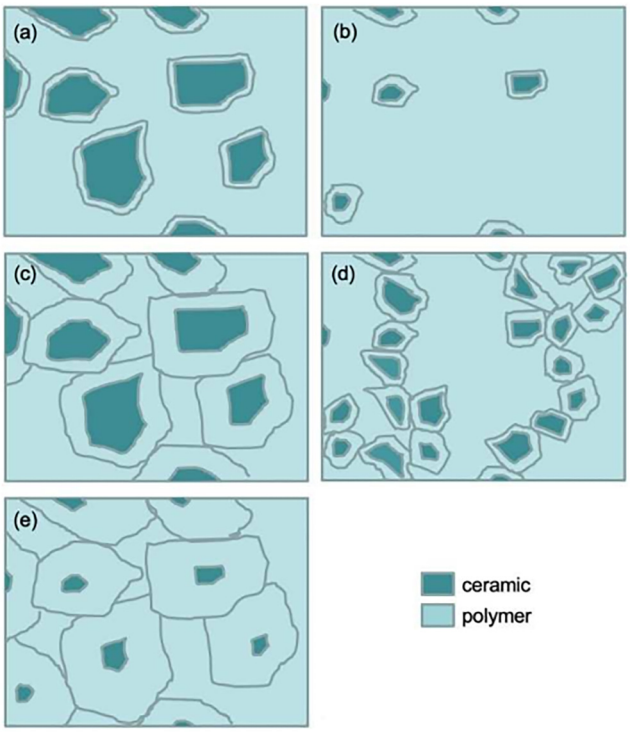

Fig. 10 Schematic representation of various scenarios of CPE microstructure interfacial regions with enhanced Na^+ ion conductivity. (a) and (b) CPEs having a narrow highly conductive interfacial region and low filler volume fractions; with this microstructure, the areas of the improved ionic conduction stay clearly separated, (c) CPEs with wider conductive interfacial zones, (d) CPEs with larger filler volume fractions; the areas of the improved conductivities resulting from engagement with separate particles intersect and supply continuous improved transport channels, and (e) CPEs with small volume fractions of passive fillers, small particles, but enlarged interfacial irregular areas of a high-conductivity polymer (reprinted with permission from ref. 126. Copyright © 2023 Wiley-VCH GmbH).

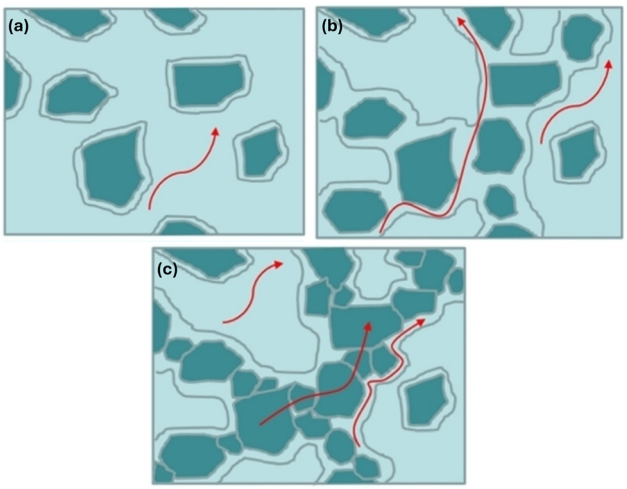

Fig. 11 (a)–(c) Three CPE situations with varying ceramic volume fractions (reprinted with permission from ref. 126. Copyright © 2023 Wiley-VCH GmbH).

significant portion of conduction can occur through the filler particles themselves. Conversely, a high interface resistance effectively blocks ion entry into the filler. In this case, conduction is confined to the polymer phase, specifically within the disordered, high-conductivity regions near the ceramic surfaces. The design objective then shifts toward maximizing the volume of this favorable polymer zone. When the ceramic particles form a percolating network, the nature of the conduction pathways changes. In this scenario, the resistance at the contacts between individual filler particles becomes a key parameter of performance. To illustrate these competing mechanisms, Fig. 11 presents three distinct microstructural scenarios with varying ceramic content. In the first (Fig. 11a), the ceramic volume fraction is too low to form any continuous pathway; either through the ceramic itself or *via* interconnected interfacial polymer zones. Na^+ ions are restricted to the bulk polymer matrix, leading to low overall ionic conductivity. The second scenario (Fig. 11b) represents an optimal balance, where the filler content is sufficient to create a continuous, high-conductivity network through the overlapping interfacial polymer regions, even though the ceramic particles themselves remain disconnected. This percolating interfacial pathway provides a new, fast channel for ion transport, substantially boosting overall conductivity. Finally, at high filler loadings (Fig. 11c), the particles form a direct, percolating ceramic network, where Na^+ ions can travel through three parallel pathways: the bulk polymer, the interfacial polymer zones, and the particle network itself, greatly facilitating migration. This wide array of possible conduction routes makes predicting and optimizing conductivity in CPEs with active fillers more challenging than in systems containing only passive fillers.[100,128]

Solid-state NMR is generally used to probe cation transport and dynamic processes in SPEs. Foran *et al.*[129] have published an excellent review on the use of solid-state NMR spectroscopy for the characterization of molecular structure and dynamics in solid polymer and hybrid electrolytes. However, the ^{23}Na nucleus, with a spin quantum number of 3/2, exhibits strong quadrupolar interactions that significantly influence its NMR behavior.[130] These interactions lead to short T_2 relaxation times, causing pronounced spectral line broadening, which renders direct measurements of sodium ion diffusion infeasible in SPEs/CPEs for SIBs. As a result, ^{23}Na NMR is inherently limited for direct diffusion studies in sodium-based systems. To overcome this limitation, a common methodological approach is to monitor the anionic counterion using a more amenable nucleus, such as ^{19}F.[131] Consequently, in these studies, cation dynamics and diffusion are inferred indirectly based on the self-diffusion results obtained from ^{19}F NMR. This indirect approach introduces uncertainty, as the behavior of cations is only approximated rather than directly measured. Pulsed field gradient (PFG) NMR spectroscopy is a key technique for measuring self-diffusion coefficients, which quantify the random, thermally driven translational motion of ions and molecules in materials such as polymer electrolytes.[129,132]

In lithium-conducting systems, this is commonly achieved by targeting the high-sensitivity nuclei ^{7}Li and ^{19}F to probe cation and anion mobility, respectively.[133] PFG NMR can also be applied to ^{1}H and ^{13}C nuclei to characterize polymer chain dynamics, which significantly influence overall ion transport.[134–136] The utility of PFG NMR for determining ionic transference numbers, a critical metric for electrolyte performance, depends critically on the system's dissociation state.[137] The key limitation of the PFG-NMR technique is that it provides an indistinguishable average diffusivity of all mobile NMR-visible species, including dissociated ions, neutral ion pairs, and charged clusters. Consequently, PFG NMR-derived transference numbers often exceed those obtained from electrochemical methods, such as the potentiostatic polarization technique, which selectively senses the flux of charged carriers.[137,138] As an example, in their work, Kaneko *et al.*[123] employed a combination of PFG NMR and impedance spectroscopy to investigate the dynamic transport properties of lithium-ion-based plasticized SPEs containing LiTFSI salt. By selectively observing ^{7}Li and ^{19}F, the PFG NMR technique provides separate diffusion coefficients for lithium-containing species and fluorine-containing species (primarily from the TFSI anion), offering species-specific insight into ionic mobility. To derive the lithium-ion transport number from these diffusion data, approximation methods are required because PFG NMR cannot distinguish between charged ions (*e.g.*, free Li^+) and neutral species (*e.g.*, non-dissociated LiTFSI ion pairs). A simple and common approach, proposed by Watanabe *et al.*,[139] assumes that the salt is fully dissociated and that interactions between ions are minimal. Under this ideal condition, the transport number (t_{Li}) is defined by Eqn 3, where the lithium-ion contribution is represented by the ratio of its diffusion coefficient to the sum of the cation and anion diffusion coefficients:

$$t_{Li} = \frac{D_{Li}}{D_{Li} + D_F} \tag{3}$$

where D_{Li} represents the diffusion coefficient of all lithium-containing species (both free Li^+ ions and any associated ion pairs) as measured by PFG NMR, while D_F represents the diffusion coefficient of all fluorine-containing species (primarily the TFSI anion). This value approximates the fraction of current carried by the lithium ion based solely on NMR-derived mobilities, but it is only accurate when the dissociation ratio is nearly unity (*i.e.*, a few ion pairs exist). However, when incomplete salt dissociation is present, the simple t_{Li} value can be misleading. To account for this, a more refined transport number, t_{Li^+}, is calculated using a model proposed by Angell *et al.*[140] This approach assumes that the diffusion coefficient of the non-dissociated Li salt (D_{LiF}) is equal to the measured D_F value. The expression for this corrected transport number is given by eqn (4):

$$t_{Li^+} = \frac{1}{2}\left(\frac{D_{Li} - 2D_F + \xi}{\xi - D_F}\right), \quad \text{where } \xi = \frac{RT\sigma_{imp}}{cF^2}. \tag{4}$$

Here, D_{Li} and D_F are the same NMR-derived diffusion coefficients as in eqn (4). The parameter ξ is a composite factor derived from electrochemical data, R is the gas constant, T is the absolute temperature, σ_{imp} is the ionic conductivity obtained from impedance spectroscopy, c is the volumetric molar concentration of the lithium salt in the electrolyte (in mol cm^{-3}), and F is the Faraday constant. The authors observed that t_{Li^+} values obtained from eqn (4) were consistently different from (specifically, lower than) the simple t_{Li} values obtained from eqn (3). This discrepancy arises due to incomplete salt dissociation. It should be noted that t_{Li} was obtained by assuming that the associated (non-dissociated) Li salt was immobile, effectively setting D_{LiF} = 0. in the more general expression. In contrast, the calculation of t_{Li^+} assumes equal diffusion coefficients for the anions and the associated Li salt, *i.e.*, $D_F = D_{LiF}$. These two assumptions represent extreme cases, and consequently, the real value of the transport number should lie somewhere between t_{Li} and t_{Li^+}. The magnitude of gap between these two values thus serves as an indicator of the degree of ion aggregation; a significant difference suggests substantial ion pairing and its associated mobility, while similar values would indicate near-complete salt dissociation. Discrepancies between transference numbers obtained from PFG NMR and electrochemical techniques can also be understood through the dissociation ratio of the ionic species.[141] As discussed above, since PFG NMR cannot distinguish between charged and neutral species, its measured diffusion coefficients include contributions from free ions, ion pairs, and larger aggregates. Consequently, transference numbers derived solely from NMR data are typically overestimated compared to those obtained from electrochemical methods.[141,142] When similar transference numbers are observed from both approaches, it suggests near-complete dissociation of the salt. This concept is illustrated by studies on LiTFSI-doped PEO, where transference numbers varied with the lithium-to-ether oxygen molar ratio (r). PFG NMR measurements yielded values between 0.17 and 0.30, while potentiostatic polarization experiments gave a range of 0.06 to 0.26. However, it should be noted that certain electrochemical methods can also be susceptible to overestimation under specific conditions. Sun *et al.*[143] demonstrated that in concentrated systems, potentiostatic polarization can induce diffusion of neutral species, artificially inflating the transference number. For instance, in a poly(trimethylene carbonate)-ε-caprolactone copolymer, they reported Li^+ transference numbers of 0.32 by PFG NMR and 0.66 by potentiostatic polarization. This discrepancy was attributed to the migration of neutral aggregates, an issue that could be circumvented by employing the Hittorf method, which provides more accurate transference numbers by directly measuring concentration changes.[144] PFG NMR studies have also demonstrated that Li^+ transference numbers depend on both polymer chain segmental motion and the affinity of lithium cations for the polymer matrix. Xu *et al.*[145] and Sun *et al.*[143] have shown that in PEO/LiTFSI SPE at high lithium loading, cation mobility is lower than anion mobility due to increased cation–polymer affinity. PFG NMR experiments have further confirmed that strategies aimed at enhancing segmental

motion, such as incorporating inert ceramic fillers[146,147] or increasing temperature,[148,149] can improve Li^+ mobility in polymer electrolytes.

Unlike for lithium systems, PFG NMR is rarely used for characterizing sodium-ion mobility in sodium-based SPEs. The rapid quadrupolar relaxation of the ^{23}Na nucleus leads to substantial line broadening and signal decay, rendering its signal impractical for detection in PFG NMR-based diffusion studies.[150] As a result, researchers turn to electrochemical characterization, most commonly potentiostatic polarization, to obtain reliable sodium transport numbers.[151] Electrophoretic NMR (eNMR) is a one-dimensional diffusion technique used to measure ion flow in liquid electrolytes and derive transference numbers.[152–154] Rosenwinkel and Schönhoff applied it to PEO–LiTFSI solid electrolytes, showing that cation mobility decreases with increasing salt content due to polymer–cation coordination.[152] eNMR-derived transference numbers (0.23, 0.19, and 0.15) closely matched PFG NMR values (0.21, 0.17, 0.17) at varying salt concentrations, indicating mostly free cations. As eNMR is less affected by ion pairs and agglomeration, it may provide more accurate transference numbers than PFG NMR in concentrated systems, making it particularly valuable for analyzing complex electrolytes such as hybrid systems containing active ceramics.[129] ^{23}Na is readily detectable by NMR but it exhibits very short spin relaxation times, making direct determination of electrophoretic mobilities and thus transference numbers for Na^+ by eNMR unfeasible. To address this limitation, Mönich *et al.*[155] introduced a novel approach that calculates transference numbers for ^{23}Na and other unmeasurable cations by combining eNMR and impedance spectroscopy, where anion mobility is obtained from eNMR, while total conductivity is determined *via* electrochemical impedance spectroscopy, enabling accurate calculation of cation transference numbers. Nevertheless, it is important to recognize that electrochemical methods such as potentiostatic polarization also rely on simplifying assumptions, including ideal ion dissociation and negligible ion–ion correlations. In practical electrolyte systems, the presence of ion pairing, aggregation, and correlated ion motion can lead to deviations from these assumptions, resulting in inaccurate or overestimated transference numbers. Therefore, care must be taken when interpreting values obtained from such techniques, particularly in highly concentrated or weakly dissociated systems.

To provide a clearer comparison of the methodologies used to determine cation transference numbers, a summary of key experimental techniques along with their advantages and limitations is presented in Table 2.

6. Composite polymer electrolytes with passive fillers

Na-free fillers, known as passive fillers, which do not facilitate ion transport through their bulk, have been widely investigated for their ability to increase the physical and electrochemical properties of CPEs for SIBs.[126,156] While inert oxide ceramic fillers, such as Al_2O_3, TiO_2, and SiO_2, and others lack intrinsic ionic conductivity, their incorporation into CPEs improves overall ionic conductivity, electrochemical stability, and mechanical integrity. This enhancement arises from a dual mechanism: first, they function as solid-state plasticizers that reduce host polymer crystallinity. Second, through Lewis acid–base interactions, the filler surfaces can adsorb anions, which promote the dissociation of salt ion pairs and consequently increase the concentration of mobile Na^+ ions within the electrolyte.[157] This section summarizes recent approaches adopted for enhancing the efficiency of CPEs using inert fillers for SIB applications.

Sahu *et al.*[158] investigated the effect of TiO_2 nanofiller particles in PEO/$NaPF_6$/TiO_2 CPE films. The base SPE system, with a composition of [80PEO:20$NaPF_6$], was prepared using a hot-press technique. To enhance its properties, nano-sized TiO_2 (<100 nm) was incorporated as a nanofiller to form a series of CPE films: [80PEO:20$NaPF_6$] + $x$$TiO_2$, where x = 1–9 wt%. As depicted in Fig. 12, the filler-dependent conductivity study identified the nanocomposite with 8 wt% TiO_2 as the optimized CPE composition, exhibiting the maximum conductivity of 3.53×10^{-6} S cm^{-1} at room temperature, which is approximately one order of magnitude greater than the conductivity of unfilled optimized SPE (7.78×10^{-7} S cm^{-1}). The overall ionic transference number (t_{ion}) and the cationic transference number (t^+) for the optimized CPE films were found to be ~0.99 and ~0.22, respectively. XRD analysis and DSC studies confirmed that the addition of TiO_2 reduced the crystallinity of the PEO matrix. This increase in the amorphous phase content directly correlates with the measured enhancement in ionic conductivity. Finally, an electrochemical cell was fabricated

Table 2 Comparison of experimental techniques for determining cation transference numbers (t^+)

Technique	Principle	t^+ Nature	Advantages	Limitations
Potentiostatic polarization (Bruce–Vincent method)	Steady-state current under applied DC polarization	Effective (electrochemical)	Simple, widely used, applicable to solid electrolytes	Can overestimate t^+ due to neutral species transport and interfacial effects
Hittorf method	Measures concentration change after current flow	True (based on mass balance)	More accurate, accounts for all species	Experimentally complex, time-consuming
PFG NMR	Measures self-diffusion coefficients of ions	Apparent (mobility-based)	Non-destructive, species-specific diffusion info	Cannot distinguish free ions *vs.* ion pairs, leading to overestimation
Electrophoretic NMR (eNMR)	Measures ion drift under an electric field	True (direct ion mobility)	Direct ion movement under an electric field	Requires specialized setup, low sensitivity
Impedance-based methods	Uses conductivity and modeling	Approximate	Easy integration with EIS data	Model-dependent, less reliable

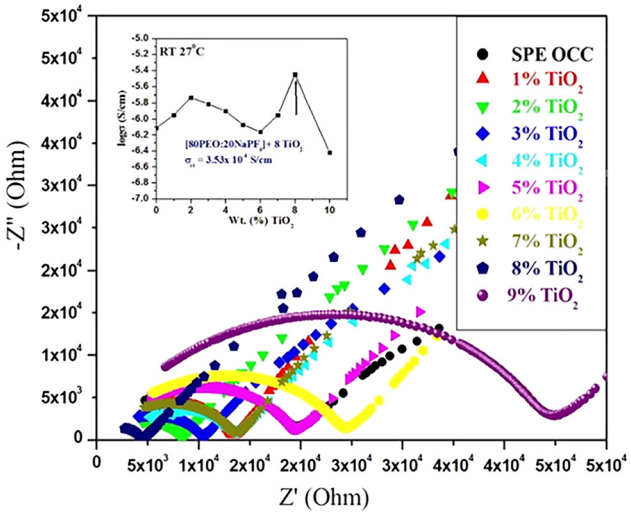

Fig. 12 Complex impedance plot (Z' *vs.* Z'') for the CPE system [(80PEO:20$NaPF_6$) + $x$$TiO_2$]. The inset presents the correlation of ionic conductivity with TiO_2 filler wt% (x) (reprinted with permission from ref. 158. Copyright © 2024 Wiley-VCH GmbH).

with optimized CPE, with a graphitic anode, and amorphous MnO_2 as the cathode. The CV results demonstrated stable electrochemical performance. The same group also reported PEO/PAN blend-based CPEs with TiO_2 nanofillers and $NaClO_4$ using a hot-pressing technique.[159] The optimum CPE composition [88(90PEO/10PAN) + 12$NaClO_4$ + 15TiO_2] exhibited an ionic conductivity of $\sim 1.05 \times 10^{-5}$ S cm^{-1} at ambient temperature. The temperature-dependent conductivity study revealed Arrhenius behavior having a small activation energy (E_a) of $\sim$0.22 eV for the optimal composition. Cyclic voltammetry measurements demonstrated an ESW from −3 to +3 V and exhibited excellent electrochemical reversibility and cyclability.

SiO_2, an abundant compound found in sand and agricultural waste such as sugarcane bagasse, serves as a valuable source of high-purity filler material.[160,161] In polymer electrolytes, SiO_2 enhances ionic conductivity by promoting salt dissociation and reducing crystallinity, thereby facilitating ion mobility.[162] To utilize eco-friendly materials and to reduce the cost of development, Nimah *et al.*[163] developed CPEs with a polyvinyl alcohol (PVA)/chitosan blend as the matrix, SiO_2 from bagasse ash as a filler, and $NaClO_4$ as a salt using a solution casting method. The highest conductivity of 3.00×10^{-4} S cm^{-1} was attained using 3PVA:2CS:4$NaClO_4$ and 5 wt% SiO_2, significantly improving from 1.08×10^{-4} S cm^{-1} without a filler for SPE. The enhancement in ionic conductivity of the CPE was attributed to the increase in matrix amorphicity induced by SiO_2 incorporation, as confirmed by XRD analysis. Nano-SiO_2 surface interactions improve polymer/filler interfacial stability, which inhibits polymer crystallization and leads to increased ionic conductivity in the CPE.[164] The same group also reported CPEs based on PEO/$NaClO_4$ and nano-SiO_2 derived from sugarcane bagasse.[165] Similarly, in this system, nano-SiO_2 enhances free volume and improves salt dissociation, leading to more mobile ions and improved conductivity. Compared to Al_2O_3 and TiO_2, SiO_2 shows stronger Lewis acidity and higher surface area, which explains its more pronounced impact on polymer chain relaxation and ion dissociation at similar loadings.[166]

Hydroxyapatite (HAP, $Ca_{10}(PO_4)_6(OH)_2$) is a thermodynamically resilient calcium orthophosphate under physiological conditions.[167,168] Its chemical and physical similarity to natural bone and teeth makes synthetic HAP a material of interest for biomedical applications.[169,170] In the past few years, HAP has been explored as a passive filler in SPEs, where it promotes salt dissociation *via* Lewis acid–base interplay, improving mechanical properties and ionic conductivity. For instance, in CPEs for LIBs, HAP improves conductivity and cycling efficiency,[171] while in PEO-based electrolytes with succinonitrile as a plasticizer, it contributed to a maximum ionic conductivity of roughly 10^{-3} S cm^{-1}.[172] Due to the above benefits of HAP as a passive filler, Abouricha *et al.*[173] prepared HAP *via* a co-precipitation method, yielding a somewhat low calcium powder, and incorporated it as a filler into a PEO/NaTFSI matrix as a CPE for SIBs. The inclusion of HAP significantly improved Young's modulus (1.98 ± 0.79 MPa) and tensile strength (3.63 ± 0.33 MPa), which is beneficial for dendrite suppression and cycle stability. Electrochemical characterization revealed an ionic conductivity over 10^{-4} S cm^{-1} at high temperatures (60–80 °C), $t_{Na^+} \sim 0.38$, and a broad ESW of 1.0–5.10 V. The authors attributed this conductivity improvement to enhanced NaTFSI salt dissociation, which is facilitated by Lewis acid–base interactions between the hydroxyl groups on the HAP surface and the salt. To evaluate the compatibility with Na metal electrodes, symmetric Na|CPE|Na cells were cycled for 160 hours at 70 °C under a current density of 0.05 mA cm^{-2}. As depicted in Fig. 13, the pristine PEO/NaTFSI SPE cell exhibited a high overpotential of 369 mV and experienced a short circuit following 32 h. In contrast, the cell incorporating PEO/NaTFSI with a 15% HAP filler maintained a stable and significantly lower overpotential of 88 mV throughout the entire test, showing no indication of short circuit. This markedly improved performance demonstrates that the enhanced mechanical properties of CPEs with HAP as a filler effectively suppress sodium dendrite formation and propagation. When paired with a $Na_4CrFe(PO_4)_3$ cathode and a sodium metal anode, the CPE provided a specific discharge capacity of 124 mAh g^{-1} at the fifth cycle (C/20 rate). These results underscore the potential of HAP as an effective filler in SPEs for medium to high temperature SIBs, providing a platform for further interface optimization and system development.

Fillers with high aspect ratios (fibers) form continuous conductive networks, whereas low-aspect-ratio particles (*e.g.*, nanoparticles) result in isolated interfaces with limited conductivity enhancement in SPEs.[174,175] Moreover, particle agglomeration causes uneven ion flux, promoting dendrite growth and reducing cycling stability.[174] Electrospun nanofiber membranes, with their 3D networks, offer a promising alternative by improving mechanical strength and enabling uniform ion distribution and enhanced ion conductivity.[176] Another major challenge in solid electrolytes is the low Na^+ ion transference number due to anion mobility and ion-pairing effects.

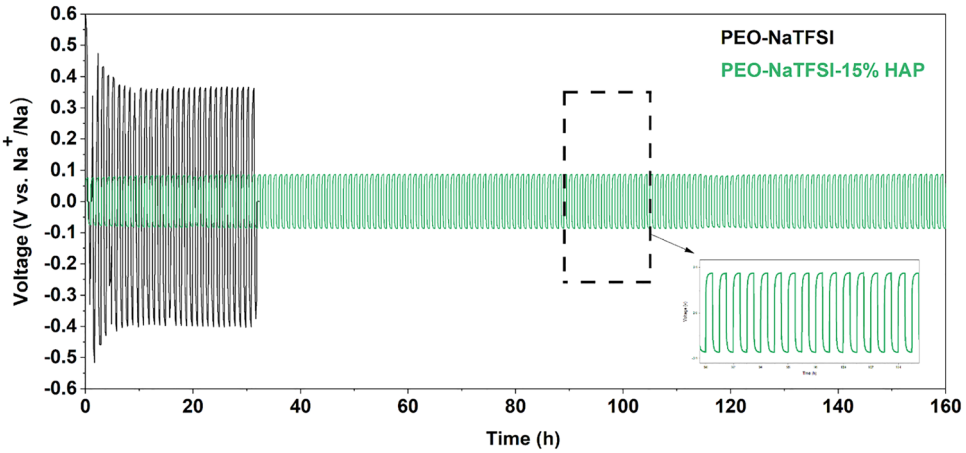

Fig. 13 Voltage profiles of symmetric Na|PEO–NaTFSI|Na and Na|PEO–NaTFSI-15% HAP|Na cells during galvanostatic cycling at 70 °C under a current density of 0.05 mA cm^{-2} (reprinted with permission from ref. 173. Copyright © 2024 Elsevier Ltd).

To counter the demerits of nanoparticles and to simultaneously enhance the Na^+ ion transference number of CPEs for SIB applications, various strategies have been adopted. For instance, Wu *et al.*[177] fabricated a nanofiber CPE with electrospun ceramic (SiO_2) nanofibers (SNF) functionalized to immobilize anions (SNF@IA) embedded in poly(2-(methacryloyloxy)ethyl 3-oxobutanoate) (PAAEM) (Fig. 14a and b). This CPE architecture facilitates ionic conduction through two primary mechanisms: (1) ion migration along the ceramic/polymer interface and (2) a coordination–dissociation process with

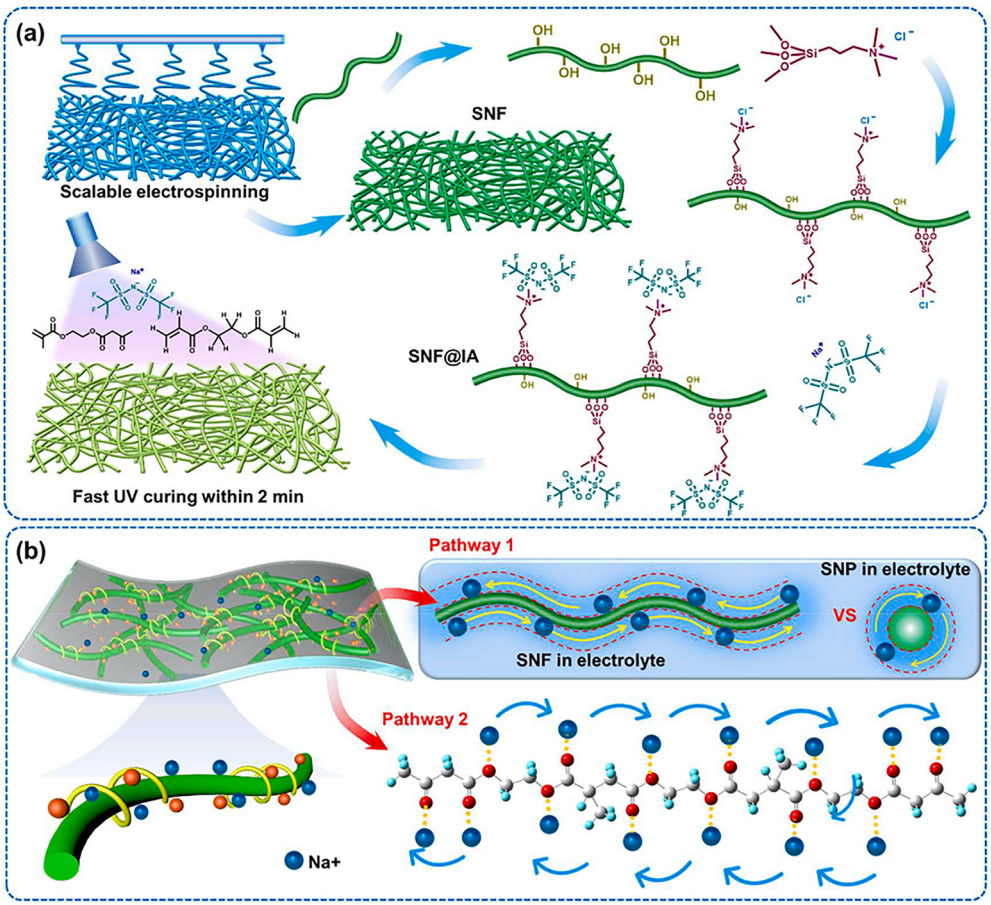

Fig. 14 (a) Manufacturing workflow for the PAAEM-SNF@IA membrane. (b) Model illustrating the mechanistic basis of ionic conduction, featuring dual transport pathways (reprinted with permission from ref. 177. Copyright © 2024 Elsevier B.V. All rights reserved).

the polymer's oxygen-based groups (C═O). The anion stabilization impact of the modified SNF@IA further increases the Na^+ transference number. Furthermore, its 3D network also promotes uniform distribution, preventing dendritic growth. In contrast to oxide nanoparticles that primarily affect crystallinity and salt dissociation, nanofibers modify ion pathways by providing continuous ion conducting channels, which minimizes barriers to ion transport and explains their superior performance at lower filler contents. Finally, the system exhibits wide temperature adaptability, achieved through the inherent minimal flammability of the ceramic SNF and the significantly suppressed T_g of the host PAAEM. The electrolyte demonstrated superior ionic conductivity (0.75×10^{-4} S cm^{-1} at −40 °C), $t_{Na^+} = 0.72$, and stable stripping/plating over 5400 h. In a Na cell, it retained 90.2% capacity after 1500 cycles and enabled pouch cells having an energy density of 162.6 Wh kg^{-1}.

In another study conducted by Kmiec *et al.*[178] employing a glass-fiber membrane as a matrix, they fabricated thin and mechanically robust CPE films by *in situ* UV-polymerizing poly(ethylene glycol) diacrylate (PEGDA) with PEG as a plasticizer and NaFSI salt. The resulting ∼50 μm mechanically robust membrane exhibited ionic conductivity with 50 wt% of PEG content up to $10^{-3.8}$ S cm^{-1} at 60 °C and stable sodium metal cycling (0.67 mA cm^{-2} at 60 °C) and retained 70% capacity following 50 cycles at C/5 in a full cell operation with a $Na_{2/3}Ni_{1/3}Mn_{2/3}O_2$ cathode and Na anode. High PEG content improves chain flexibility and free volume, resulting in quicker Na^+ transfer and higher conductivity. Meanwhile, the glass-fiber framework supports the membrane, reducing dendritic penetration and promoting long-term cycling and capacity retention. Here, the glass-fiber scaffold acts purely as mechanical reinforcement rather than participating in Lewis acid–base interactions or crystallinity suppression, illustrating that the filler can be performance-relevant even without altering ion transport chemistry.

Metal–organic frameworks (MOFs) and covalent organic frameworks (COFs) have gained significant recognition because of their capability to improve electrolyte efficiency by restricting anion transport, decreasing concentration polarization, and homogenizing the electric field profile.[179,180] To exploit these characteristics for improving the electrochemical performance of CPEs for SIBs, Guo *et al.*[181] introduced a boron-containing structured CPE (BSCPE) designed to selectively enhance Na^+ transport by embedding an anion-trapping boron-based COF (B-COF) network within a PEO matrix. As depicted in Fig. 15a, the abundant boron Lewis-acid sites on the B-COF framework effectively immobilize $TFSI^-$ anions, simultaneously promoting salt dissociation and increasing the Na^+ transference number. Furthermore, the *in situ* growth of well-ordered B-COF nanosheets on a glass fiber scaffold created continuous pathways for rapid and selective Na^+ transport. This unique microstructure, combined with the enhanced amorphization of the PEO matrix, resulted in an excellent ionic conductivity of 5.28×10^{-4} S cm^{-1} at 60 °C and a high t_{Na^+} value of 0.71. The improved ion transport and interfacial properties were substantiated by MD simulations and DFT calculations, which confirmed the strong anion-trapping effect and optimized Na^+ coordination environment. Finite element simulations showed reduced concentration polarization and uniform electric field distribution, contributing to exceptional interfacial stability. As a result, the Na‖BSCPE‖Na symmetric cell displayed consistent plating/stripping for up to 8800 h (0.1 mA cm^{-2}) with minimal polarization. In all-solid-state SIBs, the BSCPE enabled outstanding cycling efficiency, retaining 81.2% capacity following 1200 cycles at 1C (Fig. 15b–e).

Similarly, to evaluate the effect of MOFs, Guan *et al.*[182] engineered a zirconium-based MOF functionalized with sodium sulphate and designed a CPE system through a solution-mediated process where PEO chains were infiltrated into the pores of the prepared sodium sulphate grafted MOF. The prepared sodium sulfate grafted-MOF framework provides a high surface area and precisely sized pores that restrict anion movement while permitting small Na^+ and PEO segments to move through. The zirconium sites of the framework act as Lewis acid centers, effectively anchoring anions.[183] Furthermore, the restriction of PEO in the MOF pores suppresses polymer crystal regeneration, enhancing the amorphous regions conducive to ion conduction. The grafted $–SO_3Na$ groups additionally improve Na^+ ion transport efficiency by improving the transference number and Na^+ conductivity. Thus, with this framework, the CPE, even with low filler content (5 wt%), displayed a high Na^+ transference number of 0.67 and ionic conductivity of 6.62×10^{-4} S cm^{-1} at 60 °C, and ESW approaching ∼5.0 V. The improved ESW is due to the inherent high potential resistance of the designed filler. All solid-state assembled cells with the designed CPE retained a capacity of 82.8% following 1000 cycles at 1C and offered a superior cycling stability. Still at increased rates of 4C and 2C, the cells retain 95.86% and 91.1% capacity after 500 cycles, respectively. The corresponding pouch cell exhibited superior safety and stability, with a capacity retention of 97.03% after following cycles at 1C, outperforming most reported CPEs.

Graphitic carbon nitride (g-C_3N_4), with its 2D structure and surface-terminating $–NH_2$/–NH groups, is a promising nanofiller for polymer electrolytes due to its rich Lewis basic sites, intrinsic polarity, and negligible electronic conductivity.[184] Its surface nitrogen atoms interact with metal salts, enhancing salt dissociation, while inherent defects provide channels for vertical ion transport, boosting overall ionic conductivity.[185] Furthermore, strong interactions between g-C_3N_4 nanosheets and the polymer matrix inhibit chain slip, significantly improving mechanical strength.[186] The efficacy of g-C_3N_4 was first demonstrated in LIBs.[184,187] As an example, Sun *et al.*[185] investigated a PEO/g-C_3N_4 Li^+-CPE having a tensile modulus of 65.7 MPa and an ionic conductivity of 10^{-5} S cm^{-1} at 30 °C; a $LiFePO_4$|Li cell exhibited 161 mAh g^{-1} at 0.2C (60 °C), retaining 155 mAh g^{-1} after 100 cycles. The addition of g-C_3N_4 introduces Lewis base sites that facilitate salt dissociation while restricting polymer crystallinity, explaining the increased conductivity and mechanical strength. Engineering the g-C_3N_4 structure itself, such as creating porous nanosheets, can regulate Li^+ distribution to mitigate dendrites, yielding a CPE having a minimal

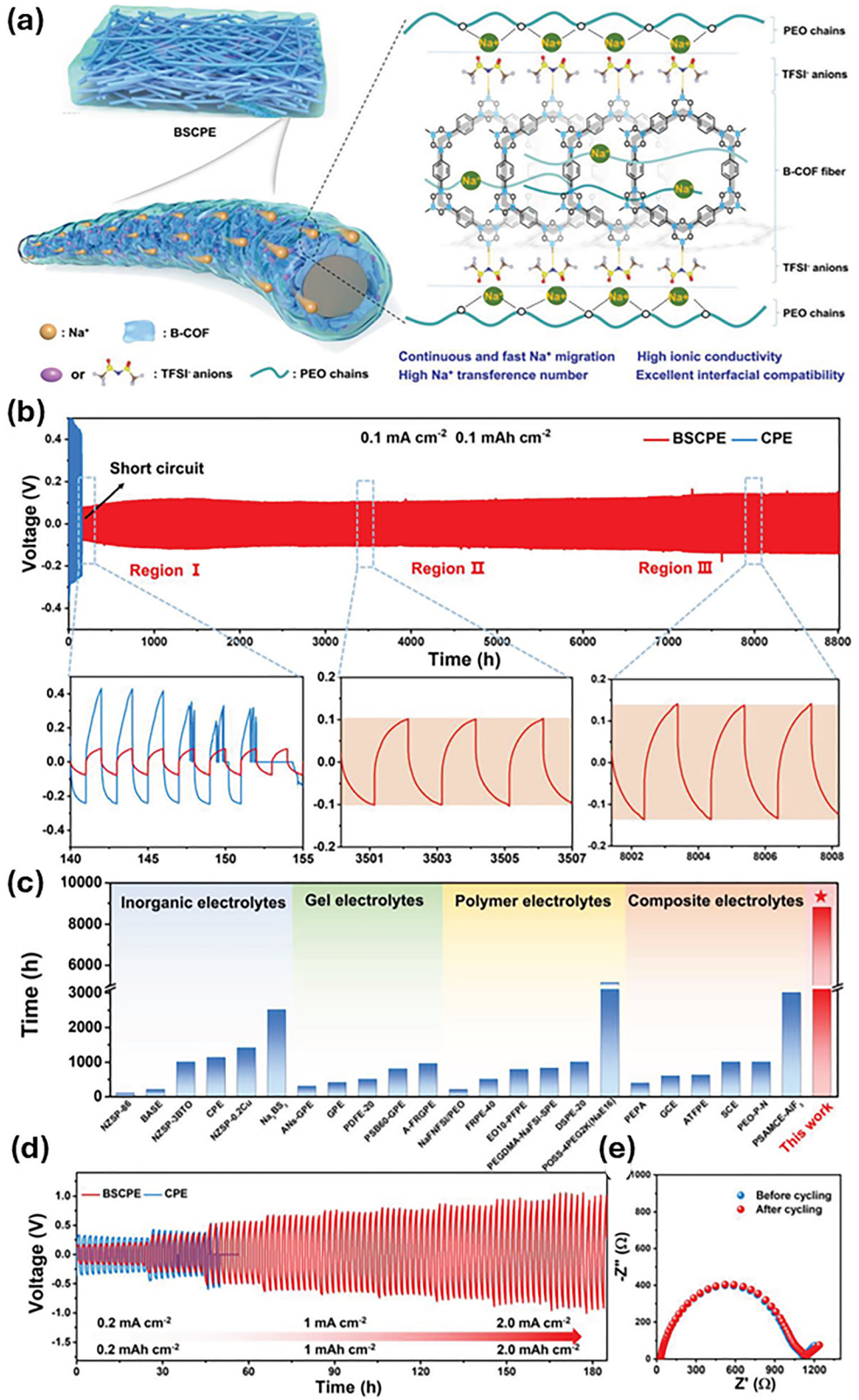

Fig. 15 (a) Schematic depiction of the B-COF structure within the CPE, highlighting its role in enabling selective and rapid sodium-ion (Na^+) transport. (b) Extended cycling durability of Na/Na symmetric cells having BSCPE and conventional CPE at 0.1 mA cm^{-2} (1 h per cycle, 60 °C); insets show detailed views of specific cycling stages. (c) Plating/stripping stability comparison of ASSMBs employing various electrolyte types. (d) Rate efficiency of Na/Na symmetric cells with BSCPE and CPE electrolytes, tested at current densities ranging from 0.2 to 2 mA cm^{-2} (60 °C). (e) EIS plot for the Na/BSCPE/Na cell before and after 100 cycles at 0.1 mA cm^{-2} (60 °C) (reprinted with permission from ref. 181. Copyright © 2024 Wiley-VCH GmbH).

capacity fading of 0.05% per cycle and conductivity up to 10^{-4} S cm^{-1}.[188] Focusing on the same aspects, Shu *et al.*[189] pioneered the application of g-C_3N_4 nanosheets as a nanofiller in PVDF–HFP/$NaClO_4$ CPEs for SIBs. The g-C_3N_4 filler modifies the CPE by reducing polymer crystallinity and promoting sodium salt dissociation *via* surface nitrogen atom interactions. This results in simultaneously enhanced ionic conductivity, mechanical properties, and thermal stability. When applied in a Na|g-C_3N_4-CSPE|$Na_3V_2(PO_4)_3$ (NVP) cell, the system demonstrated rapid Na^+ transfer and inhibited dendrite production. This yielded a minimal polarization voltage of 90 mV and a consistent reversible capacity of 93 mAh g^{-1} following 200 cycles at 1C, showcasing excellent cycling stability. The g-C_3N_4's homogeneous Na^+ flux eliminates concentration gradients at the interface, suppressing dendritic development and ensuring long-term cycle stability. Reduced graphene oxide (rGO), another 2D nanomaterial, has also been explored as a nanofiller in CPEs for SIBs.[190]

A key strategy to improve ionic conductivity involves incorporating ceramic fillers with high dielectric constants, such as TiO_2,[191] $SrBi_4Ti_4O_{15}$,[192] and $BaTiO_3$ (BTO),[193] which facilitate salt dissociation and enhance ion mobility. Dielectric nanoparticles decrease the activation energy by establishing effective ion transport channels in the polymer matrix. Additionally, dielectric particles have been shown to facilitate Li^+ transfer by functioning as Lewis acids and restricting the mobility of anions.[192] Exploiting the high dielectric constant character, Jeya *et al.*[194] investigated the influence of strontium titanate ($SrTiO_3$) on the Na^+ ion conductivity of PVDF–HFP/NaTF-based SPE. $SrTiO_3$ is paraelectric at room temperature, offering a high dielectric constant alongside low dielectric loss. The room temperature ionic conductivity dramatically increased by 10^3 times, from 4.19×10^{-7} S cm^{-1} for the SPE with no filler to a maximum of 1.83×10^{-4} S cm^{-1} with the incorporation of 6 wt% $SrTiO_3$ (Fig. 16). This improvement is primarily ascribed

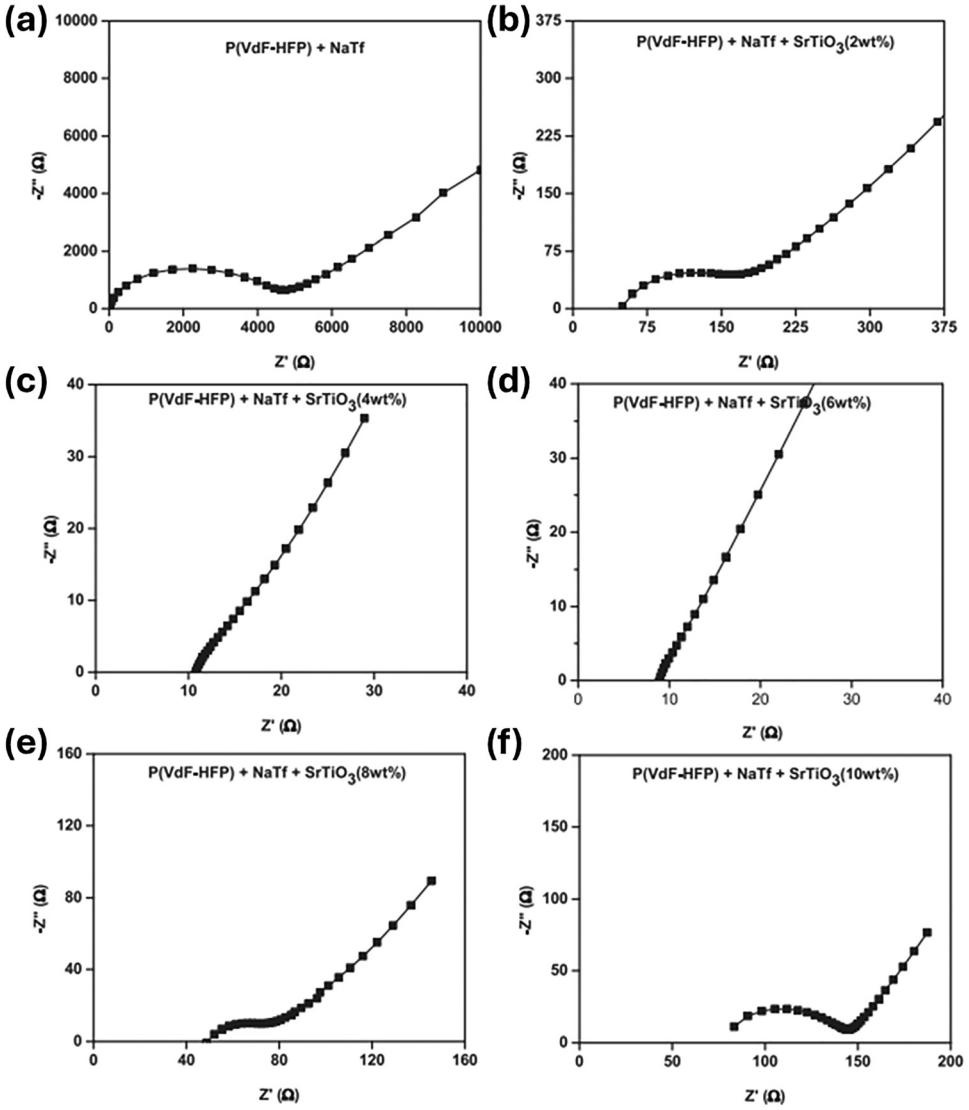

Fig. 16 Nyquist plots for the P(VdF-HFP)-NaTf polymer electrolyte with varying concentrations of $SrTiO_3$ filler. (a) 0 wt%, (b) 2 wt%, (c) 4 wt%, (d) 6 wt%, (e) 8 wt%, and (f) 10 wt% (reprinted with permission from ref. 194 Copyright © 2023 Elsevier B.V. All rights reserved).

to the high dielectric constant ($\varepsilon \approx 300$) of $SrTiO_3$, which, as dictated by Coulomb's law ($F \propto 1/\varepsilon$), reduces the attractive forces between polymer chains and ions and between the ions themselves. This weakening of interactions promotes greater dissociation of salt, liberating a higher concentration of mobile Na^+ cations.

Barium titanate ($BaTiO_3$) is a ferroelectric material [a type of material that exhibits spontaneous polarization, which can be reversed by applying an external electric field] renowned for its exceptionally high permittivity. These properties originate from its non-centrosymmetric perovskite crystal structure. In view of such properties, Sadiq *et al.*[195] developed sodium-ion conducting PVA/PEG blend-based CPEs with a sodium nitrate salt and $BaTiO_3$ as a nanofiller employing a solution casting method. Their analysis confirmed that the $BaTiO_3$ nanofiller interacts with the Na ions and polymer chains. The optimized composite, containing 15 wt% $BaTiO_3$, exhibited a transference number of 0.96, an ESW of ~4.1 V, and a maximum ionic conductivity of $\sim 1.035 \times 10^{-4}$ S cm^{-1} at 30 °C. The practical applicability of this optimized electrolyte was evaluated in electric double-layer capacitors. The assembled cell exhibited a capacitive charge storage mechanism with a specific capacitance of nearly 4.4 F g^{-1} with a scan rate of 3 mV s^{-1}. The device demonstrated an energy density of 27.7 Wh kg^{-1} and a power density of 9972 W kg^{-1} with stable performance sustained over 100 cycles. The same group developed CPEs by incorporating varying quantities of $CaTiO_3$ as a nanofiller in an environmentally friendly PVA/cellulose polymer blend, where they achieved a maximum conductivity of 9.76×10^{-5} S cm^{-1} for the optimized electrolyte composition ($CaTiO_3$ of 2 wt%) at 25 °C. It is to be mentioned that although $CaTiO_3$ shares a similar bonding and composition with ferroelectric titanates like $BaTiO_3$ and $PbTiO_3$, it does not undergo ferroelectric transitions. Instead, it is classified as an incipient ferroelectric, like $KTaO_3$ and $SrTiO_3$, meaning that it possesses a polar soft mode, but quantum fluctuations suppress the long-range ordering required for a ferroelectric phase transition (it does not undergo a spontaneous ferroelectric phase transition at room temperature).

7. Composite polymer electrolytes with active fillers

The development of CPEs for SIBs has been significantly advanced by incorporating active fillers, which offer distinct advantages over traditional inert fillers. These fillers, characterized by inherent structural defects and low activation energies, facilitate ionic conductivity through the bulk structure *via* the hopping mechanism, directly contributing to the ion transport process.[196,197] Furthermore, active fillers provide additional Na^+ ions to the electrolyte, increasing the charge carrier concentration. This strategy, widely utilized in lithium-ion batteries to enhance polymer electrolytes, has also been applied to SIBs using NASICON-type materials, such as $Na_3Zr_2Si_2PO_{12}$[198] and $Na_3Zr_{1.8}Mg_{0.2}Si_2PO_{12}$,[199] along with other sodium-ion conductors like $Na_2Zn_2TeO_6$.[200] By taking advantage of the unique properties of active fillers, this approach addresses key challenges in SIBs, including interfacial resistance and low ionic conductivity, while offering a pathway to develop high-performance energy storage systems.[201,202] Senthilkumar *et al.*[61] have recently published an excellent review on NASICON-type filler incorporated CPEs for SIBs. Active fillers play a direct role in Na^+ migration, establishing distinct ion-transport channels compared to passive fillers that rely on crystallinity reduction, Lewis-acid interactions, and mechanical reinforcing.

7.1. NASICON type fillers

To investigate the effect of NASICON-type active fillers, Wang *et al.*[203] fabricated (using an electrospinning technique) NASICON-type nanofibers (NFs) ($Na_{3.3}La_{0.3}Zr_{1.7}Si_2PO_{12}$ (NLZSP)). The prepared NFs were subjected to (i) ball milling (S-NFs) (Fig. 17a), which resulted in NFs with a smaller size (average length 1 μm) and lower aspect ratio and (ii) ultrasonic treatment (L-NFs) (Fig. 17b) with lengths generally exceeding 3 μm. Three CPE systems based on PVDF–HFP with (i) ceramic powder (CP), (ii) S-NFs, and (iii) L-NFs as nanofillers were prepared. It was demonstrated that NLZSP S-NF-containing CPE exhibits markedly greater ionic conductivity as compared to the CP-based CPEs. This enhancement was primarily attributed to the smaller size, more homogeneous dispersion capability, and higher aspect ratio of NLZSP S-NFs. This comparison demonstrates that as the filler geometry becomes more elongated, the percolation threshold is reached more efficiently, allowing the development of continuous ion-conducting networks that bulk particles cannot achieve at comparable loads. The highest performance was, however, exhibited by NLZSP L-NF-based CPEs with ESW > 5 V, a superior ionic conductivity of 3.36×10^{-4} S cm^{-1} at ambient temperature, a Na^+ ion transference number of 0.65, and a lower value of E_a (0.28 eV). The superior ionic conductivity of L-NFs having a maximum aspect fraction was attributed to the capability of NLZSP L-NFs to interconnect easily, creating a continuous 3D ion-conductive structure, as depicted in Fig. 17d. NLZSP L-NFs displayed uniform distribution in the polymer matrix (Fig. 17c). The results reveal that high-aspect-ratio NASICON nanofibers have lower activation energies and greater t_{Na^+} values than particle NASICON fillers, highlighting the importance of geometry-controlled percolation in determining total conductivity and transference number. Schematic illustration of the conduction pathways in the developed CPEs is depicted in Fig. 17e–g for ceramic powder, S-NF, and L-NF based CPEs, respectively. Furthermore, CPE with L-NFs also displayed good stress–strain properties with a break elongation of 104.4% and a tensile strength of ~10.66 MPa. To achieve the maximum potential of a CPE with a wide ESW, high-voltage, high-energy-density cathodes are also essential. The $Na_4MnCr(PO_4)_3$@C (NMCP@C) cathode demonstrates the highest reported energy density among these cathodes.[204] However, given its low ionic conductivity, coarse particles, and agglomeration issues, a high proportion of conductive additives

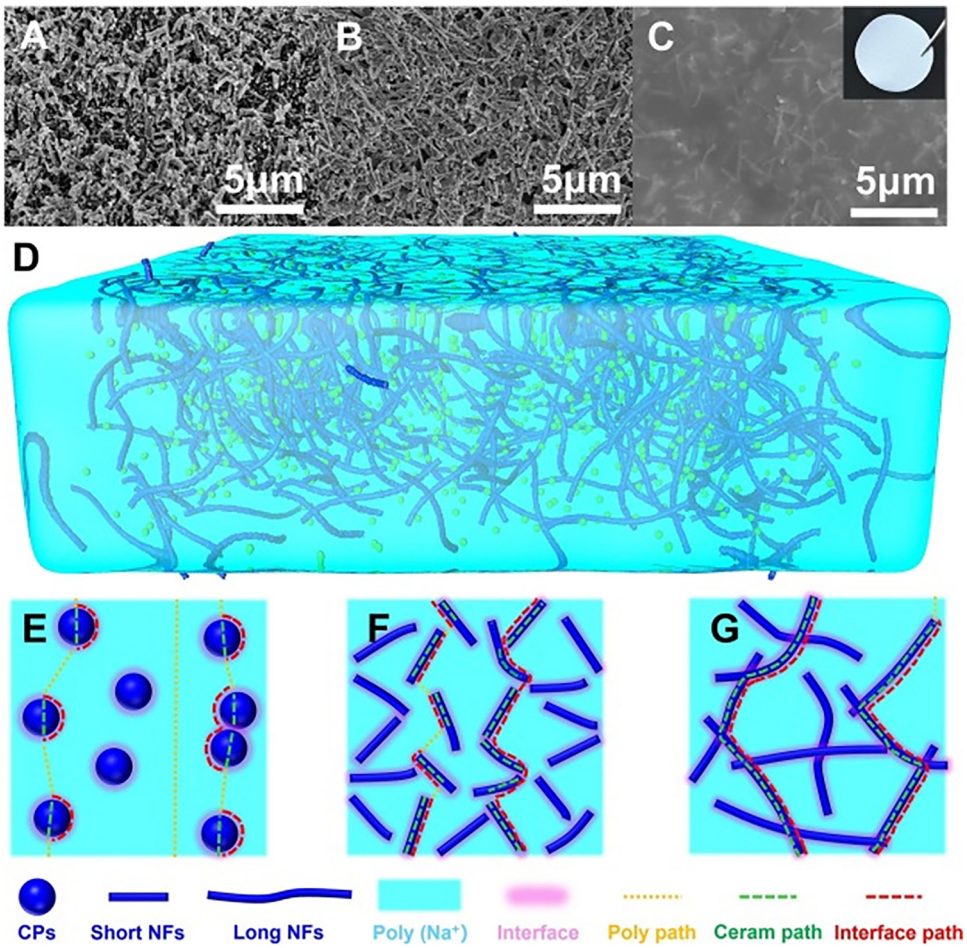

Fig. 17 SEM micrographs of (A) NLZSP S-NF, (B) NLZSP L-NF, and (C) the exterior of (PVDF–HFP)–$NaClO_4$–NLZSP S-NF CPEs (inset: image of the CPE). Schematics illustrating (D) (PVDF–HFP)–$NaClO_4$–NLZSP L-NF CPE and (E)–(G) Na-ion transport channels in CPEs (reprinted with permission from ref. 203. Copyright © 2024 Elsevier B.V. All rights reserved).

(20 wt%)[205,206] is required in the electrode, which results in a significantly lower energy density of the battery. To overcome these drawbacks, the authors fabricated non-agglomerating NMCP@C NFs with reduced diameters *via* electrospinning, which demonstrated remarkable electrochemical performance, delivering a maximum specific capacity of 161 mAh g^{-1} and an energy density of 534 Wh kg^{-1} at a rate of 0.1C, attributed to their enhanced electronic conductivity and short Na^+ ion migration path. The elongated NMCP@C skeleton improves ionic conductivity, while the reduced fiber diameter decreases ion diffusion distances. When integrated into an NMCP@C/CPE//Na ASSSMB, the system showed superior rate efficiency and cycling stability, retaining 70.5% of its capacity at 0.5C (1.4–4.6 V) and 78.8% of its capacity at 1C (1.4–4.3 V) after 200 cycles.

The ionic conductivity of a NASICON-type ceramic filler can be further enhanced through Mg substitution.[207] For instance, Zhang *et al.*[199] prepared NASICON structured $Na_{3.4}Zr_{1.8}Mg_{0.2}Si_2PO_{12}$ through a sol–gel process that was incorporated into PEO/$Na(CF_3SO_2)_2N$ (NaTFSI)-based electrolyte to achieve flexible CPE films *via* a solution cast technique for solid-state SIBs. Proposed ion conduction pathways for these CPEs are shown in Fig. 18a, depicting three possible pathways for Na^+ ion transport. The CPE showed a maximum ionic conductivity of 6.0×10^{-5} S cm^{-1} at ambient temperature and 2.8 mS cm^{-1} at 80 °C with 50 wt% NASICON quantity (Fig. 18b). The conductivity enhancement was attributed to the synergistic effect of the following four factors: first, NASICON ceramic fillers reduce crystallinity (confirmed by DSC analysis) and increase polymer chain mobility, expanding the ion-conducting regions while boosting carrier mobility. Second, the percolation effect contributes significantly to conductivity enhancement by creating extensive, interconnected transport pathways along NASICON particle surfaces (SEM analysis shows that at 50 wt% NASICON content, the particles form continuous and interconnected junctions, creating an efficient ion transport pathway). Third, the concentration gradient between highly conductive NASICON particles and the polymer matrix promotes Na^+ absorption by PEO (which strongly dilutes salts), increasing Na^+ vacancies on NASICON surfaces and accelerating interfacial ion transport. Fourth, the high bulk conductivity of NASICON ceramics further elevates the overall CPE membrane conductivity.

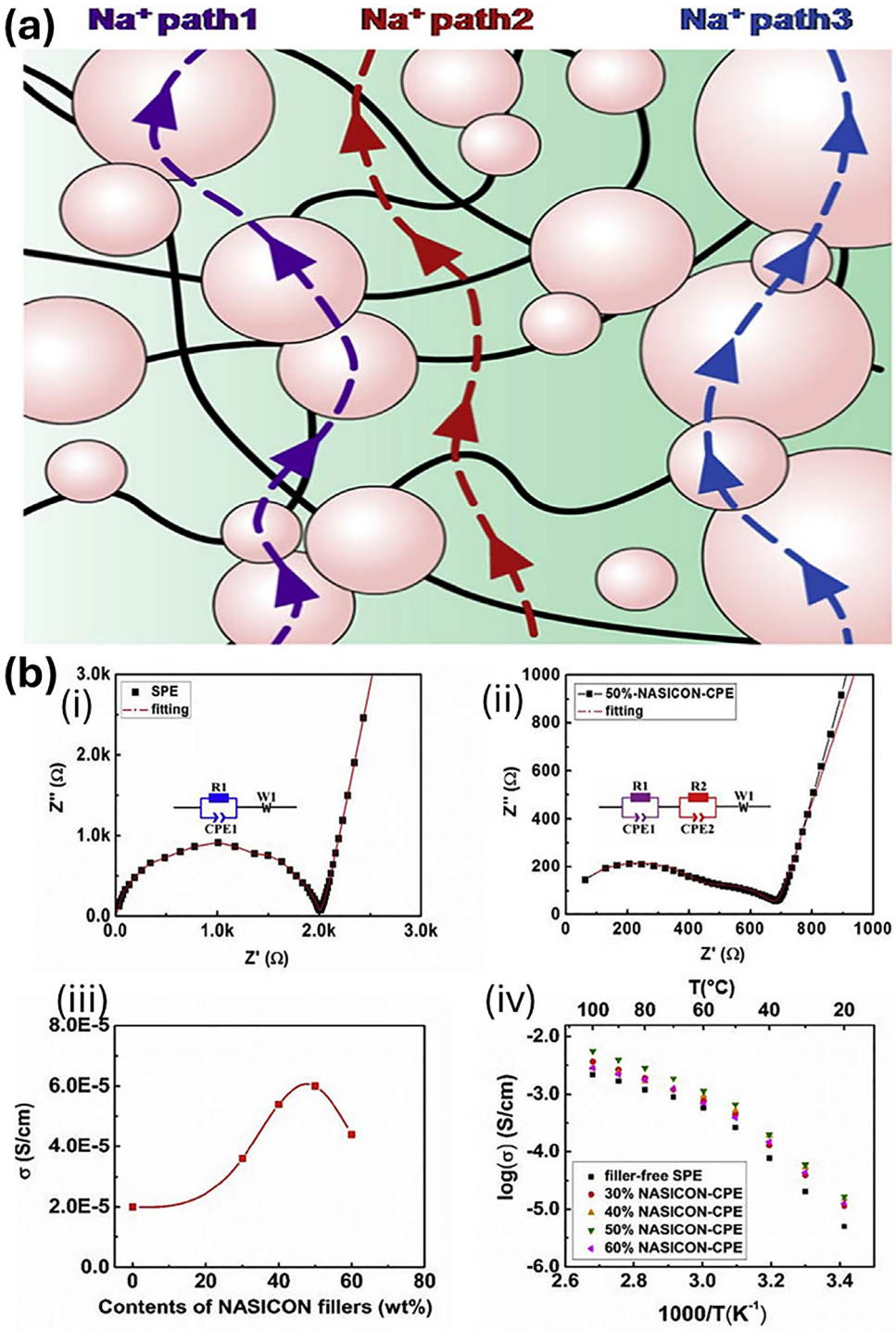

Fig. 18 (a) Illustration showing the Na^+ conduction mechanism in CPEs. (b) Impedance spectra of (i) NaTFSI-PEO14 SPE and (ii) 50 wt% NASICON-CPE at 25 °C, with fitting equivalent circuits; (iii) composition-dependent ionic conductivity of NASICON-CPEs at 30 °C; (iv) temperature-dependent conductivity (20–100 °C) of NASICON-CPEs (reprinted with permission from ref. 199. Copyright © 2017 Elsevier B.V. All rights reserved).

Furthermore, the ESW improved to 4.3 V *vs.* Na^+/Na, attributed to the stabilizing effect of NASICON fillers. With these characteristics, the fabricated all-solid-state sodium ion battery ($Na_3V_2(PO_4)_3$/CPE/Na) exhibited excellent reversible capacity, rate capability, and cycling efficiency, which the authors link to CPE's superior electrochemical stability and its flexibility, which ensures optimal interfacial contact with the electrodes.

Real-world use of CPEs remains hindered by the aggregation and deposition of inorganic ceramic fillers. Insufficient or unevenly distributed fillers prevent seamless Na^+ transport paths and degrade mechanical properties.[208] The inherently

limited Na^+ conductivity of the polymer matrix further limits overall CPE conductivity,[209] particularly, near the percolation threshold, filler agglomeration creates tortuous ion pathways and inhomogeneous current distribution. Combined with a typically limited Na^+ transference number (<0.5), this results in severe Na dendrite growth and concentration polarization.[210,211] Thus, the design of ceramic filler morphology in CPE plays a critical role in creating continuous, long-distance ion-conduction pathways in CPEs. Active fillers benefit particularly from topologies that allow for direct connectivity (nanofibers and 3D frameworks), whereas passive fillers rely mostly on interfacial polarization and polymer structural changes rather than bulk conduction. This distinction emphasizes that interface engineering in active fillers focuses on both polymer–filler and filler–filler interfaces, whereas passive fillers primarily affect the polymer–filler interface. To achieve this, considerable research effort has been directed towards developing CPEs possessing 3D interconnected porous architectures *via* approaches including electrospinning, 3D printing, and template-based methods (*e.g.*, ice-templating and organic removal).[212] Following the same concept, Wang *et al.*[213] created a new CPE, a 3D interconnected NZSP structure having an asymmetric PVDF–HFP/PEO dual-layer (3D-PNZSPP) *via* a simple and sustainable approach using NaCl as a removable template. This design offers key advantages: environmentally friendly NaCl removal in comparison to conventional templates; a 3D-NZSP network enabling seamless Na^+ routes (Fig. 19a), high mechanical resilience, and dendrite suppression. In the developed bilayer design, a thermally/mechanically stable, reduction-resistant PEO/$NaClO_4$ layer protects the Na anode, while an oxidation-resistant PVDF–HFP/$NaClO_4$ layer shields the cathode, collectively enhancing the interfacial compatibility and ESW.

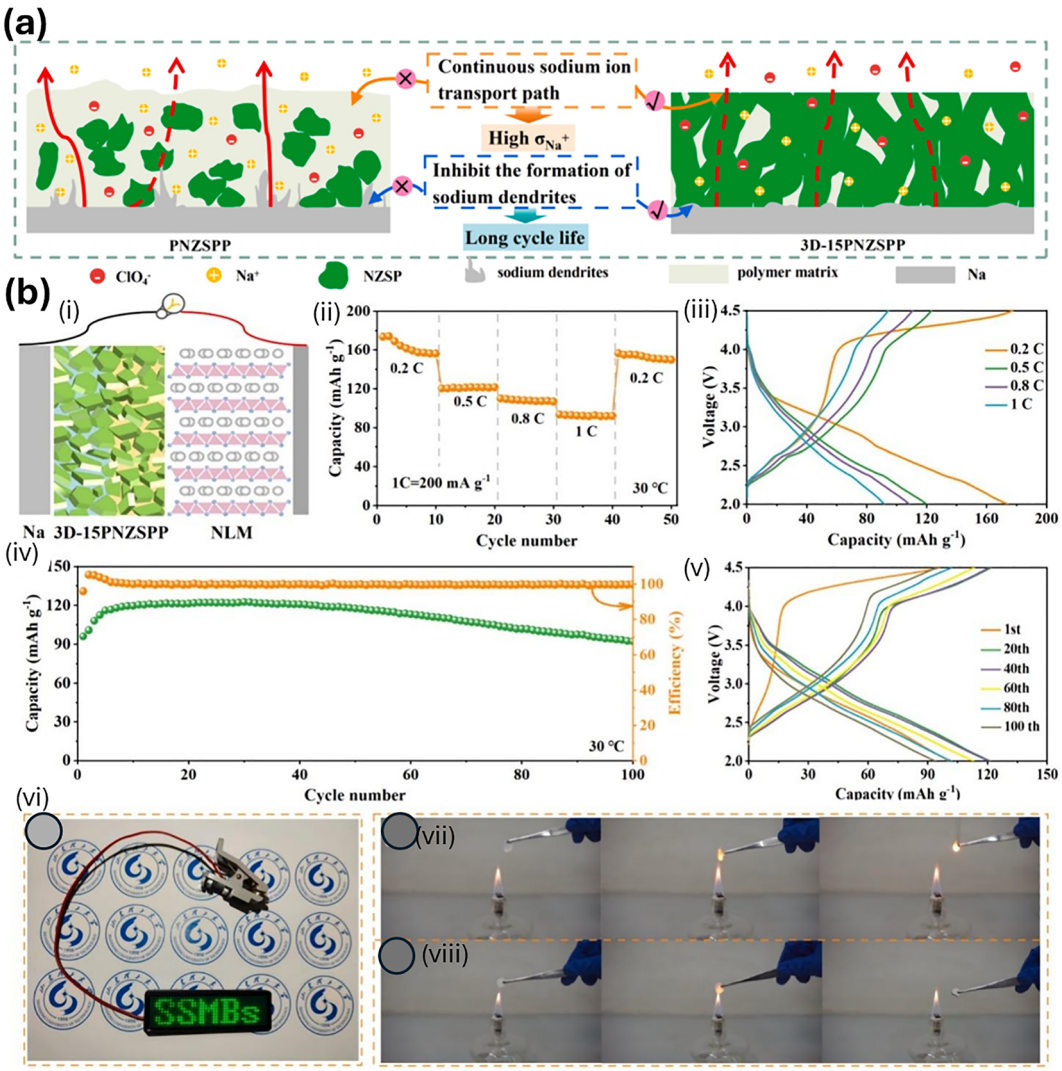

Fig. 19 (a) Schematic depiction of Na^+ ion movement in the PNZSPP (conventional ceramic powder-based CPE) based film, the interface of electrolyte/Na, and 3D-15PNZSPP. (b) All-solid-state NLM/3D-15PNZSPP/Na battery: (i) schematic depiction; (ii) rate efficiency; (iii) GCD profiles at various rates; (iv) cycling stability at 0.5C; (v) GCD profiles at selected cycles; (vi) application efficiency; flammability analysis of (vii) the PNZSPP film and (viii) 3D-15PNZSPP (reprinted with permission from ref. 213. Copyright © 2024 Elsevier B.V. All rights reserved).

The optimized 3D-15PNZSPP CPE achieves an outstanding transference number of 0.82 at 30 °C and a maximum Na^+ ion conductivity of 7.6×10^{-4} S cm^{-1}. This enables Na/Na symmetric cells to cycle stably for more than 700 h, maintaining minimal polarization and stable plating/stripping across current densities. In full solid-state $Na_{0.67}Li_{0.24}Mn_{0.76}O_2$(NLM)/3D-15PNZSPP/Na batteries, the electrolyte delivers a 96.17 mAh g^{-1} discharge capacity at 0.5C at 30 °C with a capacity retention of 96.07% after 100 cycles (Fig. 19b), demonstrating exceptional cycling stability and rate capability for the fabricated batteries.

The conventional solution-casting technique for SPEs/CPEs suffers from solvent evaporation-induced bubbles and residual solvent decomposition at interfaces (increasing impedance/polarization and reducing coulombic efficiency).[214,215] Hot-pressing provides a solvent-free alternative with faster processing and lower cost.[216] This technique eliminates organic solvents and shortens processing time *versus* solution casting. Therefore, Zhao *et al.*[75] used a hot-pressing technique to fabricate a CPE for SIBs that comprises a PEO matrix with a sieved NZSP nanofiller, $NaClO_4$ salt, and trace PEG plasticizer. Particle size control by sieving minimized segregation and agglomeration during mixing and enabled rapid, low-cost CPE production. The resulting CPE exhibited reduced PEO crystallinity and enhanced chain mobility that yielded a maximum ionic conductivity (4.42×10^{-4} S cm^{-1}) and a reasonable ESW (4.5 V *vs.* Na/Na^+). Fig. 20a shows schematic depiction of the ion transport mechanism in (i) conventional SPE *versus* (ii) hot-pressed CPE illustrating how hot-pressing enhances electrolyte performance: it significantly improves mechanical strength to block dendrite penetration (preventing short circuits), while boosting interfacial compatibility for efficient Na^+ transport and stability. The added NZSP/$NaClO_4$ also increases PEO's amorphous phase, accelerating ion conduction. ASSSMBs show a capacity retention of 97.1% following 100 cycles (60 °C, 0.5C) and exhibit excellent coulombic efficiency (~100%).

Apart from SIBs, NZSP has also been investigated as a filler in CPEs. For instance, Ge *et al.*[218] developed a PEO/NaTFSI/NZSP CPE for an all-solid-state sodium battery using a solution casting technique. NaTFSI offers several advantages in comparison to $NaClO_4$ (poses safety risks due to oxidative ClO_4^- decomposition), including improved ionic conductivity, lower toxicity, and thermal stability. The enhanced ionic conductivity is because its $TFSI^-$ anion facilitates dissociation of Na^+ and $TFSI^-$ ions *via* a highly electronegative nitrogen atom and two sulfur atoms, each bonded to a strong electron-absorbing CF_3 group, thereby enhancing ionic conductivity. Additionally, $TFSI^-$'s larger size improves electrolyte transference number.[219] Optimizing the ethylene oxide and Na^+ ion molar ratio to 20 : 1 and incorporating 30 wt% NZSP as a filler yield the optimal ionic conductivity of 3.14×10^{-4} S cm^{-1} at 60 °C, representing a threefold enhancement over the unfilled PEO electrolyte (1.08×10^{-4} S cm^{-1}). This significant improvement was attributed to a dual mechanism: (1) NZSP disrupts PEO crystallinity, as confirmed by XRD, thereby increasing polymer chain segmental mobility and (2) its intrinsic Na^+-ion conductivity that provides additional pathways for Na^+ transport within the composite. Furthermore, the t_{Na^+} for the optimized CPE composition reaches 0.66, which is significantly higher than the value of 0.21 for unfilled SPE at 60 °C. This enhancement stems from NZSP's intrinsic Na^+ conductivity (with the ion mobility number approaching unity), which introduces supplementary Na^+ migration pathways and increases the concentration of mobile sodium ions. Electrochemical performance of the developed CPE was assessed in an all-solid-state Na–S battery setup employing a polyaniline-layered sulfur cathode paired with a sodium metal anode. The battery exhibited prominent initial discharge capacity, extended cycling performance, and better capacity maintenance. To enable high-energy-density batteries, a high-performance solid electrolyte must simultaneously withstand a high-voltage oxidative cathode and mitigate reduction tendencies at the sodium metal anode. To achieve this goal, Wang *et al.*[217] proposed a nanocellulose reinforced hetero-layered CPE design to allow simultaneous interfacial compatibility with the high-potential cathode and Na metallic anode. To stabilize multi-scale interfacial dynamics, a PEO polymer layer in contact with the Na metal anode is layered with a PAN coating oriented toward the high-voltage cathode. NZSP nanofillers (high-energy ball milling was used to reduce the heat-treated NZSP ceramics to the nanoscale, facilitating uniform nanofiller dispersion within the polymer) were incorporated into the polymer matrix, providing additional Na^+ conduction pathways while enhancing PEO chain segmental motion as depicted in Fig. 20b. The hetero-layered CPE simultaneously stabilizes interfaces with a high-voltage cathode (up to 4.2 V) and sodium metal anode. NZSP nanofillers and a mechanically stiff nanocellulose framework enabled the thin-layer (25 μm), ultralightweight (1.65 mg cm^{-2}) CPE fabrication with significant enhancements in ionic conductivity (1.62×10^{-4} S cm^{-1}) and mechanical strength (13.84 MPa) *versus* pristine polymer electrolyte, plus dimensional stability up to 180 °C. Furthermore, the developed CPE paired with an iron hexacyanoferrate cathode and a Na foil anode exhibited excellent cycling stability (93.73% capacity retention over 200 cycles) at ambient-temperature and high-temperature operation reaching 80 °C in ASSMBs.

Kannadasan *et al.*[220] synthesized NZSP by using a sol–gel method and dispersed it in a PEO matrix. They used sodium perborate ($Na_2H_4B_2O_8$) as a source of Na^+ ions. Sodium perborate is a non-toxic, non-carcinogenic, and biodegradable salt, offering enhanced safety over other oxidizing agents and exhibiting better performance compared to conventional electrolytes.[221] Furthermore, the extended shelf life and ease of storage/use make sodium perborate particularly suitable for ASSSB applications. A Stokes' solution casting technique was employed to prepare polymer-integrated solid electrolytes. EIS was performed on SS|CPE|SS cells to measure Na^+ ion conductivities of both pure PEO and CPEs with varying NZSP filler content across 20–80 °C. The CPE achieved a maximum ionic conductivity (2.4×10^{-4} S cm^{-1}) with 25 wt% NZSP loading, beyond which conductivity decreased. Conductivity showed significant improvement between 30 and 60 °C but plateaued

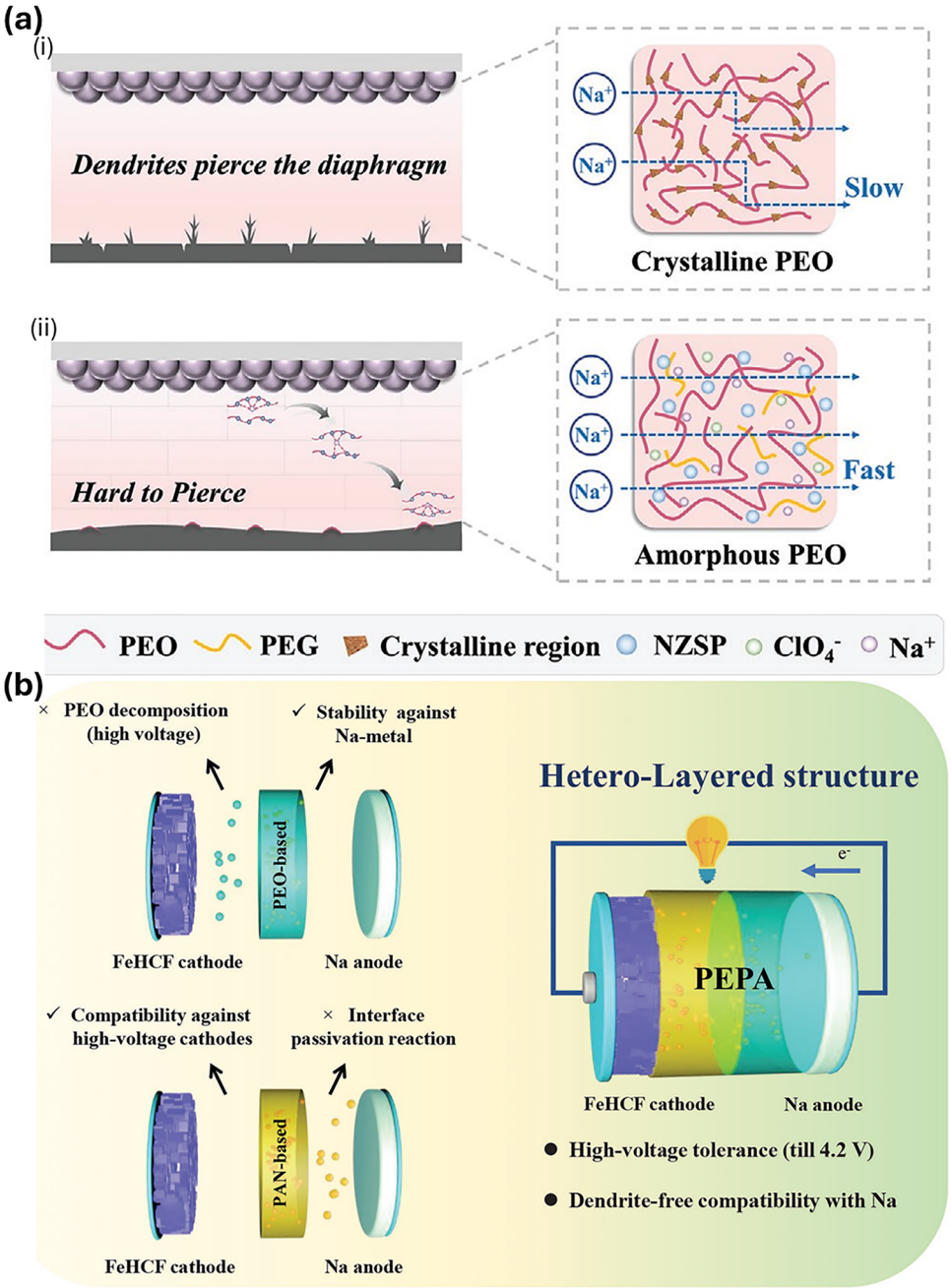

Fig. 20 (a) Schematic depiction of ion transport and mechanism in (i) conventional SPE *versus* (ii) hot-pressed CPE (reprinted with permission from ref. 75. Copyright © 2024 Wiley-VCH GmbH). (b) Schematic of the hetero-layered CPE design (reprinted with permission from ref. 217. Copyright © 2023 Wiley-VCH GmbH).

at higher temperatures (60–75 °C). This enhancement was attributed to the NZSP's ability to reduce PEO crystallinity, thereby facilitating Na^+ ion transport in addition to its intrinsic Na^+ ion conductivity. LSV analysis revealed ESW limits of 3.7 V for PEO, 4.6 V for PEO/$Na_2H_4B_2O_8$/NZSP, and 4.1 V for PEO/$Na_2H_4B_2O_8$. The NZSP filler enhanced stability by 0.5 V compared to the unfilled polymer electrolyte, demonstrating its effectiveness in suppressing PEO degradation (Fig. 21a–c). This study further quantifies the relationship between conductivity and geometry: nanofiber NASICON fillers achieve similar or higher conductivities (3.3×10^{-2} S cm^{-1}),[222] at lower effective volume fractions due to more efficient percolation resulting from their high-aspect-ratio morphology, while particulate NZSP requires ~25–30 wt% to reach its optimal conductivity. The distinction also highlights the different interface engineering approaches needed: nanofiber and 3D frameworks gain from filler–filler interconnections that establish continuous conduction highways, whereas active particle fillers primarily rely on polymer–filler interfacial resistance minimization.

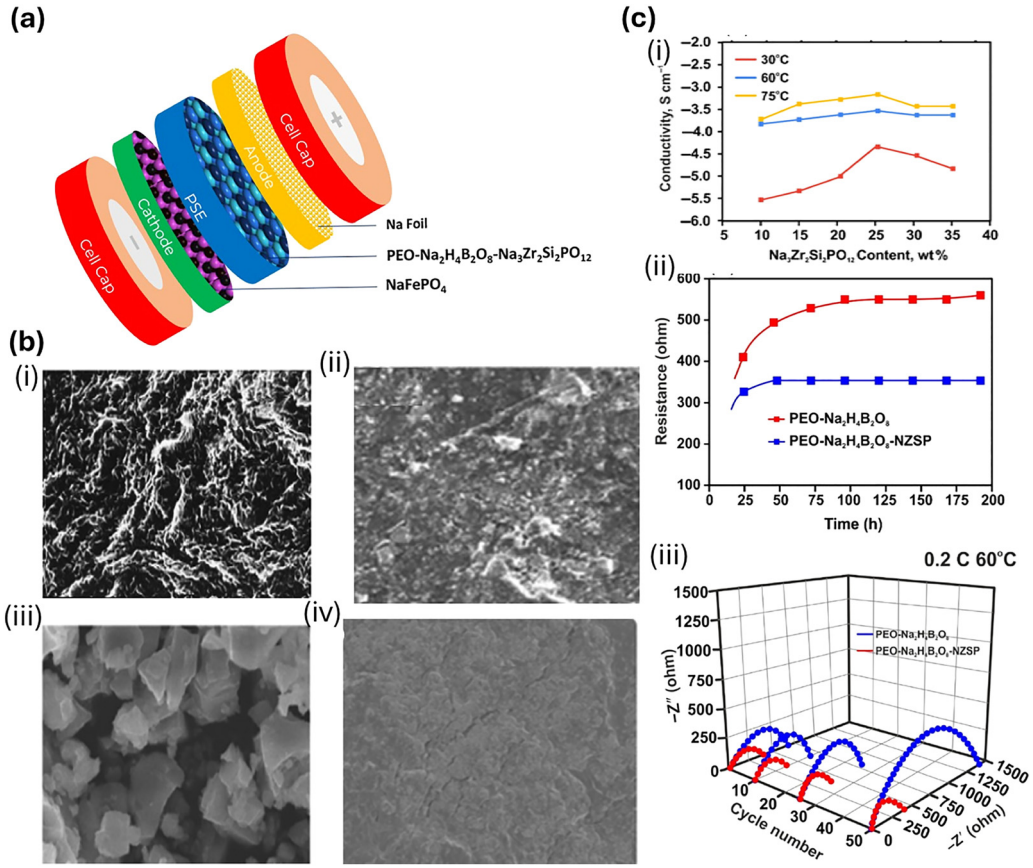

Fig. 21 (a) PEO–$Na_2H_4B_2O_8$–$Na_3Zr_2Si_2PO_{12}$‖$NaFePO_4$ button cell assembly. (b) SEM micrographs of (i) pure PEO, (ii) PEO-$Na_2H_4B_2O_8$, (iii) $Na_3Zr_2Si_2PO_{12}$, and (iv) PEO–$Na_2H_4B_2O_8$–$Na_3Zr_2Si_2PO_{12}$ polymer-integrated solid electrolyte. (c) (i) Ionic conductivities of a solid electrolyte containing PEO–$Na_2H_4B_2O_8$–$Na_3Zr_2Si_2PO_{12}$‖$NaFePO_4$ polymer at varying temperatures and with varied concentrations of $Na_3Zr_2Si_2PO_{12}$. (ii) Changes in the impedance of the Na‖electrolyte‖$NaFePO_4$ cell at various time intervals, and (iii) Nyquist plots across cycles (reprinted with permission from ref. 220. Copyright © 2024 Wiley-VCH).

A comparative analysis of the performance metrics across different NASICON morphologies reveals a clear scaling relationship with filler geometry and connectivity. Conventional powder fillers, such as NZSP in a PEO/NaTFSI matrix, typically achieve optimized room-temperature conductivities on the order of 10^{-5} to 10^{-4} S cm^{-1}, with the transference number (t_{Na^+}) around 0.66 at elevated temperatures (*e.g.*, 60 °C).[218] When the same chemistry is engineered into high-aspect-ratio morphologies, performance is markedly enhanced. For instance, long NLZSP nanofibers (>3 μm) within a PVDF–HFP matrix demonstrate one of the highest reported room-temperature conductivities for an active-filler CPE at 3.36×10^{-4} S cm^{-1}, coupled with a low activation energy of 0.28 eV and a t_{Na^+} of 0.65.[203] This superior performance stems from the fibers' ability to form a continuous percolating network at a lower volumetric threshold, creating efficient long-range ion highways. This trend is further amplified in 3D-interconnected scaffolds, such as the 3D-NZSP structure, which achieves an exceptional t_{Na^+} of 0.82 and a conductivity of 7.6×10^{-4} S cm^{-1} at 30 °C.[213] The data consistently show that transitioning from isolated particles to elongated fibers and finally to pre-connected 3D networks systematically lowers activation barriers, enhances absolute conductivity, and increases the cationic transference number. This progression underscores that for active fillers, optimizing morphological connectivity is as critical as tuning chemical composition to maximize ion transport efficiency. As summarized in Table 3, the performance of NASICON-type fillers in CPEs depends strongly on their morphology and connectivity. Conventional powder fillers mainly enhance ion transport through polymer–filler interfacial effects, whereas high-aspect-ratio nanofibers form continuous percolating networks that improve Na^+ mobility, reduce activation energy, and increase transference numbers. The 3D-interconnected scaffolds further amplify ion transport by providing seamless long-range pathways. These results highlight that, as shown in Table 3, optimizing filler geometry and network connectivity is as important as chemical composition for maximizing electrochemical performance.

7.2. Other complex oxide-type fillers

Beyond NASICON-type ceramics, other types of nanostructured Na-ion conductive inorganic fillers are also emerging as promising alternatives as fillers for CPEs. The $Na_2Zn_2TeO_6$ (NZTO) structure features a substantial 2-D grid Na^+ transport route

Table 3 Effect of NASICON-type filler morphology on ionic conductivity, activation energy, and the Na^+ transference number in CPEs

Filler type/morphology	Ionic conductivity (S cm^{-1})	Activation energy (eV)	Na transference no. (t_{Na^+})	Ref.
Conventional NZSP powder (PEO/NaTFSI matrix)	1×10^{-5}–1×10^{-4} (RT)	Not reported	0.66 (at 60 °C)	218
Short NLZSP nanofibers (S-NFs, ~1 μm)	Not explicitly reported	Not reported	Not explicitly reported	203
Long NLZSP nanofibers (L-NFs, >3 μm)	3.36×10^{-4} (RT)	0.28	0.65	203
3D-interconnected NZSP scaffold (3D-PNZSPP)	7.6×10^{-4} (30 °C)	Not reported	0.82	213

between adjoining honeycomb-like layers, enabling excellent ionic conductivity. Element incorporation (Ga, Ca, Mg, and Ni) in the NZTO structure could further enhance ionic conductivity.[223] Furthermore, to achieve a highly conductive and impurity-free NZTO, the calcination temperature is close to ~850 °C, representing substantially lower energy input than NZSP production.[224] Using the above concept, Wu *et al.*[200] reported CPEs with Ga doped NZTO incorporated as an active filler in PEO/NaTFSI-based SPE. The fabricated CPE was paired with a nanostructured $Na_2V_3(PO_4)_3$ cathode in ASSSBs. The ionic conductivity of CPE with 50 wt% filler content increased ~40 times to 4×10^{-5} S cm^{-1} at 30 °C and 1×10^{-3} S cm^{-1} at 80 °C. This was attributed to the reduced crystallinity of PEO and maximum Na^+ conduction of Ga-NZTO. Ga-doped NZTO's rapid Na^+ routes and strong polymer–filler contacts reduce crystallinity and allow for continuous ion-transport networks, leading to a significant increase in conductivity. The conductivity of the CPE containing 50 wt% doped-NZTO is similar to that of PEO/NZSP CPEs, yet clearly greater than those of the PEO/Al_2O_3, PEO/SiO_2, or PEO/ZrO_2 and other CPEs.[131,207] The developed CPE offers decent thermal stability (no weight reduction up to 140 °C in TGA analysis), an appropriate ESW (~4 V, a symmetric cell with a Na electrode and PEO/NZTO CPE), low Na/CPE interfacial resistance (47 Ω cm^2 at 80 °C), and good stability against the metallic Na electrode. Using the nanostructured $Na_2V_3(PO_4)_3$ cathode and CPE, the ASSSB exhibited superior performance (discharge capacities of ~106 in the 1st and 99 mAh g^{-1} in the 100th cycles, at 0.2C and 80 °C) compared to those of batteries employing the microcrystalline $Na_2V_3(PO_4)_3$ and PEO:NaTFSI electrolyte. The synergy between the highly conductive CPE and the nanostructured cathode allows for faster Na-ion transport and more efficient intercalation, explaining the increased capacity and stability.

In a similar study, Maurya *et al.*[225] reported the development of a Ca-doped NZTO ($Na_2Zn_{1.97}Ca_{0.03}TeO_6$ (NZCTO)) nanofiller-reinforced PVDF–HFP-containing electrospun hybrid polymer membrane (ESHPM) serving as both a separator and an electrolyte for a Na^+ ion capacitor. The physicochemical characteristics of ESHPMs and NZCTO were analyzed for porosity, morphology, electrolyte uptake, thermal stability, crystallinity, operating potential window, ionic conductivity, and dimensional stability. The ionic conductivity of ESHPME incorporating 1 M sodium hexafluorophosphate ($NaPF_6$) in dimethyl carbonate/ethylene carbonate (DMC/EC, 1 : 1 v/v) was assessed by EIS. As for ESPME (with no filler incorporated) and ESHPME (5, 10, and 15 wt% NZCTO) sandwiched within stainless-steel blocking electrodes, substantially higher ionic conductivity was observed in ESHPMEs *versus* ESPME. ESHPME (10 wt% NZCTO) exhibits peak conductivity (up to 1.47×10^{-3} S cm^{-1}), attributed to: (1) PVDF–HFP's C–F moieties lowering surface energy to enhance wettability and ion transport; (2) uniformly dispersed NZCTO fillers promoting Na^+ migration *via* surface charge and intrinsic high conductivity; (3) NZCTO-induced free volume resulting from reduced melting temperature and Lewis acid–base interactions, accelerating polymer segmental motion;[226,227] and (4) hierarchical nanofibrous structures increasing porosity/membrane gelation for enhanced ion transport.[228] However, ESHPME (>10 wt% NZCTO) shows conductivity decay, likely due to filler agglomeration beyond the percolation threshold that results in reducing membrane porosity, electrolyte uptake, and restricting polymer chain dynamics.

Sodium aluminate ($NaAlO_2$) is another active filler for Na-ion conduction that is gaining interest for application in SIBs. As an example, in addition to an enhancement in ESW and ionic conductivity, Hashmi *et al.*[229] found a significant enhancement in t_{Na^+} from 0.27 to 0.42, when $NaAlO_2$ was added as a filler in a gel polymer electrolyte system, as compared to passive Al_2O_3 fillers. In another report, $NaAlO_2$ as a nanofiller was found to enhance the electrochemical characteristics of PVDF–HFP-containing porous gel polymer electrolyte.[230]

Similarly, Chauhan *et al.*[231] explored the influence of $NaAlO_2$ as an active filler on the conductivity of an SPE comprising PEO, propylene carbonate, and $NaClO_4$. A free-standing bendable solid electrolyte membrane prepared by a solution casting method shows enhanced amorphicity (*via* SEM/XRD) upon $NaAlO_2$ dispersion in PEO/$NaClO_4$ SPE. Ionic conductivity increased from 1.6×10^{-5} S cm^{-1} (SPE, 25 °C) to 7.4×10^{-5} S cm^{-1} (5 wt% $NaAlO_2$, 30 °C). A further increase in filler concentration results in a decline in ionic conductivity. The initial conductivity enhancement correlates with enhanced electrolyte amorphicity that facilitates faster ion transport through a disordered polymer matrix. The increase in amorphicity upon the dispersion of $NaAlO_2$ is also evident with the temperature-dependent conductivity, which exhibits Vogel–Tammann–Fulcher behavior across the entire temperature range. Additionally, polar $NaAlO_2$ fillers (Na^+–AlO_2^-) liberate additional Na^+ ions and provide low-resistance transport pathways.[229,230] Beyond 5 wt%, a decline in conductivity was assigned to filler aggregation that blocks Na^+ migration, reducing ion mobility. The optimized CPE composition revealed a significantly enhanced electrochemical stability window (~4.5 V) and t_{Na^+} (~0.60). Sodium β″-alumina (SBA) is another well-established Na^+ ion solid electrolyte, known for its electrochemical stability, maximum ionic conductivity, and better compatibility with sodium metal, which allows its

commercial use in Na–$NiCl_2$ and Na–S batteries.[232] However, its application is constrained by an energy-intensive synthesis process requiring high-temperature sintering and stabilizing additives, along with a high sensitivity to humidity.[233,234] Nevertheless, the integration of SBA into CPEs for SIBs has been explored by various groups. For instance, Fang *et al.*[235] developed an ultra-thin single-particle-layer (UTSPL) CPE membrane, where a ceramic sodium β-alumina (SBA) electrolyte particle (size ~20 mm) bridges across a flexible polymer matrix to form a membrane only ≈20 μm thick. This CPE design, with the optimized composition (35 wt% SBA), synergistically combines the flexibility and mechanical strength of a polymer with a percolating pathway for rapid Na^+ transport (Fig. 22a). Fig. 22b depicts comparative illustration of Na^+ ion conduction pathways with the bridged single-particle-layer providing continuous percolation networks for Na^+ ion conduction, unlike the isolated particles in the conventional CPE. This design also solves the problem of isolated inorganic particles within typical CPEs, which generally fail to form a continuous percolation network for efficient Na^+ transport, where the overall conductivity remains restricted by the poor inherent ion conduction of the polymer matrix.

This architecture with optimized composition (35 wt% filler content) delivered exceptional performance in terms of a very high room temperature ionic conductivity (0.19 mS cm^{-1}) and Na^+ transference number (0.92). The high transference number indicates that the bridged SBA layer effectively traps anions, thereby releasing more Na^+ ions for transport, while its percolation network facilitates rapid cation conduction. This resulted in a significant reduction in concentration overpotential, enhanced rate capability, and improved electrolyte's ability to suppress sodium dendrite growth, as evidenced by good plating/stripping behavior with a sodium metal anode.

7.3. Mechanistic insights into filler function in composite electrolytes

The diverse array of fillers discussed, ranging from passive oxides and high-κ dielectrics to active ceramics and framework materials, enhance CPE performance through distinct yet often synergistic mechanisms. A unified understanding emerges by categorizing fillers based on their primary function and linking their intrinsic properties to the resulting electrochemical performance.

Fillers can be classified into three principal mechanistic groups:

1. Structural disruptors (crystallinity modifiers): inert, non-conductive fillers such as SiO_2, Al_2O_3, and TiO_2 primarily act as solid-state plasticizers. Their incorporation physically disrupts the ordered packing of polymer chains (*e.g.*, PEO and PVDF–HFP), increasing the amorphous phase content. This expansion of the disordered regions facilitates greater segmental motion of polymer chains, which is the primary driver of cation mobility in solvent-free polymer electrolytes. The enhancement in ionic conductivity in these systems correlates directly with the degree of crystallinity suppression, as consistently confirmed by XRD and DSC analyses.

2. Interfacial modifiers *via* Lewis acid–base interactions: this group includes fillers whose surface chemistry actively modifies local ion coordination and transport. Materials such as hydroxyapatite (HAP), boron-based COFs (B-COF), and high-dielectric-constant particles (*e.g.*, $SrTiO_3$ and $BaTiO_3$) function as interfacial modifiers. Their surfaces provide Lewis acid or base sites that interact with electrolyte anions (*e.g.*, $TFSI^-$ and PF_6^-). For HAP and B-COF, this results in anion adsorption or trapping, which promotes salt dissociation and increases the cationic transference number (t_{Na^+}). For high-κ fillers, the

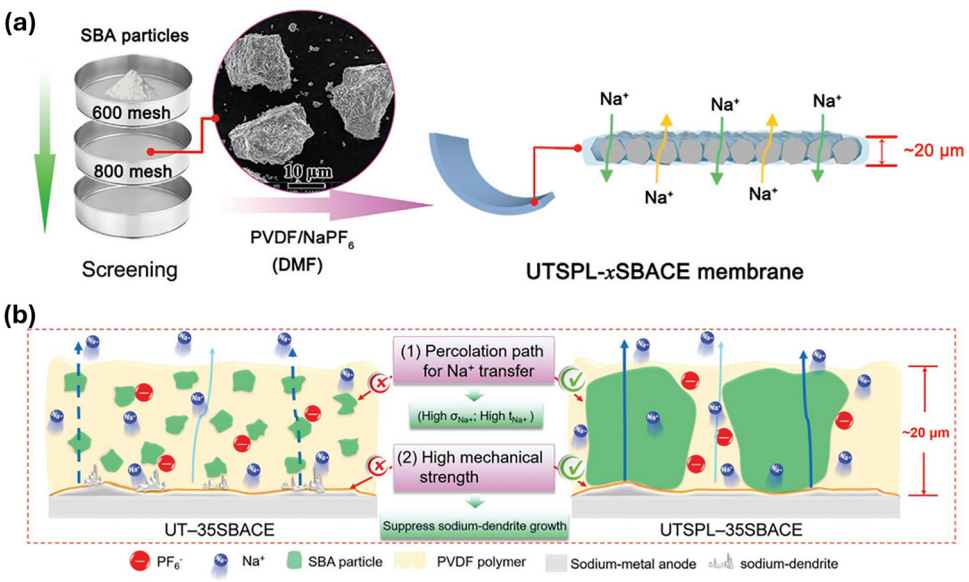

Fig. 22 (a) Schematic of the synthesis protocol for the SBA CPE. (b) Comparative illustration of Na^+ ion conduction pathways: the bridged single-particle-layer providing continuous percolation networks for Na^+ ion conduction, unlike the isolated particles in the conventional CPE membrane, including the electrolyte/anode interface behavior (reprinted with permission from ref. 235. Copyright © 2022 Wiley-VCH GmbH).

strong dielectric polarization weakens the coulombic attraction between Na^+ and its counter-anion, likewise enhancing dissociation and increasing the concentration of free charge carriers.

3. Active ionic conductors: fillers with intrinsic sodium-ion conductivity, such as NASICON-type ceramics (NZSP), $Na_2Zn_2TeO_6$ (NZTO), and $NaAlO_2$, serve a dual purpose. First, like passive fillers, they can disrupt polymer crystallinity at their interfaces. Second, and more critically, their bulk provides fast ion-conduction pathways, contributing directly to overall conductivity. These fillers act as a source of additional mobile Na^+ ions and can form percolating networks within the polymer matrix, creating highway-like channels for ion transport that bypass the slower polymer-mediated diffusion.

A critical and universal observation across all filler types is the existence of an optimum loading content (*e.g.*, ~8 wt% for TiO_2 and ~30 wt% for NZSP), beyond which ionic conductivity declines. This optimum represents a balance between competing effects. At lower loadings, benefits dominate interfacial area increases, promoting dissociation and amorphization, and percolation pathways begin to form for conductive fillers. Beyond the threshold, detrimental effects prevail; nanoparticle aggregation severely impedes ion transport by blocking ion pathways and restricting polymer chain dynamics, and for conductive fillers, a dense packing may reduce the effective conductive interface with the polymer. The performance of a filler is ultimately governed by a combination of three key properties:

1. Surface area and morphology: high-surface-area fillers (nanoparticles, nanofibers, and 2D sheets) maximize the polymer–filler interface. High-aspect-ratio morphologies (nanofibers and 3D scaffolds) dramatically lower the percolation threshold, enabling the formation of continuous conductive networks at low volume fractions, as demonstrated by NASICON nanofibers.

2. Dielectric constant (κ): a high κ is a primary property for fillers aimed at enhancing salt dissociation. The local electric field of a high-κ particle screens the ion-pair interaction, an effect quantitatively described by the reduction of the activation energy for dissociation.

3. Surface chemistry: the chemical functionalities (*e.g.*, –OH groups on HAP, Zr Lewis acid sites in MOFs, and $–NH_2$ groups on g-C_3N_4) dictate the specific nature of the polymer–filler and ion–filler interaction. This chemistry determines whether the filler acts as an anion trapper, a dissociation promoter, or simply a physical crosslinker.

7.4. Key performance metrics of high-performing CPE systems

To distill the practical insights from the above broad survey, this section identifies the most promising systems, elucidates the mechanisms behind their superior performance, and comments on their potential for scalable manufacturing. Based on the comprehensive review, the highest-performing CPEs are distinguished by their ability to combine high ionic conductivity with a high Na^+ transference number, t_{Na^+}, which minimizes polarization and enables long-term stability against sodium metal. The high-performing CPE designs integrate multiple enhancement mechanisms: 3D-interconnected or high-aspect-ratio active fillers (*e.g.*, NASICON nanofibers) create percolating ion highways, while anion-trapping frameworks (*e.g.*, B-COF and functionalized nanofibers) actively immobilize anions to boost t_{Na^+}. The key metrics of these high-performing systems are consolidated in Table 4 below for direct comparison.

Despite their outstanding metrics, the path to industrial adoption for these advanced CPEs is constrained by significant manufacturing challenges. The fabrication of tailored electrospun nanofibers and 3D-templated scaffolds is complex and has low-throughput, while the synthesis of tailored frameworks (B-COF and MOFs) involves costly multi-step processes and precise structural control. Consequently, translating these laboratory benchmarks to the commercial scale hinges on two key developments: the simplification of core material syntheses and their adaptation to scalable, continuous production platforms like roll-to-roll manufacturing.

8. Electrode/electrolyte interfacial engineering

According to the Electrochemical Dictionary (by Allen Bard *et al.*[236]), ''Interphase or interfacial region is an interfacial region between two contacting bulk phases, physically and chemically distinct from both bulk phases.'' It is a thin 3D transition zone where material properties gradually shift from one bulk phase to the other. The two-dimensional boundary that separates two distinct phases is termed the interface. The most prominent example of an interphase in the literature is the SEI reported by Birkl *et al.*[237] (Fig. 23a). This is a passivating layer (insulating electrons) that forms on negative electrodes during initial battery cycling because of the reduction and degradation of organic liquid electrolyte, commonly 1 M $LiPF_6$ in organic carbonates. For graphite as an anode, as an example,

Table 4 Key performance metrics of high-performance CPEs

System (filler/matrix)	Optimal ionic conductivity (temperature)	Na^+ transference number (t_{Na^+})	Ref.
3D-NZSP scaffold (PVDF–HFP/PEO)	7.6×10^{-4} S cm^{-1} (30 °C)	0.82	213
B-COF framework (PEO)	5.28×10^{-4} S cm^{-1} (60 °C)	0.71	181
Functionalized SiO_2 nanofibers (PAAEM)	0.75×10^{-4} S cm^{-1} (−40 °C)	0.72	177
NASICON nanofibers (PVDF–HFP)	3.36×10^{-4} S cm^{-1} (RT)	0.65	203
Bridged β-alumina (polymer composite)	1.9×10^{-4} S cm^{-1} (RT)	0.92	235
$NaAlO_2$ active filler (PEO/PC)	7.4×10^{-5} S cm^{-1} (30 °C)	0.60	231

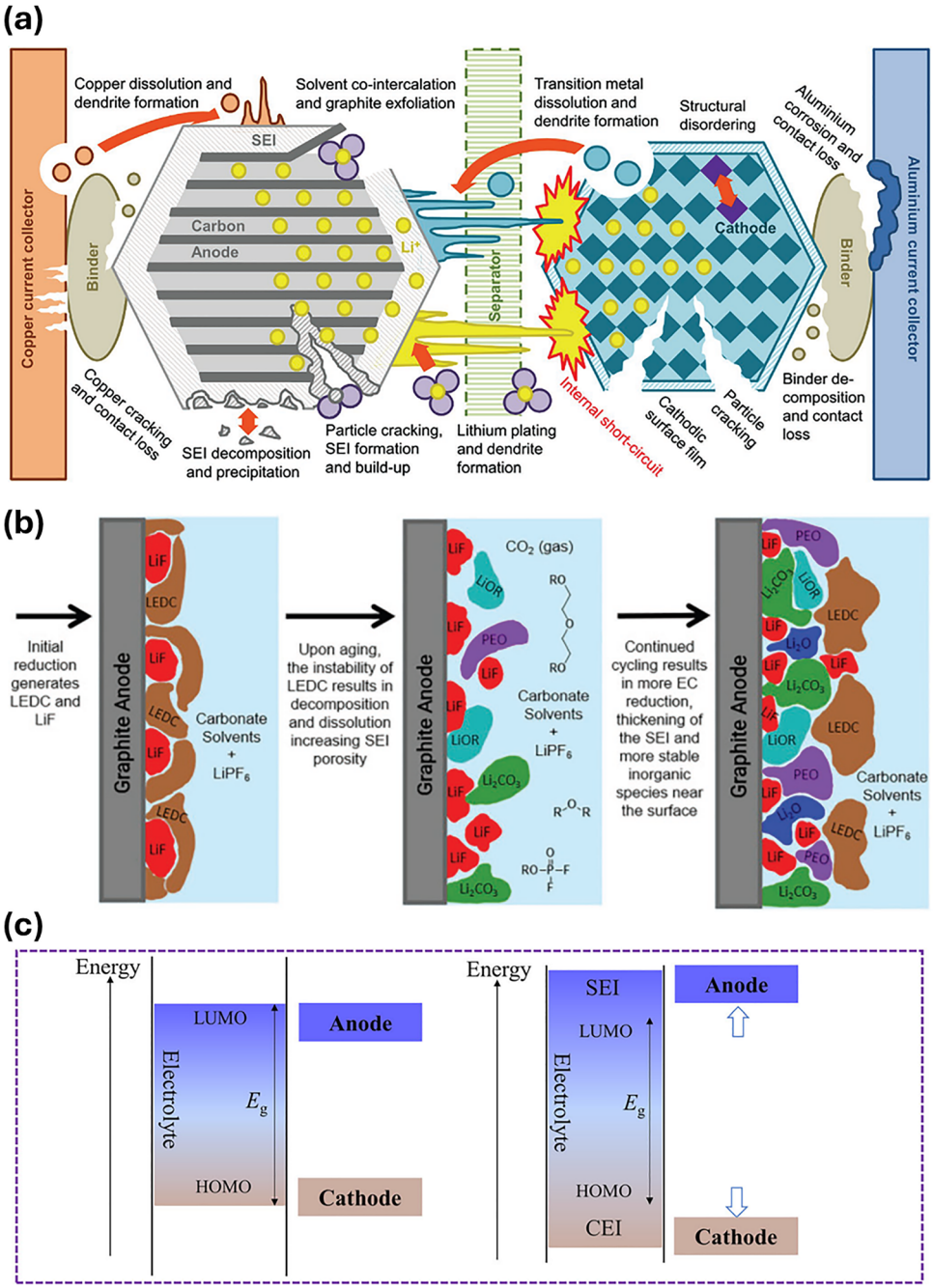

Fig. 23 (a) Schematic illustrating aging mechanisms in traditional LIBs, with focus on interfacial reactions (reprinted from ref. 237 under CC BY 4.0 Copyright 2017, the Authors. Published by Elsevier). (b) Schematic showing initial SEI formation on graphite, SEI structural changes from acid-mediated thermal decomposition, and electrolyte reduction-induced SEI thickening (LEDC: lithium ethylene dicarbonate) (reprinted with permission from ref. 247. Copyright © 2019 Elsevier Inc.). (c) Schematic depiction: CEI and SEI formation mechanisms and their electrochemical roles in SIBs (reprinted from ref. 246, 2024, Wiley-VCH GmbH. Licensed under CC BY-NC 4.0).

this layer typically forms below ~0.8 V *vs.* Li^+/Li.[238] The SEI production is critical for graphite electrodes as it prevents additional electrolyte reduction during cycling while maintaining Li^+ ion transport to the electrode surface. An unstable SEI, however, directly contributes to battery degradation by increasing interfacial resistance, promoting polarization buildup and inducing localized heating.[239,240] Historically, researchers first observed protective solid film formation on a lithium metal anode in the 1960s, which enabled stable battery operation. Peled formally termed this layer the "solid electrolyte interphase" (SEI) in 1979.[241] Later, in 1997, Peled *et al.*[242] proposed the first structural prototype depicting the SEI as a mosaic of inorganic and organic components. In addition to the anode, the interfacial reactions occurring at cathode also generate an

interphase between the cathode and electrolyte, which is named the ''cathode electrolyte interphase (CEI)'', or ''solid permeable interphase (SPI)''. Regarding CEIs, significant development started when, in 2015, Mu *et al.*[243] and Talaie *et al.*[244] conducted research to improve cathode structural reversibility through CEI-focused studies. In 2017, Alvarado *et al.*[245] used atomic layer deposition to investigate the CEI in SIBs, where the CEI formed on electrodes was found to contain reduced carbonate species and increased inorganic content that was found to result in the rapid Na^+ ion kinetics and enhanced coulombic efficiency and decreased cathode impedance. Recent studies continue to develop improved CEIs through:[246] (i) electrolyte composition control (salts, solvents, and additives), (ii) direct cathode surface modification, and (iii) indirect synthesis optimization of cathode materials.

Fundamentally, for LIBs and SIBs, interphase chemistry differs due to differences in charge density and Lewis acidity of Li^+ and Na^+ ions.[248] These differences primarily arise from different solvation/desolvation dynamics for the respective cations, which dictate interphase nucleation and initial cation diffusion activation through the interphase layer. As a result, Na-based interphases often deviate from established Li-based principles.[249] This deviation also means that interfacial engineering tactics that work in LIBs cannot be readily applied to SIBs, making microstructure control even more critical for long-term cycling stability. Since electrolytes chemically govern interphase generation, manipulating their constituents, including solvents, salts, additives, and concentration, directly dictates interphase composition and structure.[250,251] The production of an electrode/electrolyte interphase happens as the battery operates beyond the ESW of the electrolyte. The harsh conditions trigger electrolyte decomposition, which is accompanied by the formation of an interphase on the electrodes, as schematically shown by Heiskanen *et al.*[247] (Fig. 23b). The stable and well-functioning electrode/electrolyte interphase is critical for preserving reversible capacity and enabling long-term stable battery operation.[252] As depicted in Fig. 23c by Han *et al.*,[246] the anode serves as the reductant and the cathode as the oxidant, while the intrinsic stability window is governed by the energy gap (E_g) within the electrolyte's LUMO and HOMO levels. SEI compounds on the anode raise the LUMO energy, while CEI compounds lower the HOMO energy. This synergistic effect widens E_g and enhances long-term operational stability at both electrodes.[253]

A critical challenge in developing high-efficiency SIBs with solid electrolytes is the large interfacial impedance caused by weak bonding within electrolyte and electrode materials. The critical distinction for solid electrolytes contacting electrodes stems from wetting challenges, unlike liquid electrolytes that readily penetrate electrode pores to ensure optimal ionic transport.[254] Solid electrolyte wettability requires intimate contact with electrodes. Consequently, voids/cracks/porosity severely degrade solid-state battery performance by creating ''dead ends'' for the transport of ions and electrons.[255,256] These voids further accelerate dendrite formation and serve as nucleation sites for interfacial decomposition.[257] Thus, key interfacial engineering for solid-state SIBs includes solid electrolyte shaping/design and electrode design to ensure complete component wetting and efficient ion and electron transport pathways. Thus, in SSBs compared to conventional liquid electrolyte-based batteries, several more interface/interphase issues need to be addressed (Fig. 24a and b).[258] Addressing these issues require increasing the mechanical, thermal and electrochemical stability at the electrode/electrolyte interface to facilitate fast ion migration and to prevent sluggish reactions.

In CPEs that incorporate both inorganic fillers and polymer electrolytes, the rigidity of inorganic fillers often results in poor electrode affinity, increasing interfacial resistance. Polymers, on the other hand, offer better interfacial compatibility and assist in the fabrication of stable SEIs. This interface supports efficient sodium-ion transport while effectively preventing electron migration.[260] To address the issue of high interfacial resistivity and interfacial compatibility in CPEs, innovative approaches are required in the design of ASSBs. This involves tailored engineering of electrode/electrolyte interfacial layers to promote facile interactions between components, thereby enhancing the overall battery performance.[261,262] Fig. 25a and b schematically show the interface engineering for SIBs by combining electrolyte engineering and electrode effects.[263,264]

The approach to electrode/electrolyte interfacial engineering diverges significantly depending on whether the CPE incorporates inert or active fillers. For CPEs with inert fillers (*e.g.*, SiO_2 and Al_2O_3), whose ionic conductivity is inherently limited by the polymer matrix, the paramount goal is minimizing interfacial resistance through maximized electrolyte/electrode contact. Strategies, therefore, emphasize enhanced wettability and intimacy, such as *in situ* polymerization within electrode pores to create cohesive, void-free interfaces, as demonstrated in PVC-based and boron-containing CPE systems.[79,265] In contrast, CPEs with active fillers (*e.g.*, NASICON-type NZSP) present a dual challenge: the composite must maintain a rigid, percolating ceramic network for high bulk conductivity, while simultaneously presenting a compliant interface to the electrode. This necessitates decoupled structural engineering. Advanced designs address this by creating asymmetric or gradient architectures, where a ceramic-rich, high-conductivity core is flanked by polymer-rich, compliant surface layers that ensure stable interfacial contact, a principle successfully applied in five-layer gradient composite electrolytes (GCEs).[266] Alternatively, functional coatings (*e.g.*, ferroelectric layers) on the ceramic scaffold can be employed to mitigate space-charge effects and improve adhesion without sacrificing ceramic connectivity, as shown in ferroelectric-engineered 3D-NZSP frameworks.[267] Thus, while inert-filler CPE engineering focuses on perfecting interfacial intimacy through polymer contact, active-filler CPE engineering requires innovative designs to reconcile the opposing demands of a rigid, conductive bulk and a dynamically stable, soft interface with the electrodes. The following sections detail these strategies through specific examples from the literature, illustrating how the fundamental filler type dictates the choice of interfacial engineering approach.

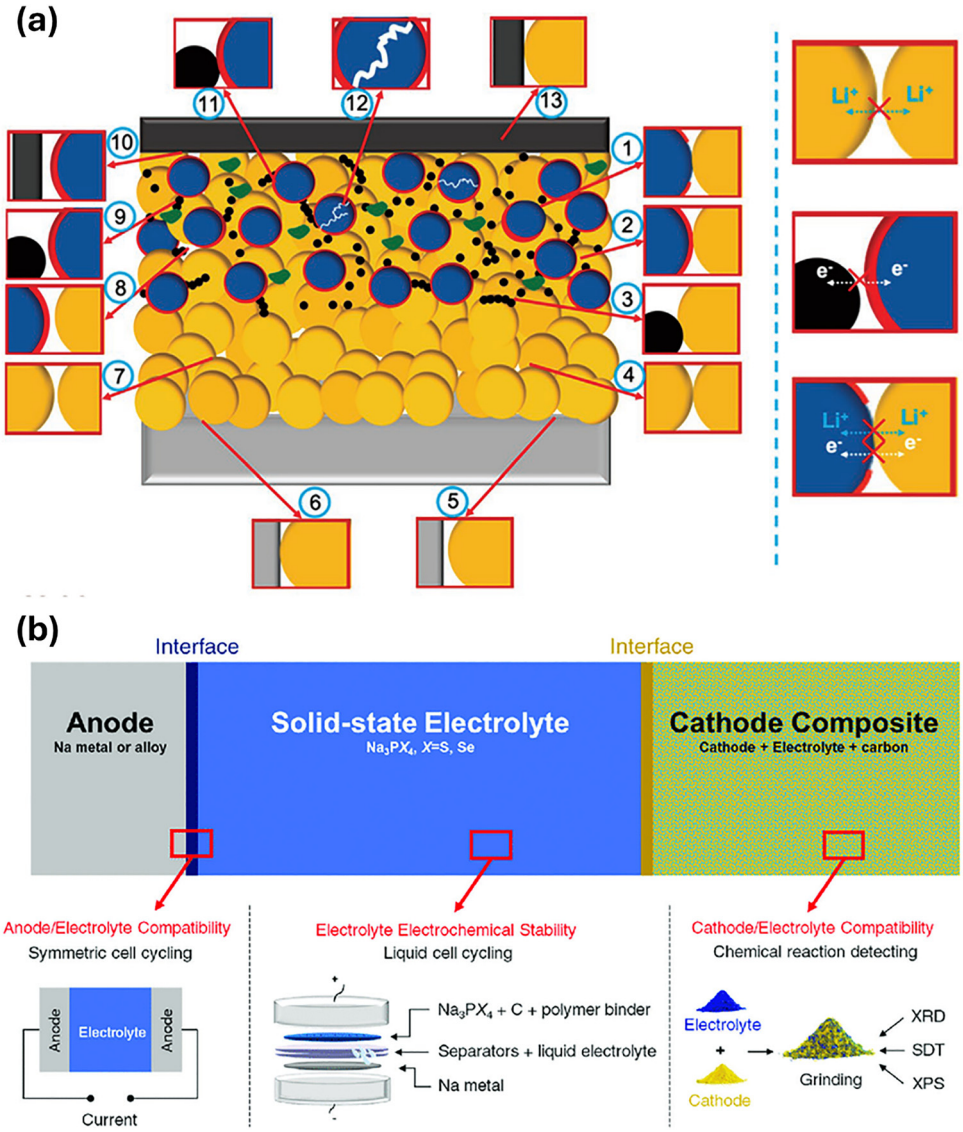

Fig. 24 (a) Schematic depicting interfacial occurrence in sulfide-based ASSBs: (1) unmodified cathode/electrolyte; (2,8) modified cathode/electrolyte (contact/voids); (3,9) conducting additive/electrolyte (contact/voids); (4,7) electrolyte/electrolyte (voids/contact); (5,6) Li metal/electrolyte (voids and contact); (10,13) cathode current collector/coated cathode (voids/contact); (11) coated cathode/conducting additive; (12) cathode fissures (reprinted with permission from ref. 258. Copyright © 2020, American Chemical Society). (b) Schematic depiction of an overview of the stability and compatibility challenges with ASSBs, along with the experimental techniques used to evaluate them (reprinted from ref. 259, 2017. Licensed under CC BY 3.0, The Royal Society of Chemistry).

Symmetric cells with NASICON-type $Na_3V_2(PO_4)_3$ (NVP) electrodes and $NaClO_4$ dissolved in organic carbonates have been found to lose their discharge capacity quite quickly; the capacity decay rate of these cells reaches up to 3.94% per cycle. The sluggish kinetics of the anode and the development of unwanted SEI on the anode are thought to cause this behavior.[268,269] Wang *et al.*[267] resolved this issue by designing a ferroelectric-designed composite electrolyte, created by infiltrating $NaClO_4$/PEO into a 3D-porous ferroelectric-NZSP framework [thin ferroelectric layers of $K_{0.5}Na_{0.5}NbO_3$ were coated on the surface of the NZSP framework without affecting its NASICON crystalline structure], that achieved both high flexibility and excellent ionic conductivity. Compared to non-engineered (no ferroelectric coating) counterparts, this design improved the electrochemical stability window. In addition, it enhanced interfacial ion conduction and reduced electrode/electrolyte interfacial resistance. The authors argued that in non-engineered electrolyte cells, the electrode/electrolyte potential difference induces space-charge accumulation at the interface, elevating the ion migration energy barrier and resulting in high charge-transfer resistance.[270] Conversely, in ferroelectric-engineered CPEs, interfacial potential polarizes ferroelectric domains *via* dipole rotation, generating a counter-electric field that redistributes interfacial ions, suppresses space-charge accumulation, and consequently reduces charge-transfer resistance (Fig. 26a). Thus, the symmetric solid-state

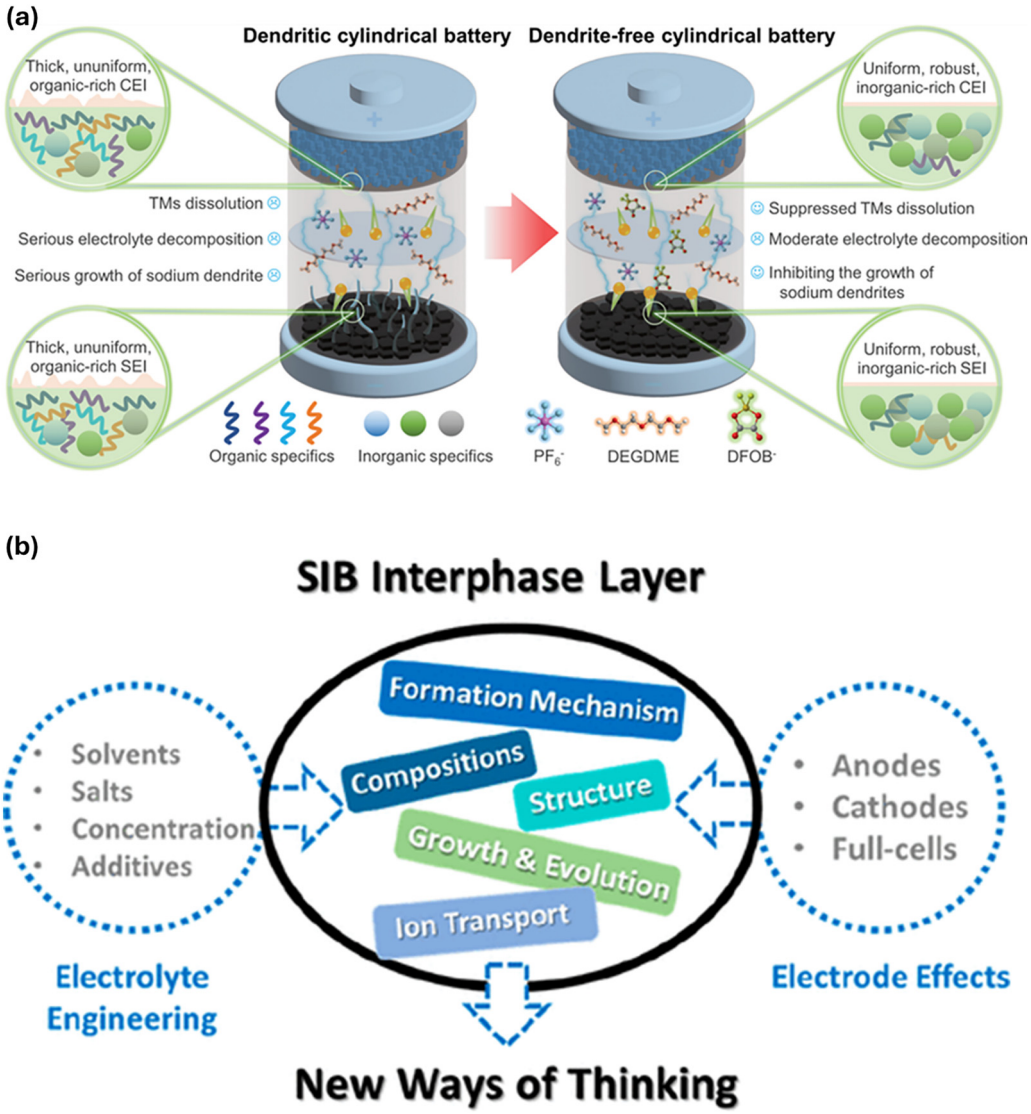

Fig. 25 (a) Schematic illustration of dendrite-free SIB design through electrolyte interface engineering (reprinted with permission from ref. 264, Copyright © 2024 Wiley-VCH GmbH). (b) Schematic representation of fabricating new advanced SIBs through electrode–electrolyte surface engineering (reprinted with permission from ref. 263, Copyright © 2021, American Chemical Society).

SIBs (NVP//NVP) with this electrolyte demonstrated exceptional stability: 86.4% capacity retention after 650 cycles (0.021% fade/cycle); outperforming liquid electrolytes (0.086% fade/cycle) (4× faster degradation) and non-engineered composites (75.8% retention (0.037% fade/cycle)). With a Prussian-blue cathode ($Na_xFe_yFe(CN)_{6-z}\cdot nH_2O$, NFFCN), the all-solid-state NVP//NFFCN cell achieved ultra-stable cycling at 500 mA g^{-1}, retaining 53.3% discharge capacity after 9000 cycles, representing a minimal fade rate of ~0.005% per cycle (Fig. 26b).

Kannadasan *et al.*[271] developed PEO/SPC/NZSP CPEs using sodium percarbonate (SPC) to achieve improved interfacial compatibility, wide electrochemical windows, dendrite growth prevention, and electrode/electrolyte contact and stability. For interfacial stability evaluation, the post-cycling EIS data showed progressively rising interface resistance (672 Ω/10cyc → 789 Ω/20cyc → 824 Ω/35cyc → 1449 Ω/50cyc) for PEO/SPC SPE, while PEO/SPC/NZSP stabilized at ~422 Ω after 25 cycles, confirming superior interfacial compatibility with Na anodes. Furthermore, PEO/SPC resistance rose from 405 Ω to 560 Ω over seven days in Na‖PEO/SPC/NZSP‖$NaFePO_4$ cells (60 °C), whereas PEO/SPC/NZSP stabilized at 364 Ω (initial 310 Ω) with no significant change after 7 days. The better interfacial compatibility and stability of the CPEs were assigned to reduced Na-electrode/PEO contact area due to the inclusion of the NZSP filler that prevents Na^+/PEO interactions.

In situ polymerization is another approach to enhance interfacial behavior, for instance, Chen *et al.*[265] developed flexible and transparent PVC (polyvinylene carbonate)-based CPE films *via in situ* polymerization of VC+TEGDME (vinylene carbonate and tetraethylene glycol dimethyl ether) within a phase-transfer-fabricated PVDF–HFP porous support (with acetone solvent/water non-solvent) (Fig. 27a). In addition to

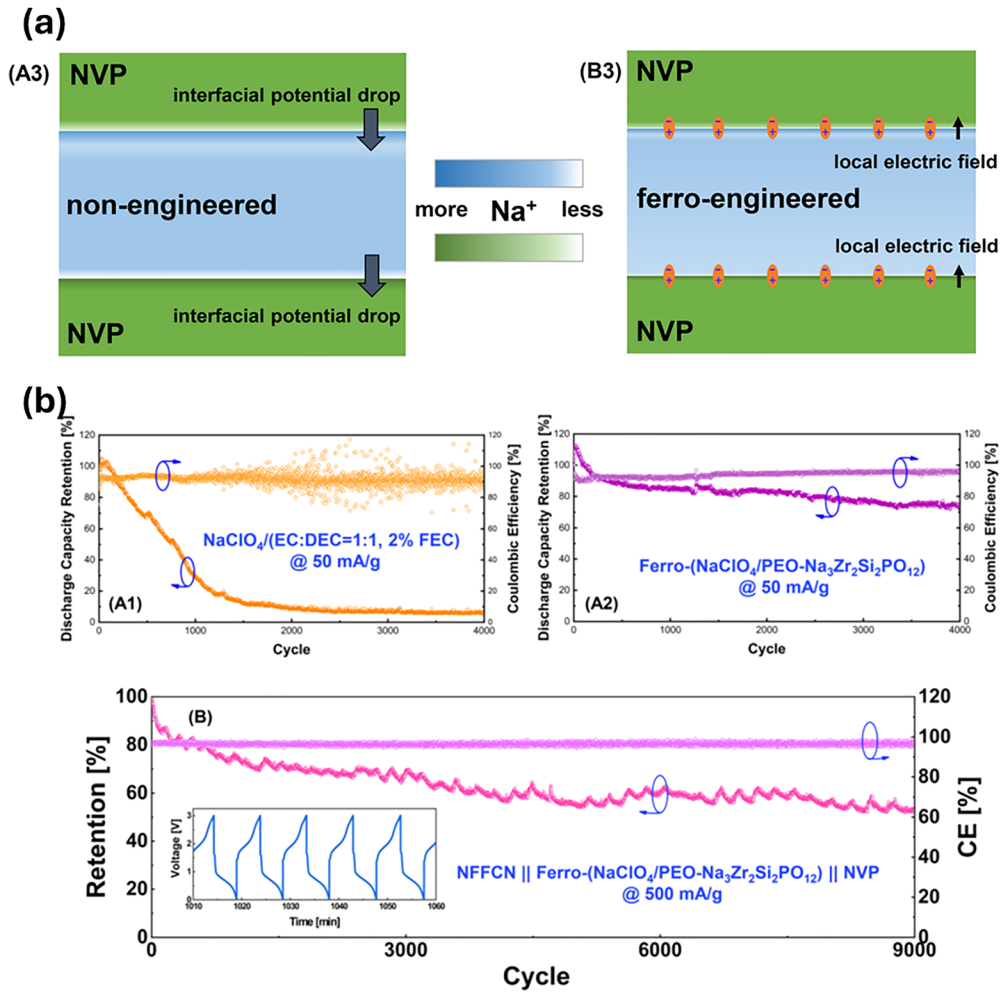

Fig. 26 (a) Schematic depiction of ion distribution at interfaces in NVP//NVP symmetric all-solid-state cells employing non-engineered and ferroelectric-engineered composite electrolytes. (b) NVP//NFFCN asymmetric cells' cycling performance with A2 (all-solid-state ferroelectric-engineered composite) and A1 (commercial liquid) electrolytes at 50 mA g^{-1} (RT); extended cycling of NFFCN‖Ferro-($NaClO_4$/PEO-$Na_3Zr_2Si_2PO_{12}$)‖NVP cells at 500 mA g^{-1} (RT). Inset: 10 min charge/discharge cycles (reprinted from ref. 267. Licensed under CC BY 4.0).

excellent ionic conductivity, ESW, and Na-ion transference number, the developed CPE exhibited enhanced interfacial compatibility (Fig. 27b(i) and (ii)). The electrochemical stability and Na metal compatibility of the CPE were assessed in symmetric Na‖PVC-CPE‖Na cells. Following 400 h polarization at 1 mA cm^{-2}, the cell maintained stable plating/stripping with minimal polarization (Fig. 27b(iii) and (iv)). In contrast, Na‖liquid electrolyte‖Na cells showed continuously increasing overpotential, indicating nonuniform plating/stripping resulting from poor compatibility. The CPE's superior compatibility resulted in suppressing dendrite growth and short circuits. EIS analysis, Fig. 27b(v) and (vi), further confirmed compatibility, *i.e.*, bulk resistance remained stable during aging, while interfacial resistance increased slightly over 15 days and then stabilized, showing good interfacial stability with Na metal.

To overcome poor ion transfer between electrodes and at electrode/electrolyte interfaces, which is a crucial factor for SSB performance, the authors fabricated the c-NFM ($NaNi_{1/3}Fe_{1/3}Mn_{1/3}O_2$) cathode *via in situ* electrolyte growth within the electrode. SEM confirmed c-NFM's smooth, homogeneous surface with polymer-filled pores, enabling omnidirectional Na^+ transport through both point contacts and nano-cracks, analogous to liquid electrolytes. This significantly enhances Na^+ transfer efficiency as compared to conventional NFM cathodes. Beyond electrode design, high interfacial resistance resulting from inadequate electrode/electrolyte contact is still a critical issue for SSBs. Addressing this issue, the authors fabricated the c-NFM/CPE/Na cell *via* single-step *in situ* polymerization, ensuring close electrode/electrolyte contact. For comparison, an *ex situ* assembled cell was fabricated with pre-synthesized CPE electrolyte sandwiched between an *ex situ* NFM cathode and Na anode. Fig. 27b confirms superior interfacial contact in the *in situ* cell that enabled higher stability and lower interfacial resistance.

Capitalizing on the Lewis acidic nature of sp^2-hybridized boron to trap basic anions from sodium salts, facilitating salt dissociation and increasing the Na^+ ion transference number,[181] the same group, Chen *et al.*,[79] developed a novel

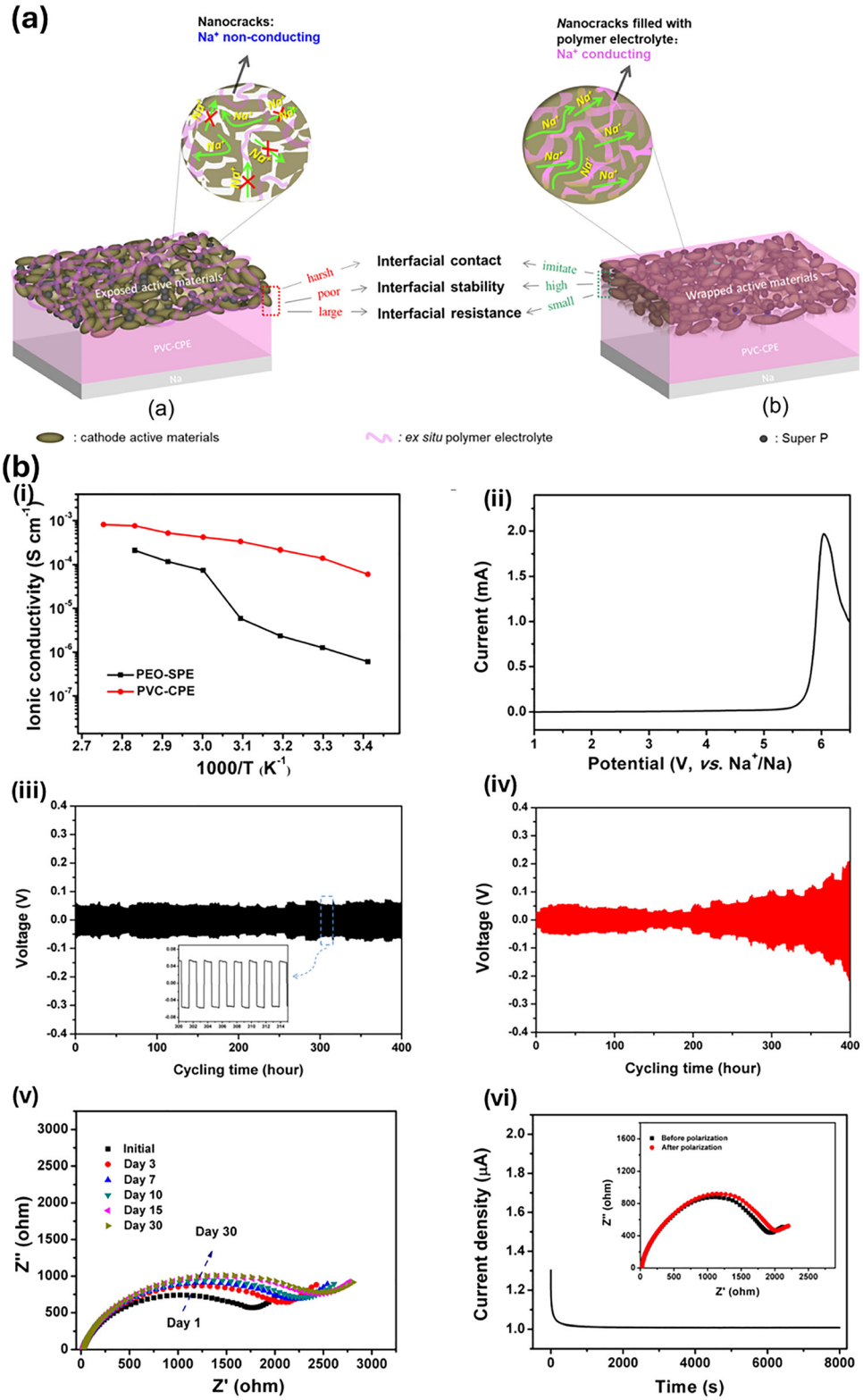

Fig. 27 (a) Schematic comparing Na^+ transfer response and electrode/electrolyte interfaces in conventionally assembled *ex situ* NFM/PVC/Na and *in situ* solidified c-NFM/PVC-CPE/Na batteries. (b) (i) Temperature-dependent ion conductivity of PEO-SPE *vs.* PVC-CPE. (ii) LSV (Na/PVC-CPE/SS, RT). Chronopotentiometry of symmetric Na cells: (iii) PVC-CPE and (iv) liquid electrolyte (1 M $NaClO_4$/PC) at 1.0 mA cm^{-2}. (v) EIS evolution of the Na/PVC-CPE/Na cell during RT aging. (vi) Chronoamperometry of Na/PVC-CPE/Na at 10 mV polarization (inset: pre/post-EIS). reprinted with permission from ref. 265. Copyright © 2019, American Chemical Society).

anion-trapping boron-based CPE (B-CPE) using a BHEMA cross-linker and *in situ* polymerization of PEGMA inside a mechanically strong matrix, using tetraethylene glycol dimethyl ether (TEGDME) as a plasticizer and sodium trifluoromethanesulfonate (NaTf) as the salt for achieving enhanced interfacial stability, Na^+ transference number, and ionic conductivity against the sodium electrode and reduced charge transfer resistance within the electrode and solid electrolyte (Fig. 28a). The developed nanostructured electrolyte design offered high ionic conductivity (2.57×10^{-4} S cm^{-1} at 40 °C), excellent interfacial stability, and a superior Na^+ transference number (0.66). The interfacial stability of the B-CPE and Na metal anode was assessed using a Na‖B-CPE‖Na symmetrical cell. The interfacial resistance stabilized at ~1680 Ω after a minor initial increase, demonstrating excellent long-term compatibility that is critical for advanced solid-state SIBs.

As in their previous study,[265] to achieve enhanced Na^+ ion transfer at the electrode/electrolyte interface and reduce the interfacial resistance in solid-state SIBs, an NFM cathode (c-NFM) composite was developed by synthesizing a polymer electrolyte directly within the cathode structure through an *in situ* heat-induced polymerization process. A full solid-state cell, c-NFM/B-CPE/Na, was fabricated using a single-step *in situ* solidification technique (the CPE was formed directly within the cell *via* an *in situ* polymerization approach; the monomer precursor solution was initially introduced into the coin cell and allowed to stand at ambient temperature for two hours to confirm entire infiltration into the NFM electrode nanopores). Subsequently, the closed cell was transferred to an argon-filled oven and sustained at 70 °C for 10 h to facilitate the polymerization reaction to ensure flawless and tight integration between the polymer electrolyte and the electrodes. Structural analysis (Fig. 28b) revealed a significant morphological difference between the conventional and composite cathodes. The traditional cathode displayed a fractured, porous architecture with poor interparticle connectivity, whereas the c-NFM cathode exhibited an even, continuous surface fully encapsulated by a polymer electrolyte coating. Cross-sectional inspection further confirmed that a continuous and dense polymer phase permeates the entire composite cathode, forming an interconnected ion-conducting network that facilitates efficient and uniform Na^+ ion transport throughout the electrode, eliminating non-conductive 'dead' zones. Moreover, the interface between the composite cathode and solid electrolyte is exceptionally cohesive, with no discernible boundary, indicating close interfacial contact. This unique design not only established continuous ion-diffusion routes but also provided a mechanically compliant buffer layer that could accommodate volume changes during electrochemical cycling.

CPEs combining a ceramic filler within a polymer matrix enhance battery safety; however, a fundamental trade-off exists in CPEs: increasing ceramic filler content enhances ionic conductivity but at the expense of flexibility, leading to higher interfacial resistance and poorer battery performance. Addressing this issue, Ran *et al.*[266] designed a flexible, five-layer gradient composite electrolyte (GCE) employing a Sc, Ge-doped NZSP (NASICON) ceramic filler and PEO matrix. The stiffer, high-conductivity middle layer (40 wt% NZSP–PEO) was selected to provide strong ionic conduction and inhibit dendrite penetration, and the softer, ceramic-poor outer layers ensure intimate interfacial contact with the electrodes that minimizes interfacial resistance. The fabricated GCE cell exhibited a small polarization gap (~0.25 V) and low interfacial resistance (~572 Ω), attributable to the softer outer electrolyte layers. In comparison, a cell with a uniform PEO/NZSP 40 wt% CPE, though possessing higher intrinsic conductivity (6.5×10^{-5} S cm^{-1} *vs.* the GCE's 4.0×10^{-5} S cm^{-1}), suffered from a high polarization gap (~0.79 V) and high interfacial resistance (~1173 Ω) due to poor electrode contact (Fig. 29). Thus, the high filler-loaded GCE mid-layer electrolyte enhances reliability and conduction, while the delicate outer film reduces the interfacial resistance, enabling better overall cell performance.

In another strategy to enhance interfacial contact and cycling efficiency in solid-state SIBs, Cheng *et al.*[272] developed a hybrid solid electrolyte (HSE), comprising the PVDF–HFP polymer matrix with NZSP ceramic particles as a nanofiller with a trace of PEG to improve the ability of the electrolyte to form films. The solid composite film (PVDF–HFP/NZSP) was then briefly soaked in a 1 M $NaClO_4$/(EC+DMC) liquid electrolyte and pressurized (5.0 kPa) to achieve HSE films. EIS revealed the critical advantage of the HSE, which exhibited significantly lower interfacial resistance (152 Ω), as compared to 792 Ω for the pure NZSP-based battery and approaching the benchmark of 118 Ω for a liquid electrolyte system. This low interfacial resistance was attributed to the HSE's flexibility, which enables a 'softer contact' and a larger electrode/electrolyte contact area, thereby facilitating Na^+ ion transfer and depolarizing the charge transfer process at the interfaces. In comparison to CPEs with pure NZSP as a filler, the HSE displayed an excellent reversible capacity of 98 mAh g^{-1} (80.5% theoretical) at 0.2C and a superior capacity retention of 85% following 175 cycles at 0.5C in a solid-state SIB cell with the $Na_3V_2(PO_4)_3$/C cathode. Unlike rigid NZSP ceramics that cannot accommodate the volume variation of the cathode (leading to void formation and skyrocketing interfacial resistance), the flexible HSE maintained intimate contact throughout cycling, providing continuous, interconnected channels for Na^+ migration through the electrode/electrolyte interface. Consequently, the $Na_3V_2(PO_4)_3$/C|HSE|Na cell configuration exhibited low polarization and stable cycle performance due to the superior interfacial stability and mechanical integrity of the HSE. The embedded NASICON particles served a dual role: acting as a mechanical obstruction to dendrite formation and providing efficient channels for Na^+ conduction.

8.1. Comparative analysis of interfacial strategies for the sodium metal anode

Collectively, the evidence from these case studies allows for a comparative analysis of the primary strategies for stabilizing the sodium metal anode interface, highlighting their distinct mechanisms and the critical link between microstructure control and long-term stability. A critical design requirement for

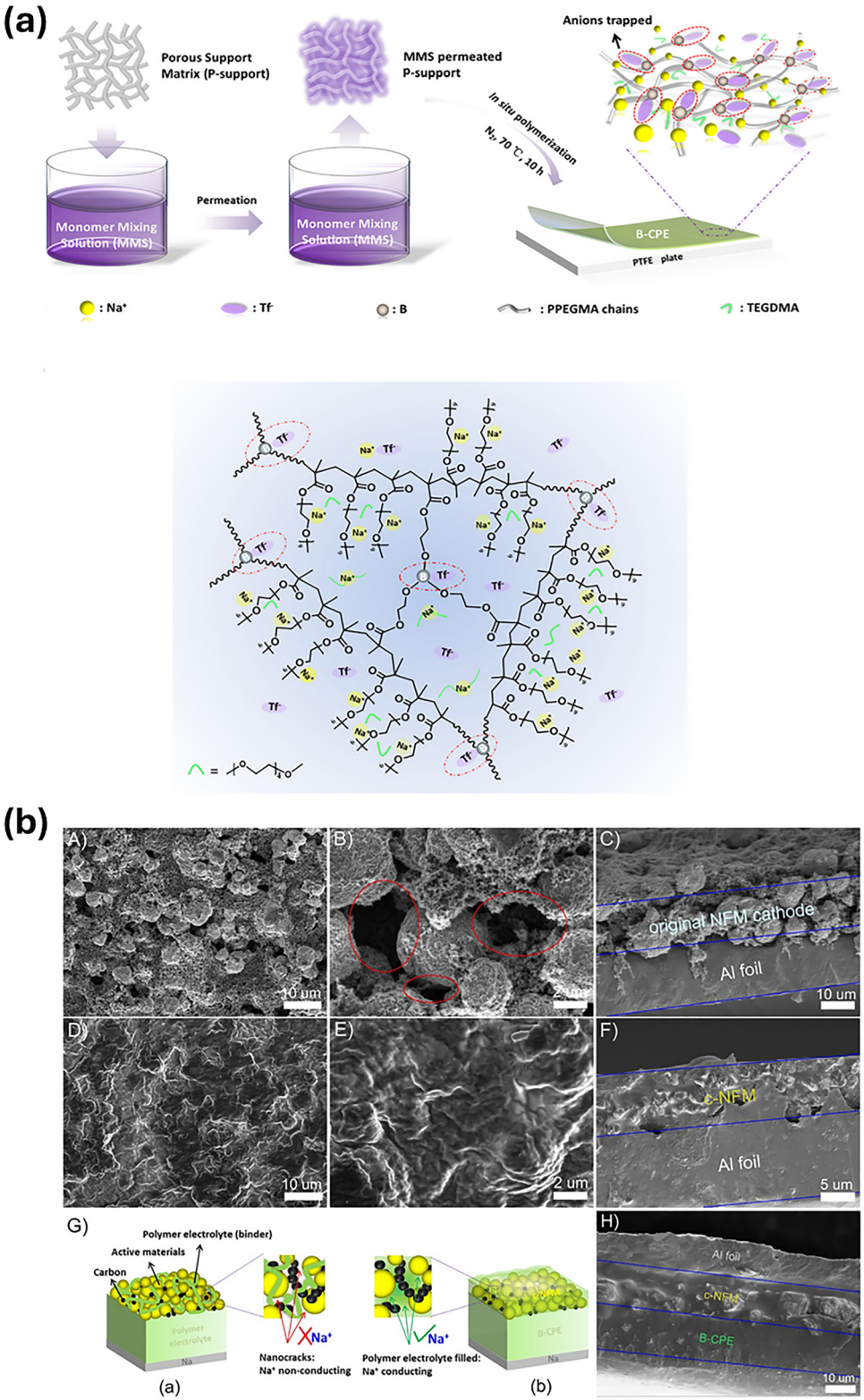

Fig. 28 (a) Schematic overview of the boron-containing composite polymer electrolyte (B-CPE) synthesis and its ion-conduction mechanism. The step-by-step fabrication process of the B-CPE and molecular-level view of the chemical structure, illustrating the distinct existential states of mobile Na^+ ions and anions trapped by Lewis-acidic boron sites. (b) Morphological and structural characterization of cathodes and solid-state SIB assembly. (A)–(C) Original NFM cathode: (A) surface, (B) high-resolution surface, and (C) cross-sectional SEM micrographs. (D)–(F) Composite NFM (c-NFM) cathode: (D) surface, (E) high-magnification surface, and (F) cross-sectional SEM micrographs. (G) Schematic comparing the architectures of (a) a conventional SSB and (b) the c-NFM/B-CPE/Na battery fabricated *via* single-step *in situ* solidification. (H) Cross-sectional SEM micrographs of the c-NFM/B-CPE/Na interface, demonstrating integrated electrolyte–electrode cohesion (reprinted with permission from ref. 79.)

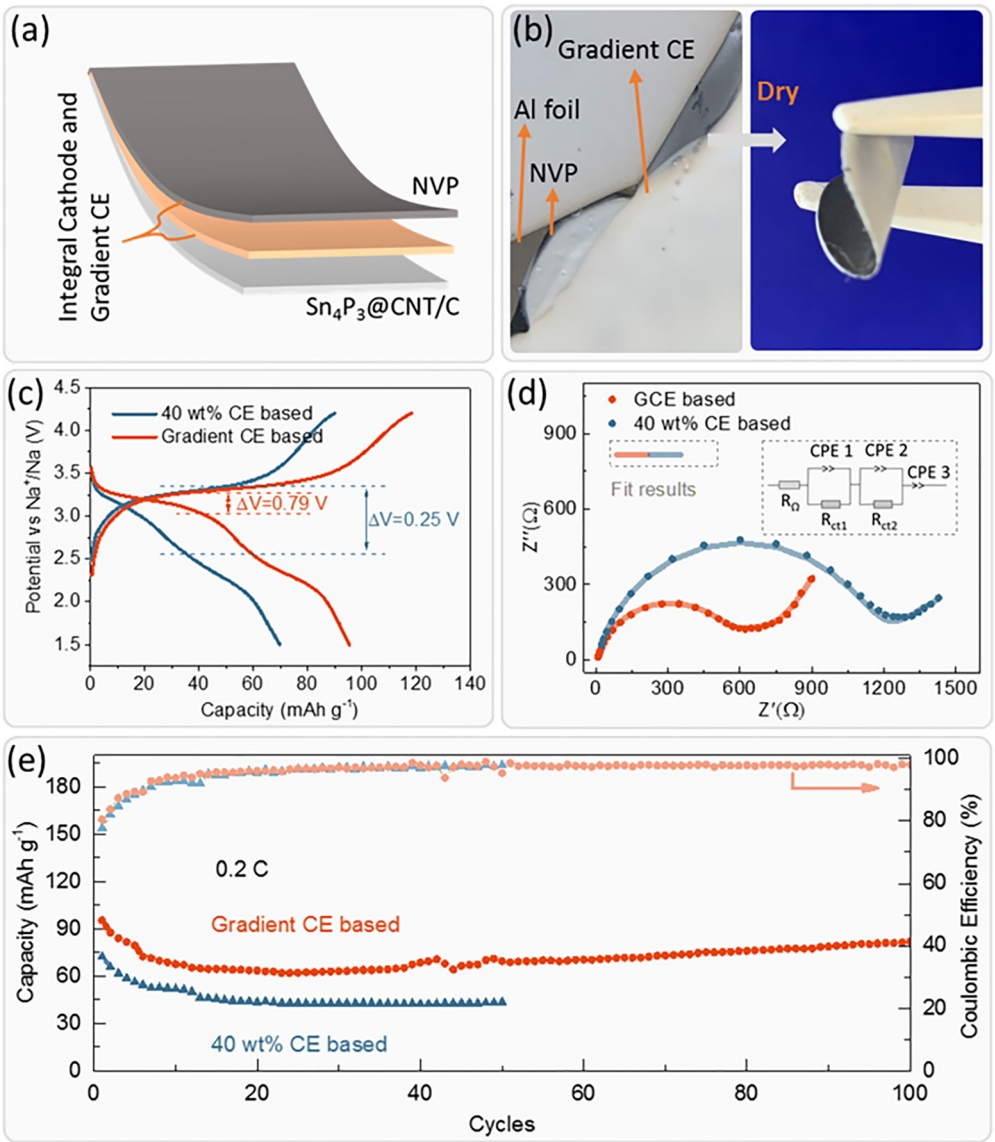

Fig. 29 Characterization of the all-solid-state SIB: (a) schematic of the all-solid-state SIB. (b) Digital photograph of the integrated composite cathode and gradient composite electrolyte (GCE) during fabrication. (c) First-cycle voltage profiles and (d) EIS spectra for SIBs employing the GCE *versus* a uniform 40 wt% NZSP–PEO electrolyte. (e) Corresponding cycling performance (reprinted with permission from ref. 266. Copyright © 2021, American Chemical Society).

stable solid-state SIBs is interfacial engineering at the Na/electrolyte interface to minimize resistance and prevent degradation. The primary strategies include the use of polymer-rich layers, ceramic-rich layers, artificial interphases, and polymer-coated ceramics, each functioning through distinct mechanisms but presenting defined limitations. Polymer-rich layers (*e.g.*, the outer layers in gradient electrolytes in contact with Na metal) minimize interfacial resistance through intimate electrode wetting and suppress void formation.[266] However, their relatively low elastic modulus may limit their ability to mechanically block sodium dendrite propagation at elevated current densities, representing a key limitation for high-rate cycling. In contrast, ceramic-rich layers offer the necessary stiffness for dendrite suppression but suffer from intrinsically poor wettability with Na metal, which results in high interfacial resistance unless intimate contact is actively engineered, as evidenced by the significantly higher interfacial resistance of a pure NZSP ceramic electrolyte (792 Ω) compared to a flexible, polymer-hybridized counterpart (152 Ω).[272] Artificial interphases, such as ferroelectric coatings applied to ceramic scaffolds, operate by electrostatically modifying the interfacial environment. By mitigating space-charge layer buildup, they lower the charge-transfer energy barrier at the Na metal interface. This mechanism is proven by the exceptional long-term stability of symmetric Na‖Na cells employing ferroelectric-engineered composite electrolytes, which retain 86.4% capacity after 650 cycles.[267] The success of this approach depends on ensuring the mechanical homogeneity and adhesion of the

applied coating. Finally, polymer-coated ceramics create a hybrid microstructure where a continuous polymer phase encapsulates ceramic surfaces, eliminating sharp boundaries and improving compatibility with sodium metal. This approach, exemplified by *in situ* polymerization within composite cathodes, establishes seamless ion-diffusion routes and accommodates volume change.[79,265] A fundamental challenge for this strategy is ensuring the uniformity and integrity of the polymer coating to maintain stable interfacial properties. Ultimately, the most effective solutions for durable sodium metal cycling involve microstructures that synthetically combine these strategies. For instance, gradient architectures decouple functions by pairing a stiff, ceramic-rich conductive core with soft, polymer-rich interfacial layers, achieving both low bulk resistance ($\sim$572 Ω) and stable plating/stripping.[266] This comparative analysis demonstrates that microstructural control, whether through gradient layers, artificial ferroelectric interphases, or hybrid polymer-ceramic coatings, is directly correlated with the suppression of interfacial resistance growth and dendrite propagation. The inclusion of specific examples, such as the 86.4% capacity retention after 650 cycles achieved *via* ferroelectric engineering[267] and the fivefold reduction in interfacial resistance realized through polymer–ceramic hybridization,[272] establishes microstructural design as a fundamental prerequisite for achieving long-term cycling stability in solid-state sodium batteries.

9. Conclusion and future perspectives

The journey of CPEs for SIBs represents a pivotal shift in the pursuit of safer, sustainable, and additional robust energy storage. Merging the processability and flexibility of polymer matrices with the mechanical strength and ionic transport capabilities of inorganic fillers, CPEs have successfully addressed critical bottlenecks that plagued earlier solid electrolytes. We have seen how passive fillers like SiO_2 and Al_2O_3 disrupt polymer crystallinity and create conductive interfacial pathways, while active NASICON-type fillers contribute their own innate sodium-ion conductivity, leading to a synergistic enhancement in overall performance. This material-level innovation is complemented by advanced fabrication techniques, from electrospinning to hot-pressing, which enable the development of tailored microstructures. Furthermore, the critical challenge of interfacial resistance has been met with sophisticated solutions, including *in situ* polymerization to ensure perfect electrode contact and the design of hetero-layered or ferroelectric-engineered electrolytes to actively modulate ion transport and stabilize the interphase. The result is a class of electrolytes that simultaneously deliver a wide voltage window, superior ionic conductivity, high Na^+ transference number, and exceptional durability, effectively preventing dendrite formation and enabling long-term cycling stability in all-solid-state cells.

Sustainable solid-state CPEs provide significant environmental benefits for SIBs over traditional liquid electrolytes. They are solids and free of volatile organic solvents, which reduces the risk of leakage, flammability, and harmful emissions. Life-cycle assessment studies suggest that PEO-based CPEs for SIBs can minimize greenhouse-gas emissions and overall energy demand during manufacture due to simplified fabrication techniques that avoid high-temperature sintering and hazardous solvents. Furthermore, the solid form of these electrolytes improves battery safety, hence lowering environmental and operational risks. Sodium is more abundant with broad geographical distribution than lithium, making it a more sustainable resource for polymer electrolyte-based SIBs. CPEs also increase sustainability through potential recyclability; recent research shows that solid-state SIBs utilizing polymer electrolytes can be mechanically or chemically processed to recover polymer and inorganic components, reducing waste and facilitating reuse.[273,274] However, issues persist since some polymer matrices are still petroleum-based, and fillers may necessitate energy-intensive manufacturing. Future research should concentrate on bio-derived polymers, low-energy filler manufacture, and integrated recycling methods to maximize sustainability in SIB applications. As we look to the future, the path forward requires a concerted effort on several fronts. The next generation of fillers must be multi-functional; we need materials that not only conduct ions but also actively trap anions, like advanced boron-based COFs, or possess ferroelectric properties to create built-in electric fields that guide sodium-ion flux and suppress dendrites. A deeper, atomistic grasp of the complex ion transfer mechanisms within the composite matrix and across its interfaces, guided by computational modelling and *in situ* characterization techniques, will be essential for rational design. From a manufacturing perspective, the transition from lab-scale coin cells to practical applications demands a focus on scalable, solvent-free production of ultra-thin, mechanically robust CPE membranes. Another significant trend is the increased use of machine learning/artificial intelligence (ML/AI) to influence electrolyte formulation. Data-driven models can screen multiple polymer-filler combinations, predict optimal loading levels, and identify interactions that improve Na^+ mobility before materials are formulated. This method narrows down promising candidates more effectively than trial-and-error testing, particularly for multi-functional fillers where composition, morphology, and surface chemistry all influence transport. As datasets grow, ML-assisted optimization is expected to become a key tool for designing next-generation composite polymer electrolytes for SIBs. Future electrolyte innovation may benefit from principles in supramolecular chemistry. One promising direction is the use of low-molecular-weight gelators (LMWGs). A growing body of research demonstrates that LMWGs can create supramolecular networks capable of immobilizing liquid electrolytes without the use of lengthy polymer chains. These systems use a distinct self-assembly mechanism and frequently maintain higher solvent mobility than traditional GPE matrices. Typically, small organic molecules self-assemble through non-covalent interactions, such as hydrogen bonding and π–π stacking, to form a three-dimensional nanofibrous network.

This dynamic and reversible process physically immobilizes a liquid electrolyte phase. This self-assembly mechanism provides a fundamental alternative to the polymer chain entanglement that characterizes traditional solid polymer electrolytes. Consequently, exploring LMWG-based electrolytes could unlock novel strategies for engineering more adaptive ion-transport pathways and stable electrode interfaces.

The pathway from promising CPEs to commercially viable solid-state SIBs requires prioritizing solutions for industrial adoption. Near-term engineering challenges include achieving uniform filler dispersion, minimizing interfacial resistance, and fabricating mechanically robust yet thin CPE membranes. More fundamental challenges persist in decoupling the trade-off between mechanical stiffness and ionic conductivity, as well as in understanding ion transport and interfacial stability under high-loading, high-rate conditions. While the fundamental trade-off between ionic conductivity and mechanical strength is being successfully decoupled by designs like 3D ceramic scaffolds and anion-trapping frameworks, the manufacturing scalability of high-performance architectures such as electrospun nanofibers and tailored COFs remains a primary constraint, demanding a shift from complex lab-scale batch synthesis to simplified continuous processes like roll-to-roll production. A second and more paramount challenge for commercializing CPE-based SIBs is ensuring sodium metal interface stability under high areal capacity. While strategies like anion-trapping frameworks and functionalized ceramic nanofibers have achieved stable plating/stripping for thousands of hours at low current densities, their performance under high deposition capacity remains largely unproven. Promising solutions from this review, such as the hetero-layered CPE design with a mechanically reinforced, sodium-compatible layer, and 3D interconnected ceramic scaffolds that provide robust mechanical support, offer pathways to address this. However, their efficacy must be validated in full cells with high-loading cathodes, where the cumulative interfacial stress is significantly greater than that in symmetric cell tests. While stable plating/stripping has been demonstrated at low current densities and moderate capacities, the behavior under high areal loading or fast-charging conditions is less certain. Quantitative evaluation of dendrite suppression, interfacial resistance growth, and capacity retention under these realistic conditions remains a key research need, highlighting the gap between laboratory tests and full-cell performance.

Author contributions

MI: writing original draft; KHK: writing original draft, review and editing; AS: supervision, review, and editing; HH: conceptualization, supervision, review, and editing.

Conflicts of interest

The authors affirm that there are no conflicts of interest, financial or otherwise, related to this work.

Data availability

No primary research results, software or code have been included and no new data were generated or analysed as part of this review.

References

1 X. H. Chen, K. Tee, M. Elnahass and R. Ahmed, *J. Environ. Manage.*, 2023, **345**, 118525.
2 M. K. G. Deshmukh, M. Sameeroddin, D. Abdul and M. A. Sattar, *Mater. Today Proc.*, 2023, **80**, 1756–1759.
3 J. Wang and W. Azam, *Geosci. Front.*, 2024, **15**, 101757.
4 International Energy Agency (IEA), *World Energy Outlook 2023*, IEA, Paris, 2023.
5 I. P. on C. C. (IPCC), Climate Change 2021 – The Physical Science Basis: Working Group I Contribution to the Sixth Assessment Report of the Intergovernmental Panel on Climate Change, Cambridge University Press, Cambridge, 2023.
6 G. De Carne, S. M. Maroufi, H. Beiranvand, V. De Angelis, S. D'Arco, V. Gevorgian, S. Waczowicz, B. Mather, M. Liserre and V. Hagenmeyer, *Electr. Power Syst. Res.*, 2024, **236**, 110963.
7 F. Ahmad, Q. Saeed, S. M. U. Shah, M. A. Gondal and S. Mumtaz, *Nat. Resour. Conserv. Adv. Sustain.*, 2022, 243–270.
8 J. Kim, J. Song, C.-H. Kim, J. Mahseredjian and S. Kim, *J. Mod. Power Syst. Clean Energy*, 2023, **11**, 1576–1587.
9 A. Aghmadi and O. A. Mohammed, *Batteries*, 2024, **10**, 141.
10 M. D. Ahmed and K. M. Maraz, *Mater. Eng. Res.*, 2023, **5**, 265–278.
11 L. Zhang, K. Zhou, X. Dai, C. Lu, J. Li, Y. Yang, G. Huang and S. Xu, *Adv. Energy Mater.*, 2024, **14**, 2402400.
12 K. H. Khan, A. Zafar, H. Rashid, I. Ahmad, G. S. Khan and H. Hussain, *Mater. Adv.*, 2024, **5**, 9613–9625.
13 M. Irfan, S. Muhammad, K. H. Khan, M. Zamurad and H. Gao, *Adv. Sustainable Syst.*, 2026, **10**, e01706.
14 P. Shrivastava, P. A. Naidu, S. Sharma, B. K. Panigrahi and A. Garg, *J. Energy Storage*, 2023, **64**, 107159.
15 I. Rani, S. Arwish, K. H. Khan, M. Zamurad, S. M. Shah and H. Hussain, *J. Appl. Polym. Sci.*, 2025, **142**, e56331.
16 M. Aizudin, W. Fu, R. P. Pottammel, Z. Dai, H. Wang, X. Rui, J. Zhu, C. C. Li, X. Wu and E. H. Ang, *Small*, 2024, **20**, 2305217.
17 Y. Lv, X. Geng, W. Luo, T. Chu, H. Li, D. Liu, H. Cheng, J. Chen, X. He and C. Li, *J. Energy Storage*, 2023, **72**, 108389.
18 L. V. Garcia, Y.-C. Ho, M. M. Myo Thant, D. S. Han and J. W. Lim, *Processes*, 2023, **11**, 418.
19 M. L. Vera, W. R. Torres, C. I. Galli, A. Chagnes and V. Flexer, *Nat. Rev. Earth Environ.*, 2023, **4**, 149–165.
20 H. Rostami, J. Valio, P. Suominen, P. Tynjälä and U. Lassi, *Chem. Eng. J.*, 2024, **486**, 153471.
21 W. Teng, J. Wu, Q. Liang, J. Deng, Y. Xu, Q. Liu, B. Wang, T. Ma, D. Nan and J. Liu, *Energy Environ. Mater.*, 2023, **6**, e12355.

22 S. Qiao, Q. Zhou, M. Ma, H. K. Liu, S. X. Dou and S. Chong, *ACS Nano*, 2023, **17**, 11220–11252.
23 L. Hu, J. Deng, Q. Liang, J. Wu, B. Ge, Q. Liu, G. Chen and X. Yu, *EcoMat*, 2023, **5**, e12269.
24 R. R. Gaddam and G. Zhao, *Handbook of Sodium-Ion Batteries: Materials and Characterization*, Jenny Stanford Publishing, Newyork, 2023.
25 R. Sun, F. Xu, C.-H. Wang, S.-J. Lu, Y.-F. Zhang and H.-S. Fan, *Rare Met.*, 2024, **43**, 1906–1931.
26 Y.-J. Guo, R.-X. Jin, M. Fan, W.-P. Wang, S. Xin, L.-J. Wan and Y.-G. Guo, *Chem. Soc. Rev.*, 2024, **53**, 1–46.
27 H. Bai and Z. Song, *J. Power Sources*, 2023, **580**, 233426.
28 M. Tawalbeh, A. Ali, B. Aljawrneh and A. Al-Othman, *Nano-Struct. Nano-Objects*, 2024, **39**, 101311.
29 J. Zhang, J. Li, H. Wang and M. Wang, *Front. Chem.*, 2023, **11**, 1253959.
30 F. Wang, Z. Jiang, Y. Zhang, Y. Zhang, J. Li, H. Wang, Y. Jiang, G. Xing, H. Liu and Y. Tang, *eScience*, 2024, **4**, 100181.
31 R. Wanison, W. N. H. Syahputra, N. Kammuang-lue, P. Sakulchangsatjatai, C. Chaichana, V. U. Shankar, P. Suttakul and Y. Mona, *J. Energy Storage*, 2024, **79**, 113497.
32 L. Zhu, Y. Li, J. Zhao, J. Liu, L. Wang and J. Lei, *Green Energy Environ.*, 2023, **8**, 1–12.
33 J. Lu, Y. Chen, Y. Lei, P. Jaumaux, H. Tian and G. Wang, *Nanomicro Lett.*, 2025, **17**, 194.
34 A. Machín, C. Morant and F. Márquez, *Batteries*, 2024, **10**, 29.
35 S. Yang, J. Hu, F. Jiang, H. Yuan, H. S. Park and J. Huang, *InfoMat*, 2024, **6**, e12512.
36 S. Cui, X. Wu, Y. Yang, M. Fei, S. Liu, G. Li and X.-P. Gao, *ACS Energy Lett.*, 2021, **7**, 42–52.
37 Y. Du, Y. Xie, X. Liu, H. Jiang, F. Wu, H. Wu, Y. Mei and D. Xie, *ACS Sustainable Chem. Eng.*, 2023, **11**, 4498–4508.
38 S. Fu, L.-L. Zuo, P.-S. Zhou, X.-J. Liu, Q. Ma, M.-J. Chen, J.-P. Yue, X.-W. Wu and Q. Deng, *Mater. Chem. Front.*, 2021, **5**, 5211–5232.
39 J. Qian, B. Jin, Y. Li, X. Zhan, Y. Hou and Q. Zhang, *J. Energy Chem.*, 2021, **56**, 420–437.
40 D. K. Smith, *Soft Matter*, 2024, **20**, 10–70.
41 C. Zhong, Y. Deng, W. Hu, J. Qiao, L. Zhang and J. Zhang, *Chem. Soc. Rev.*, 2015, **44**, 7484–7539.
42 A. Thamizhanban, K. Lalitha and S. Nagarajan, *Emerging Nanostructured Materials for Energy and Environmental Science*, 2019, pp. 443–470.
43 K. Hanabusa, K. Hiratsuka, M. Kimura and H. Shirai, *Chem. Mater.*, 1999, **11**, 649–655.
44 V. R. Basrur, J. Guo, C. Wang and S. R. Raghavan, *ACS Appl. Mater. Interfaces*, 2013, **5**, 262–267.
45 H. Li, C. Huang, Z. Teng, Y. Luo, C. Zhang, L. Wu, W. Huang, T. Zhao, L. Dong and W. Chen, *Polymers*, 2024, **16**, 1680.
46 F. Ahmad, N. Bielejewska, D. Pakulski and M. Bielejewski, *Macromolecules*, 2025, **58**, 9786–9798.
47 Z. Li, P. Liu, K. Zhu, Z. Zhang, Y. Si, Y. Wang and L. Jiao, *Energy Fuels*, 2021, **35**, 9063–9079.
48 Y. Dong, P. Wen, H. Shi, Y. Yu and Z. S. Wu, *Adv. Funct. Mater.*, 2024, **34**, 2213584.
49 S. Liu, L. Kang, J. Henzie, J. Zhang, J. Ha, M. A. Amin, M. S. A. Hossain, S. C. Jun and Y. Yamauchi, *ACS Nano*, 2021, **15**, 18931–18973.
50 Y. Sun, F. Zeng, Y. Zhu, P. Lu and D. Yang, *J. Energy Chem.*, 2021, **61**, 531–552.
51 D. Lee, A. Kumar Kakarla, S. Sun, P. Joohyun Kim and J. Choi, *ChemElectroChem*, 2025, **12**, e202400612.
52 K. Wu, J. Tan, Z. Liu, C. Bao, A. Li, Q. Liu and B. Li, *J. Energy Chem.*, 2023, **57**, 351–362.
53 Y. Liao, X. Xu, X. Luo, S. Ji, J. Zhao, J. Liu and Y. Huo, *Batteries*, 2023, **9**, 439.
54 H. Wang, L. Sheng, G. Yasin, L. Wang, H. Xu and X. He, *Energy Storage Mater.*, 2020, **33**, 188–215.
55 L. Han, L. Wang, Z. Chen, Y. Kan, Y. Hu, H. Zhang and X. He, *Adv. Funct. Mater.*, 2023, **33**, 2300892.
56 D. K. Maurya, R. Dhanusuraman, Z. Guo and S. Angaiah, *Adv. Compos. Hybrid Mater.*, 2022, **5**(4), 2651–2674.
57 B. Zheng, X. Lin, X. Zhang, D. Wu and K. Matyjaszewski, *Adv. Funct. Mater.*, 2020, **30**, 1907006.
58 A. Selim, *Polymer Membranes: Increasing Energy Efficiency*, 2024, p. 195.
59 S. Kumar, R. Raghupathy and M. Vittadello, *Batteries*, 2024, **10**, 73.
60 Y. He, S. Yang, C. Liu, Y. Ouyang, Y. Li, H. Zhu, Y. Yao, H. Yang, X. Rui and Y. Yu, *Small Methods*, 2025, 2402220.
61 K. K. Senthilkumar, R. Thiruvengadathan and R. B. T. S. Raghava, *Electrochem*, 2025, **6**, 6.
62 A. Gabryelczyk and A. Swiderska-Mocek, *Chem. – Eur. J.*, 2024, **30**, e202304207.
63 X. Shi, C. Zheng, X. Li, Z. Zheng, Z. Shu, J. Zhou and Y. Zhu, *J. Mater. Chem. A*, 2025, **13**, 16728–16739.
64 N. S. Choi, J. G. Han, S. Y. Ha, I. Park and C. K. Back, *RSC Adv.*, 2015, **5**(4), 2732–2748.
65 X. Yang, M. Jiang, X. Gao, D. Bao, Q. Sun, N. Holmes, H. Duan, S. Mukherjee, K. Adair and C. Zhao, *Energy Environ. Sci.*, 2020, **13**, 1318–1325.
66 D. K. Maurya, B. Bazri, P. Srivastava, J. Huang, Y. Hung, W. Huang, D. Wei and R. Liu, *Adv. Energy Mater.*, 2024, **14**, 2402402.
67 Q. Liu and L. Wang, *Adv. Energy Mater.*, 2023, **13**, 2301742.
68 K. Deshmukh, K. Varade, S. M. Rajesh, V. Sharma, P. Kabudake, S. Nehe and V. Lokawar, *J. Mater. Sci.*, 2025, **60**, 3609–3633.
69 B. Sun, P. Xiong, U. Maitra, D. Langsdorf, K. Yan, C. Wang, J. Janek, D. Schröder and G. Wang, *Adv. Mater.*, 2020, **32**, 1903891.
70 X. Shan, Z. Song, H. Ding, L. Li, Y. Tian, A. P. Sokolov, M. Tian, K. Xu and P.-F. Cao, *Energy Environ. Sci.*, 2024, **17**, 8457–8481.
71 K. A. M. Attia, A. M. Abdel-Raoof, A. Serag, S. M. Eid and A. E. Abbas, *RSC Adv.*, 2022, **12**, 17536–17549.
72 M. M. Hassan, X.-Y. Wang, A. A. Bristi, R. Yang, X. Li and Q. Lu, *Nano Energy*, 2024, **128**, 109971.

73 C. Devi, J. Gellanki, H. Pettersson and S. Kumar, *Sci. Rep.*, 2021, **11**, 20180.
74 A. Chandra, A. Chandra and K. Thakur, *Arabian J. Chem.*, 2016, **9**, 400–407.
75 L. Zhao, M. Hou, K. Ren, D. Yang, F. Li, X. Yang, Y. Zhou, D. Zhang, S. Liu and Y. Lei, *Small Methods*, 2024, 2301579.
76 A. Chandra, A. Chandra and K. Thakur, *Indian J. Pure Appl. Phys.*, 2013, **51**, 44–48.
77 L. Zhao, M. Hou, K. Ren, D. Yang, F. Li, X. Yang, Y. Zhou, D. Zhang, S. Liu, Y. Lei and F. Liang, *Small Methods*, 2024, **8**, 2301579.
78 M. J. A. Hore, L. T. J. Korley and S. K. Kumar, *J. Appl. Phys.*, 2020, **128**, 030401.
79 S. Chen, F. Feng, H. Che, Y. Yin and Z.-F. Ma, *Chem. Eng. J.*, 2021, **406**, 126736.
80 J. Liu, Z. Dong, K. Huan, Z. He, Q. Zhang, D. Deng and L. Luo, *Molecules*, 2024, **29**, 2769.
81 N. Deng, W. Duan, W. Yu, Y. Feng, Z. Feng, X. Feng, Z. Peng, H. Xiang, Y. Liu and W. Kang, *Inorg. Chem. Front.*, 2024, **11**, 5125–5140.
82 A. Sarkar, V. R. Dharmaraj, C.-H. Yi, K. Iputera, S.-Y. Huang, R.-J. Chung, S.-F. Hu and R.-S. Liu, *Chem. Rev.*, 2023, **123**, 9497–9564.
83 D. K. Maurya, V. Murugadoss, Z. Guo and S. Angaiah, *ACS Appl. Energy Mater.*, 2021, **4**, 8475–8487.
84 P. Arjunan, M. Kouthaman, R. Subadevi, K. Diwakar, W.-R. Liu, C.-H. Huang and M. Sivakumar, *Polymers*, 2020, **12**, 405.
85 F. Sun, J. Yang, Q. Shen, M. Li, H. Du and D. Y. Xing, *J. Environ. Manage.*, 2021, **297**, 113363.
86 R. Deivanayagam and R. Shahbazian-Yassar, *Batteries Supercaps*, 2021, **4**, 596–606.
87 M. A. Careem, I. S. M. Noor and A. K. Arof, *Polymer Electrolytes: Characterization Techniques and Energy Applications*, 2020, pp. 23–64.
88 M. Forsyth, H. Yoon, F. Chen, H. Zhu, D. R. MacFarlane, M. Armand and P. C. Howlett, *J. Phys. Chem. C*, 2016, **120**, 4276–4286.
89 D. Dong, H. Zhang, B. Zhou, Y. Sun, H. Zhang, M. Cao, J. Li, H. Zhou, H. Qian and Z. Lin, *Chem. Commun.*, 2019, **55**, 1458–1461.
90 J. Evans, C. A. Vincent and P. G. Bruce, *Polymer*, 1987, **28**, 2324–2328.
91 M. Doyle and J. Newman, *J. Electrochem. Soc.*, 1995, **142**, 3465.
92 J. Mindemark, M. J. Lacey, T. Bowden and D. Brandell, *Prog. Polym. Sci.*, 2018, **81**, 114–143.
93 Y. Zhu, Y. Yang, L. Fu and Y. Wu, *Electrochim. Acta*, 2017, **224**, 405–411.
94 W. Zhang, Z. Tu, J. Qian, S. Choudhury, L. A. Archer and Y. Lu, *Small*, 2018, **14**, 1703001.
95 H. Ben Youcef, B. Orayech, J. M. L. Del Amo, F. Bonilla, D. Shanmukaraj and M. Armand, *Solid State Ionics*, 2020, **345**, 115168.
96 P. Wang, H. Zhang, J. Chai, T. Liu, R. Hu, Z. Zhang, G. Li and G. Cui, *Solid State Ionics*, 2019, **337**, 140–146.
97 J. Li, H. Zhu, X. Wang, M. Armand, D. R. MacFarlane and M. Forsyth, *Electrochim. Acta*, 2015, **175**, 232–239.
98 Q. Pan, Z. Li, W. Zhang, D. Zeng, Y. Sun and H. Cheng, *Solid State Ionics*, 2017, **300**, 60–66.
99 R. Sarkar and T. K. Kundu, *J. Chem. Sci.*, 2018, **130**, 1–18.
100 J.-K. Kim, Y. J. Lim, H. Kim, G.-B. Cho and Y. Kim, *Energy Environ. Sci.*, 2015, **8**, 3589–3596.
101 L. Othman, K. B. M. Isa, Z. Osman and R. Yahya, *Mater. Today Proc.*, 2017, **4**, 5122–5129.
102 S. Janakiraman, A. Surendran, R. Biswal, S. Ghosh, S. Anandhan and A. Venimadhav, *J. Electroanal. Chem.*, 2019, **833**, 411–417.
103 Y. Horowitz, C. Schmidt, D. Yoon, L. M. Riegger, L. Katzenmeier, G. M. Bosch, M. Noked, Y. Ein-Eli, J. Janek and W. G. Zeier, *Energy Technol.*, 2020, **8**, 2000580.
104 X. Yu and A. Manthiram, *Energy Environ. Sci.*, 2018, **11**, 527–543.
105 V. Prasannavenkadesan, V. Katiyar and A. S. Achalkumar, *RSC Appl. Polym.*, 2025, **3**, 499–531.
106 J. Tu, C. Chang, J. Wang, H. Lei, R. V. Kumar, M. Wang and S. Jiao, *Energy Environ. Mater.*, 2024, **7**, e12664.
107 Y. Lu, L. Li, Q. Zhang, Z. Niu and J. Chen, *Joule*, 2018, **2**, 1747–1770.
108 Y. Tian, T. Shi, W. D. Richards, J. Li, J. C. Kim, S.-H. Bo and G. Ceder, *Energy Environ. Sci.*, 2017, **10**, 1150–1166.
109 M. Chen, J. Zhang, X. Ji, J. Fu and G. Feng, *Curr. Opin. Electrochem.*, 2022, **34**, 101030.
110 A. Méry, S. Rousselot, D. Lepage and M. Dollé, *Materials*, 2021, **14**(14), 3840.
111 L. Chen, S. Venkatram, C. Kim, R. Batra, A. Chandrasekaran and R. Ramprasad, *Chem. Mater.*, 2019, **31**, 4598–4604.
112 X. Xu, Y. Wang, Q. Yi, X. Wang, R. A. Paredes Camacho, H. Kungl, R. A. Eichel, L. Lu and H. Zhang, *ChemSusChem*, 2023, **16**(8), e202202152.
113 P. Yao, H. Yu, Z. Ding, Y. Liu, J. Lu, M. Lavorgna, J. Wu and X. Liu, *Front. Chem.*, 2019, **7**, 522.
114 V. Bocharova and A. P. Sokolov, *Macromolecules*, 2020, **53**, 4141–4157.
115 Q. Yang, A. Wang, J. Luo and W. Tang, *Chin. J. Chem. Eng.*, 2022, **43**, 202–215.
116 Y. Shao, H. Gudla, J. Mindemark, D. Brandell and C. Zhang, *Acc. Chem. Res.*, 2024, **57**, 1123–1134.
117 S. J. Lilley, Y. G. Andreev and P. G. Bruce, *J. Am. Chem. Soc.*, 2006, **128**, 12036–12037.
118 A. Chandra, A. Chandra, R. S. Dhundhel and A. Bhatt, *Mater. Today Proc.*, 2020, **33**, 5081–5084.
119 L. Qiao, X. Judez, T. Rojo, M. Armand and H. Zhang, *J. Electrochem. Soc.*, 2020, **167**, 070534.
120 C. Papamichail, O. Techlemtzi, G. Nikolakakou and E. Glynos, *ACS Macro Lett.*, 2025, **14**, 225–230.
121 F. Gebert, J. Knott, R. Gorkin, S. L. Chou and S. X. Dou, *Energy Storage Mater.*, 2021, **36**, 10–30.
122 X. Yang, J. Liu, N. Pei, Z. Chen, R. Li, L. Fu, P. Zhang and J. Zhao, *Nanomicro Lett.*, 2023, **15**, 74.

123 Y. Fu, Z. Gu, Q. Gan and Y.-W. Mai, *Mater. Sci. Eng., R*, 2024, **160**, 100815.
124 F. Croce, L. Persi, B. Scrosati, F. Serraino-Fiory, E. Plichta and M. A. Hendrickson, *Electrochim. Acta*, 2001, **46**, 2457–2461.
125 P. M. Veelken, M. Wirtz, R. Schierholz, H. Tempel, H. Kungl, R.-A. Eichel and F. Hausen, *Nanomaterials*, 2022, **12**, 654.
126 X. Xu, Y. Wang, Q. Yi, X. Wang, R. A. Paredes Camacho, H. Kungl, R. A. Eichel, L. Lu and H. Zhang, *ChemSusChem*, 2023, **16**, e202202152.
127 Z.-Y. Li, Z. Li, J.-L. Fu and X. Guo, *Rare Met.*, 2023, **42**, 1–16.
128 Y. Wang, Z. Wang, J. Sun, F. Zheng, M. Kotobuki, T. Wu, K. Zeng and L. Lu, *J. Power Sources*, 2020, **454**, 227949.
129 G. Foran, N. Verdier, D. Lepage, C. Malveau, N. Dupré and M. Dollé, *Polymers*, 2021, **13**, 1207.
130 A. Zheng and S. G. Greenbaum, *Front. Chem.*, 2023, **11**, 1275907.
131 J. S. Moreno, M. Armand, M. B. Berman, S. G. Greenbaum, B. Scrosati and S. Panero, *J. Power Sources*, 2014, **248**, 695–702.
132 W. S. Price, *Concepts Magn. Reson.*, 1997, **9**, 299–336.
133 R. K. Harris, E. D. Becker, S. M. Cabral de Menezes, R. Goodfellow and P. Granger, *Magn. Reson. Chem.*, 2002, **40**, 489–505.
134 J. Adebahr, A. S. Best, N. Byrne, P. Jacobsson, D. R. Macfarlane and M. Forsyth, *Phys. Chem. Chem. Phys.*, 2003, **5**, 720–725.
135 A. Hosseinioun, P. Nürnberg, M. Schönhoff, D. Diddens and E. Paillard, *RSC Adv.*, 2019, **9**, 27574–27582.
136 G. Foran, D. Mankovsky, N. Verdier, D. Lepage, A. Prébé, D. Aymé-Perrot and M. Dollé, *iScience*, 2020, **23**, 101597.
137 F. Kaneko, S. Wada, M. Nakayama, M. Wakihara and S. Kuroki, *ChemPhysChem*, 2009, **10**, 1911–1915.
138 M. Chintapalli, K. Timachova, K. R. Olson, S. J. Mecham, D. Devaux, J. M. DeSimone and N. P. Balsara, *Macromolecules*, 2016, **49**, 3508–3515.
139 D. J. Eyckens and L. C. Henderson, *Front. Chem.*, 2019, **7**, 263.
140 M. Videa, W. Xu, B. Geil, R. Marzke and C. A. Angell, *J. Electrochem. Soc.*, 2001, **148**, A1352–A1356.
141 F. Kaneko, S. Wada, M. Nakayama, M. Wakihara and S. Kuroki, *ChemPhysChem*, 2009, **10**, 1911–1915.
142 M. Chintapalli, K. Timachova, K. R. Olson, S. J. Mecham, D. Devaux, J. M. DeSimone and N. P. Balsara, *Macromolecules*, 2016, **49**, 3508–3515.
143 B. Sun, J. Mindemark, E. V. Morozov, L. T. Costa, M. Bergman, P. Johansson, Y. Fang, I. Furó and D. Brandell, *Phys. Chem. Chem. Phys.*, 2016, **18**, 9504–9513.
144 G. Foran, N. Verdier, D. Lepage, C. Malveau, N. Dupré and M. Dollé, *Polymers*, 2021, **13**, 1207.
145 K. Xu, *Chem. Rev.*, 2014, **114**, 11503–11618.
146 Y. Tominaga and K. Yamazaki, *Chem. Commun.*, 2014, **50**, 4448–4450.
147 K. Timachova, G. K. Sethi, R. Bhattacharya, I. Villaluenga and N. P. Balsara, *Mol. Syst. Des. Eng.*, 2019, **4**, 357–364.
148 W. Gorecki, P. Donoso, C. Berthier, M. Mali, J. Roos, D. Brinkmann and M. B. Armand, *Solid State Ionics*, 1988, **28**, 1018–1022.
149 A. Martynov, L. Sushama and R. Laprise, *Boreal Environ. Res.*, 2010, **15**, 143.
150 S. G. Greenbaum, *Polym. Adv. Technol.*, 1993, **4**, 172–178.
151 L. Yang, Y. Jiang, X. Liang, Y. Lei, T. Yuan, H. Lu, Z. Liu, Y. Cao and J. Feng, *ACS Appl. Energy Mater.*, 2020, **3**, 10053–10060.
152 P. Stilbs and I. Furó, *Curr. Opin. Colloid Interface Sci.*, 2006, **11**, 3–6.
153 Z. Zhang and L. A. Madsen, *J. Chem. Phys.*, 2014, **140**, 084204.
154 M. P. Rosenwinkel and M. Schönhoff, *J. Electrochem. Soc.*, 2019, **166**, A1977–A1983.
155 C. Mönich, R. Andersson, G. Hernández, J. Mindemark and M. Schönhoff, *J. Am. Chem. Soc.*, 2024, **146**, 11105–11114.
156 H. Yin, C. Han, Q. Liu, F. Wu, F. Zhang and Y. Tang, *Small*, 2021, **17**, 2006627.
157 J. Fu, Z. Li, X. Zhou and X. Guo, *Mater. Adv.*, 2022, **3**, 3809–3819.
158 M. Sahu, N. Kumar, R. C. Agrawal and Y. K. Mahipal, *Macromol. Symp.*, 2024, **413**, 2200212.
159 N. Kumar, D. K. Sahu and Y. K. Mahipal, *J. Mater. Res.*, 2023, **38**, 2506–2518.
160 A. Boonmee and K. Jarukumjorn, *Polym. Bull.*, 2020, **77**, 3457–3472.
161 W. Lyu, G. He and T. Liu, *ChemistryOpen*, 2020, **9**, 713–718.
162 M. Brza, S. B. Aziz, S. Raza Saeed, M. H. Hamsan, S. R. Majid, R. T. Abdulwahid, M. F. Z. Kadir and R. M. Abdullah, *Membranes*, 2020, **10**, 381.
163 Y. L. Ni'mah, F. A. Rusydiyah and S. Suprapto, *AIP Conference Proceedings*, AIP Publishing, 2024, vol. 3071.
164 D. Lin, W. Liu, Y. Liu, H. R. Lee, P.-C. Hsu, K. Liu and Y. Cui, *Nano Lett.*, 2016, **16**, 459–465.
165 Y. L. Nimah, Z. Muhaiminah and S. Suprapto, *Polymers*, 2021, **13**, 4240.
166 K. R. P. Sabu, K. V. C. Rao and C. G. R. Nair, *Bull. Chem. Soc. Jpn.*, 1991, **64**, 1920–1925.
167 S. V. Dorozhkin, *Materials*, 2009, **2**, 399–498.
168 B. Ghiasi, Y. Sefidbakht and M. Rezaei, *Nanomaterials for advanced biological applications*, Springer, 2019, pp. 85–120.
169 A. Szcześ, L. Hołysz and E. Chibowski, *Adv. Colloid Interface Sci.*, 2017, **249**, 321–330.
170 S. Wang, S. Wen, M. Shen, R. Guo, X. Cao, J. Wang and X. Shi, *Int. J. Nanomed.*, 2011, 3449–3459.
171 Y. Liang, Y. Liu, D. Chen, L. Dong, Z. Guang, J. Liu, B. Yuan, M. Yang, Y. Dong and Q. Li, *Mater. Today Energy*, 2021, **20**, 100694.
172 K. Karuppasamy, C. Vijil Vani, R. Antony, S. Balakumar and X. Sahaya Shajan, *Polym. Bull.*, 2013, **70**, 2531–2545.
173 S. Abouricha, A. Ihechmyen, H. Aziam, H. A. Said, A. Ouarga, N. Oueldna, N. Sabi, H. Noukrati, M. Lahcini,

I. Saadoune and H. Ben youcef, *J. Energy Storage*, 2024, **95**, 111967.
174 V. Vijayakumar, M. Ghosh, K. Asokan, S. B. Sukumaran, S. Kurungot, J. Mindemark, D. Brandell, M. Winter and J. R. Nair, *Adv. Energy Mater.*, 2023, **13**, 2203326.
175 X. Zhang, J. Xie, F. Shi, D. Lin, Y. Liu, W. Liu, A. Pei, Y. Gong, H. Wang and K. Liu, *Nano Lett.*, 2018, **18**, 3829–3838.
176 P. Yang, J. Qiang, J. Chen, Z. Zhang, M. Xu and L. Fei, *Angew. Chem., Int. Ed.*, 2025, **64**, e202414770.
177 S. Wu, C. Ji, F. Tang, L. Zhang, K. Fang, F. Huang and Q. Wei, *Energy Storage Mater.*, 2024, **67**, 103308.
178 S. Kmiec, E. Ruoff, J. Darga, A. Bodratti and A. Manthiram, *ACS Appl. Mater. Interfaces*, 2023, **15**, 20946–20957.
179 T. Kang, C. Sun, Y. Li, T. Song, Z. Guan, Z. Tong, J. Nan and C. Lee, *Adv. Energy Mater.*, 2023, **13**, 2204083.
180 J. Zhuang, D. Wu, H. Zou, Z. Chen and H. Cheng, Haifeng and Chen, Zhuo and Cheng, Hu, Defective Mof-Supported Poly (Ethylene Oxide) Composite Polymer Electrolytes for High-Performance All-Solid-State Lithium Ion Batteries, *Electrochim. Acta*, 2025, **513**, 145543.
181 J. Guo, F. Feng, X. Jiang, R. Wang, D. Chu, Y. Ren, F. Chen, P. He, Z. Ma and S. Chen, *Adv. Funct. Mater.*, 2024, 2313496.
182 X. Guan, Z. Jian, X. Liao, W. Liao, Y. Huang, D. Chen, R. K. Y. Li and C. Liu, *Nano Res.*, 2024, **17**, 4171–4180.
183 L. Du, B. Zhang, W. Deng, Y. Cheng, L. Xu and L. Mai, *Adv. Energy Mater.*, 2022, **12**, 2200501.
184 Y. Huang, B. Chen, J. Duan, F. Yang, T. Wang, Z. Wang, W. Yang, C. Hu, W. Luo and Y. Huang, *Angewandte Chemie*, 2020, **132**, 3728–3733.
185 Z. Sun, Y. Li, S. Zhang, L. Shi, H. Wu, H. Bu and S. Ding, *J. Mater. Chem. A*, 2019, **7**, 11069–11076.
186 L. Ruan, X. Yao, Y. Chang, L. Zhou, G. Qin and X. Zhang, *Polymers*, 2018, **10**, 228.
187 J. Yang, X. Wang, G. Zhang, A. Ma, W. Chen, L. Shao, C. Shen and K. Xie, *Front. Chem.*, 2019, **7**, 388.
188 J. Wei, X. Zheng, W. Lin, Y. Si, K. Ji, C. Wang and M. Chen, *J. Alloys Compd.*, 2022, **909**, 164825.
189 K. Shu, J. Zhou, X. Wu, X. Liu, L. Sun, Y. Wang, S. Tian, H. Niu, Y. Duan and G. Hu, *J. Mater. Chem. A*, 2025, **13**, 27947–27951.
190 M. Sadiq, M. M. H. Raza, M. Zulfequar and J. Ali, *J. Polym. Res.*, 2022, **29**, 131.
191 A. Arya, N. G. Saykar and A. L. Sharma, *J. Appl. Polym. Sci.*, 2019, **136**, 47361.
192 D. Shanmukaraj, G. X. Wang, H.-K. Liu and R. Murugan, *Polym. Bull.*, 2008, **60**, 351–361.
193 T. Sathyanathan and C. Pugazhendhi Sugumaran, *Int. J. Nanosci.*, 2020, **19**, 1950035.
194 S. Jeya and B. Sundaresan, *Solid State Ionics*, 2023, **399**, 116301.
195 M. Sadiq, S. Tanwar, M. M. H. Raza, S. M. Aalam, M. Sarvar, M. Zulfequar, A. L. Sharma and J. Ali, *Energy Storage*, 2022, **4**, e345.
196 Z. Li, J. Fu, X. Zhou, S. Gui, L. Wei, H. Yang, H. Li and X. Guo, *Adv. Sci.*, 2023, **10**, 2201718.
197 H. Yang and N. Wu, *Energy Sci. Eng.*, 2022, **10**, 1643–1671.
198 Y. Li, Z. Sun, X. Yuan, H. Jin and Y. Zhao, *ACS Appl. Mater. Interfaces*, 2023, **15**, 49321–49328.
199 Z. Zhang, K. Xu, X. Rong, Y.-S. Hu, H. Li, X. Huang and L. Chen, *J. Power Sources*, 2017, **372**, 270–275.
200 J. F. Wu, Z. Y. Yu, Q. Wang and X. Guo, *Energy Storage Mater.*, 2020, **24**, 467–471.
201 H. Ahmad, K. T. Kubra, A. Butt, U. Nisar, F. J. Iftikhar and G. Ali, *J. Power Sources*, 2023, **581**, 233518.
202 M. Jagan and S. P. Vijayachamundeeswari, *Ionics*, 2024, **30**, 647–675.
203 Z. Wang, Z. Wu, Q. Ma, J. Zhou, Q. Zhang, K. Yu, P. Lv and W. Wei, *Chem. Eng. J.*, 2024, **500**, 156722.
204 J. Zhang, Y. Liu, X. Zhao, L. He, H. Liu, Y. Song, S. Sun, Q. Li, X. Xing and J. Chen, *Adv. Mater.*, 2020, **32**, 1906348.
205 R. Chen, D. S. Butenko, S. Li, X. Zhang, G. Li, I. V. Zatovsky and W. Han, *Chin. Chem. Lett.*, 2024, **35**, 108358.
206 Y. Wang, Y. Liu, P. He, J. Jin, X. Zhao, Q. Shen, J. Li, X. Qu, Y. Liu and L. Jiao, *Energy Environ. Mater.*, 2024, **7**, e12519.
207 Z. Zhang, Q. Zhang, C. Ren, F. Luo, Q. Ma, Y.-S. Hu, Z. Zhou, H. Li, X. Huang and L. Chen, *J. Mater. Chem. A*, 2016, **4**, 15823–15828.
208 Z. Zhang, S. Zhang, S. Geng, S. Zhou, Z. Hu and J. Luo, *Energy Storage Mater.*, 2022, **51**, 19–28.
209 W. Niu, L. Chen, Y. Liu and L.-Z. Fan, *Chem. Eng. J.*, 2020, **384**, 123233.
210 X. Yu, L. Xue, J. B. Goodenough and A. Manthiram, *Adv. Funct. Mater.*, 2021, **31**, 2002144.
211 M. Liu, X. Guan, H. Liu, X. Ma, Q. Wu, S. Ge, H. Zhang and J. Xu, *Chem. Eng. J.*, 2022, **445**, 136436.
212 D. Cai, D. Wang, Y. Chen, S. Zhang, X. Wang, X. Xia and J. Tu, *Chem. Eng. J.*, 2020, **394**, 124993.
213 W. Wang, M. Ding, S. Chen, J. Weng, P. Zhang, W. Yuan, A. Bi and P. Zhou, *Chem. Eng. J.*, 2024, **491**, 151989.
214 C. Niu, D. Liu, J. A. Lochala, C. S. Anderson, X. Cao, M. E. Gross, W. Xu, J.-G. Zhang, M. S. Whittingham and J. Xiao, *Nat. Energy*, 2021, **6**, 723–732.
215 D. Li, C. Shen, Y. Zheng and J. Xu, *Small*, 2025, **21**, 2407740.
216 A. Chandra, *Compos. Commun.*, 2017, **4**, 33–36.
217 T. Wang, M. Zhang, K. Zhou, H. Wang, A. Shao, L. Hou, Z. Wang, X. Tang, M. Bai and S. Li, *Adv. Funct. Mater.*, 2023, **33**, 2215117.
218 Z. Ge, J. Li and J. Liu, *ChemistrySelect*, 2022, **7**, e202200620.
219 B. Wen, Z. Deng, P.-C. Tsai, Z. W. Lebens-Higgins, L. F. J. Piper, S. P. Ong and Y.-M. Chiang, *Nat. Energy*, 2020, **5**, 578–586.
220 M. Kannadasan, K. Sathiasivan, M. Balakrishnan, B. Subramanian and E. G. Varuvel, *Energy Storage*, 2024, **6**, e636.
221 A. Gayathri, S. Kiruthika, V. Selvarani, M. S. AlSalhi, S. Devanesan, W. Kim and B. Muthukumaran, *Fuel*, 2022, **321**, 124059.
222 S. Yu, Q. Xu, X. Lu, Z. Liu, A. Windmüller, C.-L. Tsai, A. Buchheit, H. Tempel, H. Kungl and H.-D. Wiemhofer, *ACS Appl. Mater. Interfaces*, 2021, **13**, 61067–61077.

223 J.-F. Wu, Q. Wang and X. Guo, *J. Power Sources*, 2018, **402**, 513–518.
224 Z. Zhang, Q. Zhang, J. Shi, Y. S. Chu, X. Yu, K. Xu, M. Ge, H. Yan, W. Li and L. Gu, *Adv. Energy Mater.*, 2017, **7**, 1601196.
225 D. K. Maurya, R. Dhanusuraman, J. Z. Guo and S. Angaiah, *Adv. Compos. Hybrid Mater.*, 2023, **6**, 27.
226 M. D. Singh and A. Dalvi, *Appl. Surf. Sci.*, 2021, **536**, 147792.
227 M. Li, C. Wang, Z. Chen, K. Xu and J. Lu, *Chem. Rev.*, 2020, **120**, 6783.
228 X. Shen, Z. Li, N. Deng, J. Fan, L. Wang, Z. Xia, W. Kang and Y. Liu, *Chem. Eng. J.*, 2020, **387**, 124058.
229 S. A. Hashmi, M. Y. Bhat, M. K. Singh, N. T. K. Sundaram, B. P. C. Raghupathy and H. Tanaka, *J. Solid State Electrochem.*, 2016, **20**, 2817–2826.
230 A. K. Chauhan, D. Kumar, K. Mishra and A. Singh, *Mater. Today Commun.*, 2021, **26**, 101713.
231 A. K. Chauhan, K. Mishra, D. Kumar and A. Singh, *J. Electron. Mater.*, 2021, **50**, 5122–5133.
232 M. P. Fertig, K. Skadell, M. Schulz, C. Dirksen, P. Adelhelm and M. Stelter, *Batteries Supercaps*, 2022, **5**, e202100131.
233 F. G. Will, *J. Electrochem. Soc.*, 1976, **123**, 834.
234 Y. Dong, P. Wen, H. Shi, Y. Yu and Z. Wu, *Adv. Funct. Mater.*, 2024, **34**, 2213584.
235 R. Fang, Y. Li, N. Wu, B. Xu, Y. Liu, A. Manthiram and J. B. Goodenough, *Adv. Funct. Mater.*, 2023, **33**, 2211229.
236 A. J. Bard, L. R. Faulkner and H. S. White, *Electrochemical methods: fundamentals and applications*, John Wiley & Sons, 2022.
237 C. R. Birkl, M. R. Roberts, E. McTurk, P. G. Bruce and D. A. Howey, *J. Power Sources*, 2017, **341**, 373–386.
238 S. J. An, J. Li, C. Daniel, D. Mohanty, S. Nagpure and D. L. Wood, *Carbon*, 2016, **105**, 52–76.
239 K. Guo, R. Kumar, X. Xiao, B. W. Sheldon and H. Gao, *Nano Energy*, 2020, **68**, 104257.
240 J. Kim, O. B. Chae and B. L. Lucht, *J. Electrochem. Soc.*, 2021, **168**, 030521.
241 E. Peled, *J. Electrochem. Soc.*, 1979, **126**, 2047.
242 E. Peled, D. Golodnitsky and G. Ardel, *J. Electrochem. Soc.*, 1997, **144**, L208.
243 S. Xu, Y. Wang, L. Ben, Y. Lyu, N. Song, Z. Yang, Y. Li, L. Mu, H. Yang and L. Gu, *Adv. Energy Mater.*, 2015, **5**, 1501156.
244 E. Talaie, V. Duffort, H. L. Smith, B. Fultz and L. F. Nazar, *Energy Environ. Sci.*, 2015, **8**, 2512–2523.
245 J. Alvarado, C. Ma, S. Wang, K. Nguyen, M. Kodur and Y. S. Meng, *ACS Appl. Mater. Interfaces*, 2017, **9**, 26518–26530.
246 X. Han, Z. Liu, X. Hu, Q. Huang, D. Zhang, H. Guo and Q. Yi, *Adv. Energy Sustainability Res.*, 2024, **5**, 2300166.
247 S. K. Heiskanen, J. Kim and B. L. Lucht, *Joule*, 2019, **3**, 2322–2333.
248 B. Lee, E. Paek, D. Mitlin and S. W. Lee, *Chem. Rev.*, 2019, **119**, 5416–5460.
249 L. Zhu, B. Zhu, J. Luo and B. Liu, *ACS Mater. Lett.*, 2020, **3**, 77–89.
250 H. Che, S. Chen, Y. Xie, H. Wang, K. Amine, X.-Z. Liao and Z.-F. Ma, *Energy Environ. Sci.*, 2017, **10**, 1075–1101.
251 Y. Huang, L. Zhao, L. Li, M. Xie, F. Wu and R. Chen, *Adv. Mater.*, 2019, **31**, 1808393.
252 J. Zhang, J. Gai, K. Song and W. Chen, *Cell Rep. Phys. Sci.*, 2025, **6**, 102456.
253 J. B. Goodenough and Y. Kim, *Chem. Mater.*, 2010, **22**, 587–603.
254 X. Chen, W. He, L.-X. Ding, S. Wang and H. Wang, *Energy Environ. Sci.*, 2019, **12**, 938–944.
255 D. Hlushkou, A. E. Reising, N. Kaiser, S. Spannenberger, S. Schlabach, Y. Kato, B. Roling and U. Tallarek, *J. Power Sources*, 2018, **396**, 363–370.
256 Y. Kato, S. Shiotani, K. Morita, K. Suzuki, M. Hirayama and R. Kanno, *J. Phys. Chem. Lett.*, 2018, **9**, 607–613.
257 Z. Yu, X. Zhang, C. Fu, H. Wang, M. Chen, G. Yin, H. Huo and J. Wang, *Adv. Energy Mater.*, 2021, **11**, 2003250.
258 A. Banerjee, X. Wang, C. Fang, E. A. Wu and Y. S. Meng, *Chem. Rev.*, 2020, **120**, 6878–6933.
259 Y. Tian, T. Shi, W. Richards, J. (JC) Li, J. C. Kim, S. Bo and G. Ceder, *Energy Environ. Sci.*, 2017, **10**, 1150–1166.
260 N. Yazie, D. Worku, N. Gabbiye, A. Alemayehu, Z. Getahun and M. Dagnew, *Mater. Renewable Sustainable Energy*, 2023, **12**, 73–94.
261 G. Lu, G. Meng, Q. Liu, L. Feng, J. Luo, X. Liu, Y. Luo and P. K. Chu, *Adv. Powder Mater.*, 2024, **3**, 100154.
262 W. Tang, R. Qi, J. Wu, Y. Zuo, Y. Shi, R. Liu, W. Yan and J. Zhang, *Electrochem. Energy Rev.*, 2024, **7**, 23.
263 E. Wang, Y. Niu, Y.-X. Yin and Y.-G. Guo, *ACS Mater. Lett.*, 2020, **3**, 18–41.
264 X. Liu, J. Zhao, H. Dong, L. Zhang, H. Zhang, Y. Gao, X. Zhou, L. Zhang, L. Li and Y. Liu, *Adv. Funct. Mater.*, 2024, **34**, 2402310.
265 S. Chen, H. Che, F. Feng, J. Liao, H. Wang, Y. Yin and Z. F. Ma, *ACS Appl. Mater. Interfaces*, 2019, **11**, 43056–43065.
266 L. Ran, S. Tao, I. Gentle, B. Luo, M. Li, M. Rana, L. Wang and R. Knibbe, *ACS Appl. Mater. Interfaces*, 2021, **13**, 39355–39362.
267 Y. Wang, Z. Wang, X. Xu, S. J. A. Oh, J. Sun, F. Zheng, X. Lu, C. Xu, B. Yan and G. Huang, *Nanomicro Lett.*, 2024, **16**, 1–14.
268 L. S. Plashnitsa, E. Kobayashi, Y. Noguchi, S. Okada and J. Yamaki, *J. Electrochem. Soc.*, 2010, **157**, A536.
269 Y. Zhou, X. Shao, K. Lam, Y. Zheng, L. Zhao, K. Wang, J. Zhao, F. Chen and X. Hou, *ACS Appl. Mater. Interfaces*, 2020, **12**, 30328–30335.
270 Z. Cheng, M. Liu, S. Ganapathy, C. Li, Z. Li, X. Zhang, P. He, H. Zhou and M. Wagemaker, *Joule*, 2020, **4**, 1311–1323.
271 M. Kannadasan, K. Sathiasivan, I. Pandurangan and M. Balakrishnan, *Int. J. Hydrogen Energy*, 2024, **78**, 634–641.
272 M. Cheng, T. Qu, J. Zi, Y. Yao, F. Liang, W. Ma, B. Yang, Y. Dai and Y. Lei, *Nanotechnology*, 2020, **31**, 425401.
273 L. Azhari, S. Bong, X. Ma and Y. Wang, *Matter*, 2020, **3**, 1845–1861.
274 A. Machín, M. C. Cotto, F. Díaz, J. Duconge, C. Morant and F. Márquez, *Batteries*, 2024, **10**, 255.